

3-22-2019

High Fidelity Satellite Navigation Receiver Front-End for Advanced Signal Quality Monitoring and Authentication

Andrew D. Braun

Follow this and additional works at: <https://scholar.afit.edu/etd>



Part of the [Navigation, Guidance, Control and Dynamics Commons](#), and the [Signal Processing Commons](#)

Recommended Citation

Braun, Andrew D., "High Fidelity Satellite Navigation Receiver Front-End for Advanced Signal Quality Monitoring and Authentication" (2019). *Theses and Dissertations*. 2248.
<https://scholar.afit.edu/etd/2248>

This Thesis is brought to you for free and open access by the Student Graduate Works at AFIT Scholar. It has been accepted for inclusion in Theses and Dissertations by an authorized administrator of AFIT Scholar. For more information, please contact richard.mansfield@afit.edu.



**HIGH FIDELITY SATELLITE NAVIGATION RECEIVER FRONT-END FOR
ADVANCED SIGNAL QUALITY MONITORING AND AUTHENTICATION**

THESIS

Andrew D. Braun, USAF

AFIT-ENG-MS-19-M-013

**DEPARTMENT OF THE AIR FORCE
AIR UNIVERSITY**

AIR FORCE INSTITUTE OF TECHNOLOGY

Wright-Patterson Air Force Base, Ohio

**DISTRIBUTION STATEMENT A.
APPROVED FOR PUBLIC RELEASE; DISTRIBUTION UNLIMITED.**

The views expressed in this thesis are those of the author and do not reflect the official policy or position of the United States Air Force, Department of Defense, or the United States Government. This material is declared a work of the U.S. Government and is not subject to copyright protection in the United States.

AFIT-ENG-MS-19-M-013

HIGH FIDELITY SATELLITE NAVIGATION RECEIVER FRONT-END FOR
ADVANCED SIGNAL QUALITY MONITORING AND AUTHENTICATION

THESIS

Presented to the Faculty

Department of Electrical and Computer Engineering

Graduate School of Engineering and Management

Air Force Institute of Technology

Air University

Air Education and Training Command

In Partial Fulfillment of the Requirements for the

Degree of Master of Electrical Engineering

Andrew D. Braun, BS

USAF

March 2019

DISTRIBUTION STATEMENT A.
APPROVED FOR PUBLIC RELEASE; DISTRIBUTION UNLIMITED.

AFIT-ENG-MS-19-M-013

**HIGH FIDELITY SATELLITE NAVIGATION RECEIVER FRONT-END FOR
ADVANCED SIGNAL QUALITY MONITORING AND AUTHENTICATION**

Andrew D. Braun, BS

USAF

Committee Membership:

Dr. Sanjeev Gunawardena
Chair

Dr. Richard Martin
Member

Dr. Jeff Hebert
Member

Abstract

Over the past several years, interest in utilizing foreign satellite timing and navigation (satnav) signals to augment GPS has grown. Doing so is not without risks; foreign satnav signals must be vetted and determined to be trustworthy before use in military applications. Advanced signal quality monitoring methods can help to ensure that only authentic and reliable satnav signals are utilized. To effectively monitor and authenticate signals, the receiver's front-end must impress as little distortions upon the signal as possible. The purpose of this study is to design, fabricate, and test the performance of a high-fidelity satnav receiver front-end for advanced monitoring of foreign and domestic space vehicle (SV) signals.

Advanced satnav integrity checking and authentication extends beyond range measurement based techniques such as receiver autonomous integrity monitoring (RAIM) and fault detection and exclusion (FDE). Monitoring signal deformations and spreading code chip asymmetries that are characteristic to specific space vehicles can significantly extend satnav signal quality monitoring and authentication capabilities [1]. In order to procure high fidelity nominal satnav signal deformations that may serve as a reference, the front-end of the receiver must not impress any deformations of its own. A database of nominal signal features can then be used to ascertain what is authentic versus inauthentic operation.

Current commercial receiver technology does not perform high fidelity correlation monitoring or distinguish spreading code chip asymmetries between different

SVs. These techniques benefit from a high fidelity front-end that cannot be purchased off the shelf. Chip-shape out of the satnav signal processing requires extended coherent integration times and narrow tracking loop bandwidths [1]. The stability of the reference oscillator and phase noise contributed by the frequency synthesizer limits the effectiveness of long coherent integration [2]. Thus, a highly stable reference oscillator and low phase noise frequency synthesizer are used in this front-end. Group delay variations of filters in a receiver front-end adds distortions to the satnav signals and can create pseudorange biases [3],[4]. To preserve the received signal's nominal signal characteristics, group delay variations of filters are minimized over the front-end's passband.

The front-end utilizes a superheterodyne architecture to convert satnav signals down to an intermediate frequency, in which it is bandpass sampled by a high bandwidth, high dynamic range analog-to-digital converter (ADC). Unlike the commonly used direct downconversion receiver that is plagued by inphase/quadrature (I/Q) gain and phase imbalances that can significantly impact received signal observables, this architecture produces a real stream of digitized samples that guarantees zero I/Q imbalance since quadrature downconversion is performed digitally. The front-end is designed to the OpenVPX 3U card form factor and consumes less than 3.5 Watts of power. Digital attenuators and root-mean-squared (RMS) power detectors are utilized to enable software-defined smart gain control to preserve linearity, maintain a low noise figure, and rapidly respond to interference. The front-end developed in this thesis is uniquely suited for use in high fidelity all-domain satnav signal monitoring. These domains include time domain, frequency domain, correlation domain (i.e. chip shape), spatial domain (using

multi-element controlled reception pattern antennas (CRPAs)), and polarization domain (using dual-polarized antenna elements in a CRPA). The results presented offer significant advancements towards high-fidelity satnav constellation monitoring and characterization, and next-generation navigation warfare (NAVWAR) applications.

Acknowledgments

I would like to give thanks to God for the opportunities to struggle and grow in perseverance.

A big thank you to my parents. Being electrical engineers themselves, they have always fortified education and scientific exploration. The success of this thesis would not have been possible if not for their endless support and encouragement throughout my academic career. Thank you to my siblings who have always been a source of encouragement and inspiration.

I would like to offer my sincere gratitude and appreciation to my advisor Dr. Sanjeev Gunawardena. Having started the thesis with virtually no electronics or RF experience, under his guidance I was able to achieve something I did not think I could accomplish. He has been a great source of motivation and inspiration through the duration of the thesis. By his own example and patience, he has helped instill a desire to work hard and persevere.

I would like to thank my committee members, Dr. Martin and Dr. Hebert for their valuable time and technical input toward this thesis.

None of this work would have been possible if not for the sponsorship of AFRL/RYWN; for that I am sincerely grateful. To have the opportunity to design, build, and test state-of-art technology with world class instruments and tools has been an extremely rewarding experience.

Thank you to Pranav and Jorge for assisting me in operating the RF instrumentation and PCB assembly equipment. They have never hesitated to lend a hand.

A special thank you to my colleagues from LCMC. They had involved and tutored me in several high impact projects as an inexperienced engineer. By doing so, they had inspired me to pursue GPS related topics at AFIT.

Andrew D. Braun

Table of Contents

	Page
Abstract	iv
Acknowledgments.....	vii
List of Figures	xi
List of Tables	xvi
List of Acronyms	xvii
I. Introduction	1
1.1 General Issue/Motivation	1
1.2 Problem Statement	2
II. Background/Literature Review	4
2.1 Chapter Overview	4
2.2 Satnav Signal Overview	4
2.3 Gain, Noise Figure and Sensitivity	6
2.4 Linearity	7
2.5 Dynamic Range	9
2.6 Mixer	10
2.7 Image Rejection.....	11
2.8 Selectivity.....	12
2.9 Receiver Architectures	12
2.10 Reference Oscillator.....	18
2.11 Frequency Synthesizer Phase Locked Loop	23
2.12 Group Delay Variations	28
2.13 RF Filters for Satnav Instrumentation.....	29
2.14 IF / Antialiasing Filters	30

2.15	Receiver Carrier Tracking Loops and Errors	31
III.	Methodology	35
3.1	Chapter Overview	35
3.2	Receiver Architectures	36
3.3	Analog to Digital Converter	36
3.4	Bandpass Antialiasing Filter	40
3.5	RF Image Rejection Filter	44
3.6	Reference Oscillator	51
3.7	Frequency Synthesizer Phase Locked Loop.....	52
3.8	Gain Control and Linearity for the ADC	56
3.9	RMS Power Detector	60
3.10	Gain Control, Noise Figure and Linearity RF Calculator.....	61
3.11	Nonlinear Simulation of Front-End	68
IV.	Analysis and Results	71
4.1	Introduction	71
4.2	Waveguide Evaluation	72
4.3	Front-End Low Noise Amplifier Evaluation.....	74
4.4	Frequency Synthesizer Evaluation	76
4.5	Frequency Synthesizer Design	89
4.6	Power Supply Design	92
4.7	IF Filter Design	94
4.8	RF Portion of RF Front-End Design	96
4.9	IF Portion of RF Front-End Design.....	101

4.10	Analog to Digital Converter Evaluation Results	104
4.11	Software Defined Satnav Signal Tracking & Front-End Results	107
V.	Conclusions and Recommendations.....	122
5.1	Conclusions of Research	122
5.2	Significance of Research.....	123
5.3	Recommendations for Future Research	124
5.4	Summary	125
	Appendix A: PCB Stack Up	126
	Appendix B: 3D Render.....	127
	Bibliography	128

List of Figures

	Page
Figure 2.4.1: 3 rd Order Intermodulation Products.....	8
Figure 2.6.1: Mixer Signal Translation.....	10
Figure 2.7.1: Image Frequency with Respect to LO.....	11
Figure 2.9.1: Direct Conversion Receiver Architecture	13
Figure 2.9.2: LO to RF Isolation at the Mixer	14
Figure 2.9.3: Direct RF Sampling Receiver Architecture.....	16
Figure 2.9.4: Superheterodyne Receiver Architecture.....	17
Figure 2.10.1: Two State Clock Process Noise Model [8]	19
Figure 2.10.2: SSB Calculated Phase Noise of OCXO ¹	21
Figure 2.10.3: Allan Variance Calculation	22
Figure 2.10.4: Simulated vs. Calculated Allan Variance	23
Figure 2.11.1: Integer-N PLL with 2 nd -Order Loop Filter.....	24
Figure 2.11.2: LTI Phase Domain Model with Additive Noise Sources	25
Figure 2.11.3: FSPLL Simulated Phase Noise and Measured Phase Noise from LMX 2582 In its 1 st Configuration	27
Figure 2.15.1: Receiver Carrier Tracking Loop.....	31
Figure 3.3.1: Nyquist Zones of the Analog Devices AD 9681 ADC	37
Figure 3.3.2: 1 st Nyquist Zone Frequency Overlap.....	38
Figure 3.3.3: 3 rd Nyquist Zone Frequency Response.....	39
Figure 3.3.4: Frequency Plan of the Receiver Front-End	39
Figure 3.4.1: Genesys IF Filter Using Theoretical Components	42

Figure 3.4.2: Frequency Response of Vendor Part Synthesis and Theoretical of IF Filter	43
Figure 3.4.3: Group Delay Response of Vendor Part Synthesis and Theoretical Design of IF Filter.....	44
Figure 3.5.1: Group Delay, Image Rejection, and Frequency Response of RF Filter Configurations.....	46
Figure 3.5.2: Five Resonator Ceramic RF Filter Image Rejection	47
Figure 3.5.3: Four Resonator Ceramic RF Filter Image Rejection.....	48
Figure 3.5.4: Four Resonator Ceramic RF Filter Image Rejection.....	49
Figure 3.5.5: Group Delay of RF Bandpass Filters	50
Figure 3.6.1: 10 MHz OCXO Reference Oscillator SSB Phase Noise.....	52
Figure 3.8.1: ADC Operation at -97 dBm Input Power	57
Figure 3.8.2: ADC Operation at -43 dBm Input Power	58
Figure 3.8.3: ADC Operation at Full Scale Input Power (-27 dBm)	59
Figure 3.9.1: RMS Power Detector Signal Path	60
Figure 3.11.1: Genesys Nonlinear Signal Path Simulation	68
Figure 3.11.2: Gain and Linearity at -97 dBm Operation.....	69
Figure 3.11.3: Gain and Linearity at -26 dBm Operation.....	70
Figure 4.2.1: CPWG Evaluation Board	72
Figure 4.2.2: CPWG S11 for Different Dimensions	73
Figure 4.2.3: CPWG Isolation	73
Figure 4.3.1: Left: MACOM Evaluation Board, Right: Constructed Evaluation Board ..	74
Figure 4.3.2: MAL-010704 LNA Gain and Linearity vs. Bias.....	75
Figure 4.3.3: S11 of MAL-010704 LNA	76

Figure 4.4.1: Charge Pump, Loop Filter components and VCO Circuit	77
Figure 4.4.2: LMX 2582 Evaluation Board from Texas Instruments	78
Figure 4.4.3: ADF 4355-2 Evaluation Board from Analog Devices	79
Figure 4.4.4: MAX 2871 Evaluation Board from Maxim Integrated	80
Figure 4.4.5: HMC 830 Evaluation Board from Hittite (Analog Devices)	81
Figure 4.4.6: LMX 2582 Spurs in Configuration # 1	83
Figure 4.4.7: HMC 830 Spurs in Configuration # 1	84
Figure 4.4.8: Phase Noise Collection with the Keysight PXA 9030B Spectrum Analyzer [39]	86
Figure 4.4.9: Phase Noise Measurements Taken from the Best Performing Configurations on Each Device	88
Figure 4.5.1: Constructed LMX 2582 Circuit	90
Figure 4.5.2: LMX 2582 Phase Noise at L1, L2, L5 LO	91
Figure 4.6.1: Front-End Power Supply Linear Voltage Regulators	92
Figure 4.6.2: 5.0 V Linear Regulator Power from ADP3339 [40]	93
Figure 4.6.3: 3.3 V Linear Power Regulator from ADM7150 [41]	93
Figure 4.6.4: 6.0 V Power Supplied Through BK Precision [35]	94
Figure 4.7.1: IF Filter Assembled on a Surface Mount PCB	94
Figure 4.7.2: IF Filter Response and Repeatability	95
Figure 4.7.3: IF Filter Group Delay and Repeatability	96
Figure 4.8.1: RF Portion and Layout of the Front-End	97
Figure 4.8.2: First RF Room Gain and Linearity	98
Figure 4.8.3: RF Gain and Linearity of RF Signal-Path	99

Figure 4.8.4: Group Delay of RF Signal Path.....	100
Figure 4.8.5: RF Filter Response of Signal Path	101
Figure 4.9.1: IF Portion of the Front-End.....	102
Figure 4.9.2: IF Portion Gain and Linearity of the Front-End.....	103
Figure 4.9.3: IF Portion Response and Group Delay of the Front-End	104
Figure 4.10.1: AD 9681 Evaluation Board	105
Figure 4.10.2: ADC PSD from Live-sky Antenna.....	106
Figure 4.11.1: RF Front-End Under Test.....	107
Figure 4.11.2: RF Front-End Under Test with Arduino and ADC	108
Figure 4.11.3: Simulated Satnav Signal Testbed with LMX 2582 LO.....	109
Figure 4.11.4: PSD and Time-Domain Sample Snapshot of R&S Simulated Satnav Data	110
Figure 4.11.5: Measured CNR When Using the LMX 2582 as the LO.....	111
Figure 4.11.6: Carrier Filter Tracking States LMX 2582 PLL LO.....	112
Figure 4.11.7: Simulated Satnav Signal Testbed with Synergy Microwave LO	113
Figure 4.11.8: CNR Measurements Using the LMX 2582 LO and the Synergy Microwave LO	113
Figure 4.11.9: Carrier Filter Tracking States Using the Synergy Microwave FSPLL as LO Plotted Overtop the TI LMX 2582.....	115
Figure 4.11.10: CNR Measured from Septentrio PolaRx5 Receiver.....	116
Figure 4.11.11: Carrier Phase Measurement Residues with Septentrio PolaRx5.....	117
Figure 4.11.12: Live-sky Satnav Signal with LMX 2582 LO	118
Figure 4.11.13: L1-Band Live-sky Capture 62.5 MHz of Bandwidth PSD	118

Figure 4.11.14: PRN 08 C/A Acquisition of Live-sky Signals.....	119
Figure 4.11.15: Live-Sky PRN 08 C/A Carrier Tracking Loop Output	120
Figure 4.11.16: Live-Sky CNR of Tracked PRN 08.....	120
Figure 4.11.17: Live-Sky Carrier Tracking Lock Indicator for PRN 08	121

List of Tables

	Page
Table 2.10.1: Allan Variance Power Coefficients for Typical Oscillators	21
Table 2.15.1: Typical Loop Filter Values	33
Table 3.10.1: Gain, Linearity and Noise Figure of Front-End with Passive Antenna - 97dBm	62
Table 3.10.2: Gain, Linearity and Noise Figure of Front-End -46 dBm Input	65
Table 3.10.3: Linearity, Gain and Noise Figure of Front-End at Full Scale -26dBm	67
Table 4.3.1: MAL-010704 LNA Current Consumption	76
Table 4.4.1: LMX 2582 Configurations	78
Table 4.4.2: ADF 4355-2 Configurations	79
Table 4.4.3: MAX 2871 Configurations	80
Table 4.4.4: HMC 830 Configurations	81
Table 4.4.5: LMX 2582 Spur Powers (dBc)	82
Table 4.4.6: ADF 4355-2 Spur Powers (dBc)	83
Table 4.4.7: MAX 2871 Spur Powers (dBc)	84
Table 4.4.8: HMC 830 Spur Powers (dBc)	84
Table 4.4.9: LMX 2582 Integrated Phase Noise RMS Error	86
Table 4.4.10: ADF 4355-2 Integrated Phase Noise RMS Error	87
Table 4.4.11: MAX 2871 Integrated Phase Noise RMS Error	87
Table 4.4.12: HMC 830 Integrated Phase Noise RMS Error	87
Table 4.5.1: Frequency Synthesizer Performance vs Reference Oscillator	91

List of Acronyms

ADC	Analog to Digital Converter
AGC	Automatic Gain Control
BPF	Bandpass Filter
BPSK	Binary Phase Shift Keying
CDMA	Code Division Multiple Access
CNR	Carrier to Noise Ratio
CPWG	Coplanar Waveguide
DC	Direct Current
ENOB	Effective Number of Bits
EMI	Electromagnetic Interference
FDMA	Frequency Division Multiple Access
FSPLL	Frequency Synthesizer Phase Locked Loop
FFM	Flicker Frequency Modulation
GPS	Global Positioning System
GLONASS	Globalnaya Navigazionnaya Sputnikovaya Sistema
IEEE	Institute of Electronics and Electrical Engineers
IF	Intermediate Frequency
IQ	In-phase and Quadrature Phase
IRNSS	Indian Regional Navigation Satellite System
LPF	Low Pass Filter
LNA	Low Noise Amplifier
LO	Local Oscillator

MMIC	Monolithic Microwave Integrated Circuit
OCXO	Oven Controlled Crystal Oscillator
OIP3	Output 3 rd Order Intercept Point
OIP1	Output 1dB Saturation Point
OPSAT	Output Saturation Point
PCB	Printed Circuit Board
PFD	Phase Frequency Detector
PLL	Phase Locked Loop
PNT	Position Navigation and Timing
PRN	Pseudorandom Number
PSD	Power Spectral Density
RF	Radio Frequency
RMS	Root Mean Square
RWFM	Random Walk Frequency Modulation
RO	Reference Oscillator
QZSS	Quasi-Zenith Satellite System
SDR	Software Defined Radio
SNR	Signal to Noise Ratio
SRF	Self Resonate Frequency
SV	Space Vehicle
TCXO	Temperature Compensated Crystal Oscillator
VCO	Voltage Controlled Oscillator
VNA	Vector Network Analyzer

WFM	White Frequency Modulation
WSS	Wide Sense Stationary
XO	Crystal Oscillator

HIGH FIDELITY SATELLITE NAVIGATION FRONT-END FOR SIGNAL QUALITY MONITORING AND ADVANCED AUTHENTICATION

I. Introduction

1.1 General Issue/Motivation

For military and civilian applications, having reliable and trustworthy satnav signals is of paramount importance. Many civilian applications depend on the integrity of satnav signals; a few major applications include precision aircraft landing and approach, finance and banking transactions, cargo shipping lanes, power grid synchronization, cellular networks, autonomous navigation, railway operations, survey, and precision agriculture. As the dependence upon satnav signals grow, so do the implications of signal disruptions. Interference can quickly overcome receivers, denying position-navigation-timing (PNT) capability. Software defined radios (SDRs) can pose a new threat in the hands of a nefarious actor. The implications of a receiver computing a false PNT solution can be seriously detrimental in many applications.

Advanced signal and spectrum monitoring and using foreign satnav signals can mitigate the threats posed toward military and civilian receivers. The monitoring equipment can provide civilian and military receivers with situational awareness preventing false and inaccurate PNT solutions.

High fidelity satnav signal monitoring entails providing nominal measurements of the deformations impressed upon the signal by the satellites themselves. These natural signal deformations are caused by the filter responses, amplifiers, and frequency synthesizer in the satellite. These deformations result in a unique "chip shape" in the

broadcast pseudo-random number (PRN) codes. Some of these deformations are distinct to specific satellites [1]. By measuring the nominal signal characteristics of the satnav signals, receivers can begin to distinguish authentic satnav signals from those that may be transmitted by bad actors.

High fidelity monitoring in spectrally diverse locations where strong interference may be present is an important capability to have. The advanced monitoring receiver would be able to detect and quantize interference with enough dynamic range to perform later analysis on it.

Unique design challenges arise in engineering a high-fidelity satnav signal monitor. Traditional commercial-off-the-shelf (COTS) satnav receivers are inadequate. Users have little to no control of the correlators and tracking loops within the receiver due to proprietary architectures. Users have no access to the digital samples, and the RF front-end lacks in performance. The RF front-end of the receiver is perhaps the most important component for high fidelity satnav monitoring. The purpose of this thesis is that very topic. In order to preserve the natural signal deformations characteristic of specific satellites, the front-end must impress as little deformations as possible on the received signals. This entails careful selection and design of the filters, reference oscillator (RO), frequency synthesizer, amplifiers, and sample rate.

1.2 Problem Statement

The purpose of this study is to design, fabricate, and test the performance of high-fidelity satnav receiver RF front-ends that are capable of instrumentation-grade signal analysis. An instrumentation-grade satnav front-end provides the analog-to-digital-

converter (ADC) with minimum distortions and noise not already present on the signal. Measurements computed with known satnav algorithms can then be used as a baseline against other receivers [1]. The frequency synthesizer phase-locked loop (FSPLL), group delay of filters, and linearity of the front-end are the major research thrusts in this study.

II. Background/Literature Review

2.1 Chapter Overview

This chapter discusses the basics of satnav signals, receiver front-ends and signal tracking. An overview of the satnav signal structure is provided for multiple constellations. Receiver operating characteristics are discussed including signal-to-noise ratio (SNR), carrier-to-noise ratio (CNR), gain, noise figure, linearity, group delay, frequency plan, reference oscillator and frequency synthesizers. Detrimental effects to the receiver's signal tracking ability are also described.

2.2 Satnav Signal Overview

The satnav signals of interest for this study reside in the Institute of Electrical and Electronic Engineers (IEEE) L-Band spanning from 1-2 GHz [5]. The L-Band is a very spectrally dense and highly sought-after portion of the electromagnetic spectrum due to its desirable atmospheric propagation properties. In particular for space-to-ground and ground-to-space communications and navigation.

The Global Positioning System (GPS) is a USAF owned and operated satnav system and consists of a satellite constellation in medium earth orbit (MEO). Other countries and alliances have procured their own satellite navigation constellations. Japan and India operate regional satnav capabilities QZSS and NAVIC respectively. The European Space Agency (ESA) has fielded Galileo. The Russian Federation has fielded GLONASS. The People's Republic of China has fielded BeiDou.

Satnav signals are broadcasted on several frequencies in the L-Band. The GPS Link-1 (L1) band is centered at 1575.42 MHz and is the major focus of this study. Satnav signals are also broadcast on L2 (1227.60 MHz) and L5 (1176.45 MHz) for GPS and several other constellations. GPS, BeiDou, (modernized) GLONASS, and Galileo are global systems that have satnav signals on the L1 band.

Besides the legacy GLONASS signals, all satnav signals use code-division-multiple-access (CDMA). Psuedo-random number (PRN) codes that are orthogonal from one another are used to distinguish satellites and offer ranging precision to the receiver. The PRN codes are phase modulated along with data containing orbital parameters (known as ephemeris), timing, and satellite health information.

2.2.1 SNR and CNR

SNR is a dimensionless measurement and usually expressed in terms of dB as:

$$SNR (dB) = 10 \log_{10} \frac{Signal Power (W)}{Noise Power (W)} = Signal (dBW) - Noise (dBW). \quad (1)$$

All front-end components contribute to the noise figure, starting with the thermal noise of the antenna. Thermal noise is modeled as a stationary white random process, with a variance of σ_{n0}^2 . The thermal noise power for a given temperature and bandwidth is given as:

$$n_0(t) \sim N(0, \sigma_{n_0}^2), \quad (2)$$

$$\sigma_{n_0}^2 = k_B T_0 B_{fe}, \quad (3)$$

where k_B is Boltzmann's constant $1.38E-23$ Joules / Kelvin, T_0 is the effective noise temperature in Kelvin, and B_{fe} is the bandwidth of the receiver's front-end. For a receiver at room temperature, $T_0 = 290K$, and $B_{fe} = 50MHz$; the thermal noise power is -127 dBW. The thermal noise within a 1 Hz bandwidth is -204 dBW/Hz. For an isotropic antenna, the minimum received signal power for the L1 C/A signal is -159 dBW, and -157 dBW for the new L1C signal. Thus the SNR for the L1 C/A signal is -159 dBW $- (-127$ dBW) = -32 dB. The received satnav signal is -32 dB below the thermal noise power for a 50 MHz bandwidth front-end. Equivalently, the thermal noise power is 1585 times stronger than the received satnav signal. Carrier-to-Noise-Density Ratio (CNR) is bandwidth agnostic because it considers the noise in a 1 Hz bandwidth and is given as:

$$\frac{C}{N_0} = SNR (dB) + 10 \log_{10} B_{fe} = -32 (dB) + 77 (Hz) = 45 (dB - Hz). \quad (4)$$

2.3 Gain, Noise Figure and Sensitivity

The noise factor of a system is the amount of SNR degradation that a signal experiences as it passes through the system. Noise factor expressed in dB is referred to as noise figure.

A receiver front-end is a cascade of many analog RF components, the antenna, filter, amplifier, transmission line, and mixers. All of which contribute a gain or loss, and a noise factor (NF). The noise factor and gain for a series of components in a signal path can be calculated using Friis Formula [5]:

$$F = F_1 + \frac{F_2 - 1}{G_1} + \frac{F_3 - 1}{G_1 G_2} + \frac{F_4 - 1}{G_1 G_2 G_3} + \frac{F_n - 1}{G_1 G_2 G_3 \dots G_{n-1}}, \quad (5)$$

$$G = G_1 G_2 G_3 \dots G_n, \quad (6)$$

where G_n are the gains of each device and F_n is the noise factor. It is apparent that the first several components in the signal path are the most significant for setting the noise figure of the front-end. Lossy components such as filters and transmission lines can degrade the noise figure and SNR if the satnav signal has not been adequately amplified. Sensitivity is determined by the noise figure of the receiver. It is the lowest possible received signal power at the antenna that the downstream signal processing can detect [6].

2.4 Linearity

Active devices such as amplifiers and analog-to-digital converters (ADCs) need to operate in their linear region in order to preserve the natural satnav signal characteristics. If an excessive amount of input power is supplied to an active device, it will saturate (experience non-linear behavior) and create harmonics and intermodulation products on the output.

Device manufactures supply operating points for their components to users in the form of datasheets. It is the responsibility of the designer to keep all the devices in the signal path operating in the linear region throughout the expected signal dynamic range. Manufactures typically supply the gain, noise figure, output power 3rd order intercept point, and output power 1 dB saturation point.

The 3rd order intercept point describes the nonlinearity of a system. 3rd order modulation products lie much closer to the input signals and are therefore more likely to

be in-band. This is detrimental to CDMA signals used in satnav. FSPLLs in monolithic multi-radio chips contain lots of spurious content. Intermodulation products between the spurs can degrade the tracking capability of the receiver. Figure 2.4.1 shows the intermodulation products of a nonlinear system.

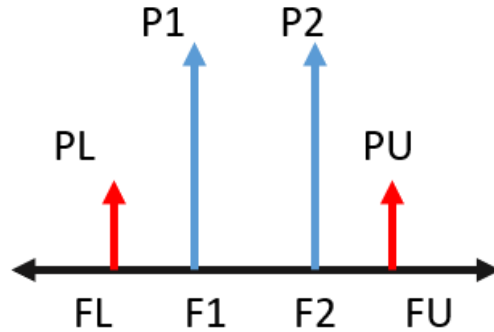


Figure 2.4.1: 3rd Order Intermodulation Products

The tones at frequencies F_L and F_U are the intermodulation products of tones at F_1 and F_2 .

F_L and F_U can be located through:

$$F_L = F_1 \mp 2F_2, \quad (7)$$

$$F_U = 2F_1 \mp F_2. \quad (8)$$

The power of the tones at F_U and F_L can be found by:

$$P_L = P_2 - 2(IP3 - P_1)(dBm), \quad (9)$$

$$P_U = P_1 - 2(IP3 - P_2)(dBm), \quad (10)$$

where P_2 and P_1 are the output powers of the device and $IP3$ is the 3rd order intercept point in dBm.

A receiver front-end is a cascade of many active and passive components. Therefore, it is useful to know cascaded 3rd order intercept point for a receiver. The 3rd order intercept for a cascade of signal components is given as:

$$ip3_c = \frac{1}{\frac{1}{ip3_{N-1} * g_N} + \frac{1}{ip3_N}} (mW). \quad (11)$$

All terms are expressed in mW. g_N is the gain of the Nth device. $ip3_c$ is the 3rd order intercept point up to the Nth device expressed in mW.

2nd order intermodulation products occur at $F1 \pm F2$. This is generally not a significant problem for superheterodyne receivers since the intermodulation products occur out-of-band. However, for direct conversion receivers, the intermodulation products are produced within the passband of the baseband signal and can severely degrade SNR (receiver architectures are covered in Section 2.9).

The 1 dB saturation point is the device's output power that diverges from the linear relationship between input/output power by 1 dB. It is up to the designer to not approach that point to ensure linear operation of the front-end.

2.5 Dynamic Range

Dynamic range is the difference between the smallest detectable signal power and the largest received signal power that the front-end can handle without saturating. A satnav front-end for signal monitoring and instrumentation purposes requires a high dynamic range due to the possibility of a diverse operating environment. Large amounts of interference may be present in the satnav signal band, which has the possibility of saturating the front-end if preventive measures are not taken. Further, for instrumentation

applications, the desire is to receive strong interference with no front-end saturation such that the interference can be carefully analyzed. This is significantly different to other satnav receiver front-ends where the goal is to merely reject the interference as much as possible.

The ADC also plays an important role in the dynamic range. The effective number of bits (ENOB) is the amount of bits that have not been degraded by noise. The input range is usually specified in volts from the manufacture. Each bit of the ADC represents 6 dB of dynamic range. It is the front-end's responsibility to adjust the gain of the input signal to excite the appropriate bits of the ADC. More is discussed in Section 3.8 Gain Control and Linearity for the ADC.

2.6 Mixer

A mixer is an inherently nonlinear device used for frequency translation. Figure 2.6.1 displays a mixer block diagram.

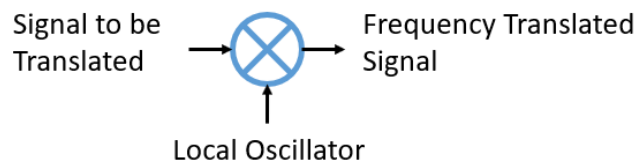


Figure 2.6.1: Mixer Signal Translation

The 2nd order nonlinearity is used to create a sum and difference of the input frequencies through:

$$f_{out} = f_1 \mp f_2. \quad (12)$$

A receiver architecture needs to mix the desired frequency at RF to an intermediate frequency (IF) where it is sampled and quantized by an ADC. A mixer is usually defined by its insertion loss and noise figure. Insertion loss is the amount of degradation to the signal power [6].

2.7 Image Rejection

The RF image rejection filter is responsible for preventing out-of-band signals from mixing into the IF. Image rejection is the receiver's ability to attenuate the image frequency for a given local oscillator (LO) and desired frequency. The image frequency for low-side mixing ($f_{LO} < f_{RF}$) and high-side mixing ($f_{LO} > f_{RF}$) is given by:

$$f_{image} = f_{LO} - f_{IF} = f_{RF} - 2f_{IF}, \quad (13)$$

$$f_{image} = f_{LO} + f_{IF} = f_{RF} + 2f_{IF}. \quad (14)$$

Figure 2.7.1 displays the image frequency location with respect to the f_{LO} [5].

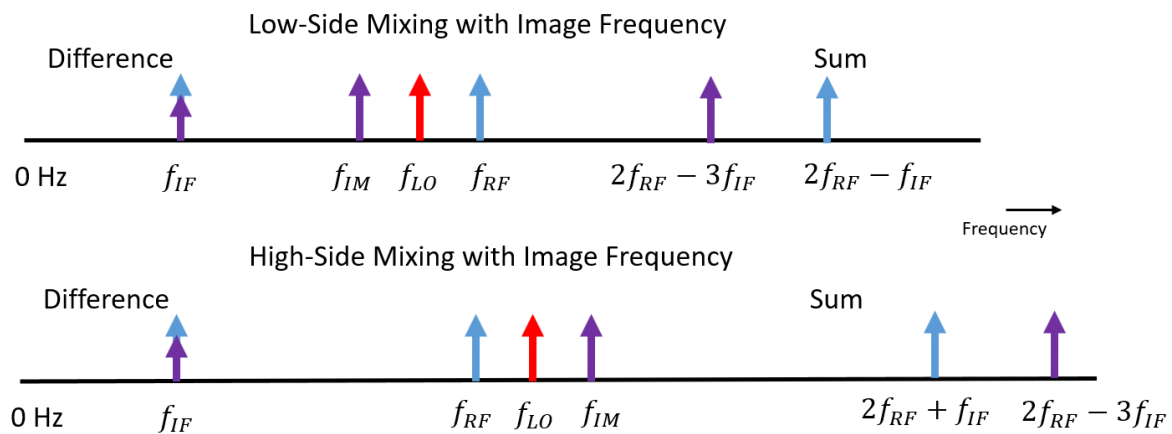


Figure 2.7.1: Image Frequency with Respect to LO

The image rejection filter's purpose is to attenuate the image frequency. This prevents energy from the image frequency from being down converted into the f_{IF} .

An image rejection mixer is a technique that some receivers use to remove the need for an image rejection filter. An image rejection mixer uses $f_{LO} = f_{RF}$.

2.8 Selectivity

Selectivity is the receiver's ability to isolate a desired signal at a given frequency while rejecting out-of-band interference. Spurs generated by the FSPLL can mix-in outside interference into the passband. Phase noise from the FSPLL will transfer onto any interfering signals, degrading SNR. Harmonics generated by the nonlinearities of active components can mix-in unwanted out-of-band interference [6].

2.9 Receiver Architectures

The choice of receiver architecture is dictated by acceptable performance, implementation, complexity, size, weight, power consumption and cost. Performance is the most important deciding factor in the design process of a high-fidelity satnav signal monitoring front-end. Power consumption and size of the front-end is the next most significant concern. The receiver's sensitivity, selectivity, image rejection, frequency planning and generation, dynamic range, and linearity are the major performance parameters that drive the requirements of the front-end.

Frequency planning and generation are dictated by the receiver architecture and performance of RF components that are available to the designer. The designer has to make tradeoffs between performance, size, weight, and cost. The biggest design hurdles

lie in the LO generation for down conversion and sampling. Limiting spurs and phase noise on the LO is fundamental to the performance of the receiver.

2.9.1 Direct Conversion

The desired portion of RF spectrum centered at f_c is down converted directly to direct current (DC) (0 Hz) using an LO frequency equal to f_c . Therefore, the image frequency matches the RF signal. The homodyne receiver does not require an image rejection filter, allowing it to be tunable over a wide range of frequencies. Figure 2.91 displays the block diagram of a homodyne receiver front-end, including an RF selection filter.

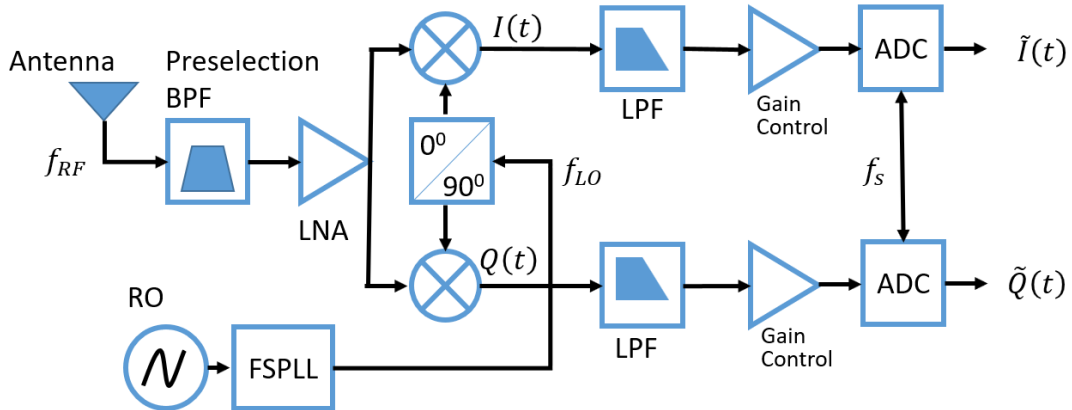


Figure 2.9.1: Direct Conversion Receiver Architecture

$I(t)$ and $Q(t)$ are the in-phase and quadrature-phase components of the signal; they are 90° orthogonal to one another. After the filter IQ become [6]:

$$\tilde{I}(t) = \frac{1}{2}I(t) \cos(\theta(t)) + \frac{1}{2}Q(t) \sin(\theta(t)), \quad (15)$$

$$\tilde{Q}(t) = \frac{1}{2}I(t) \sin(\theta(t)) + \frac{1}{2}Q(t) \cos(\theta(t)). \quad (16)$$

If there is insufficient isolation between the LO and RF signal paths, then the LO may couple onto the RF input and mix with itself creating a large DC signal at baseband. The LO may even leak into the input of the LNA, get amplified, and then mix with itself down to DC. This degradation is particularly present when the LNA, mixer, and FSPLL are integrated onto the same semiconductor substrate because high levels of isolation are challenging to achieve on-chip. This is displayed in Figure 2.9.2.

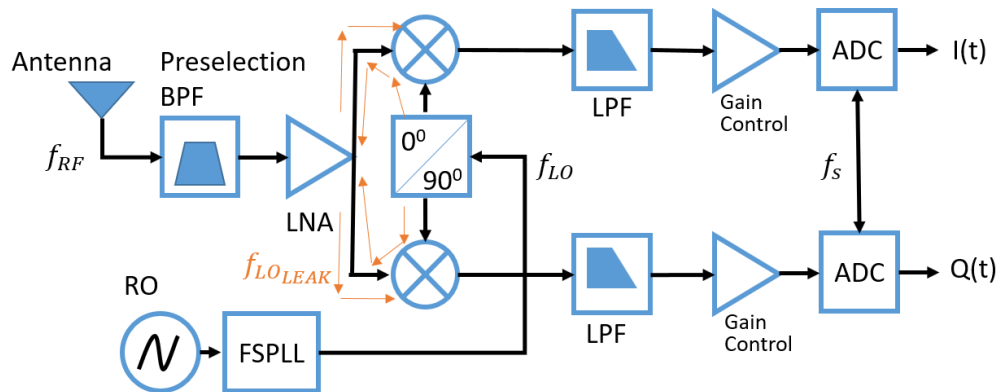


Figure 2.9.2: LO to RF Isolation at the Mixer

Similarly, if a strong interfering signal is present on the RF input at the mixer, it may couple over to the LO input if the mixer has poor RF-LO isolation. The interfering signal will then mix itself down to DC. A large DC signal after the mixer can saturate amplifiers and the ADC [6]. Low frequency phase noise or flicker noise can degrade baseband signals close to DC [6]. Flicker phase noise is discussed in Section 2.10.

There are several other deficiencies of the direct conversion architecture. Even-order nonlinearities of the circuit will result in artifacts at DC. I/Q gain and phase imbalances can distort carrier phase measurements made by the receiver. Considering an input signal with quadrature components [6]:

$$S(t) = I(t) \cos(\Omega_c t) + Q(t) \sin(\Omega_c t), \quad (17)$$

where $\Omega_c = 2\pi f_c$, and the IQ LO inputs used for mixing:

$$LO_I = 2(1 - \alpha) \cos\left(\Omega_c t - \frac{\theta}{2}\right), \quad (18)$$

$$LO_Q = 2(1 + \alpha) \sin\left(\Omega_c t + \frac{\theta}{2}\right). \quad (19)$$

α is the amplitude imbalance, and θ is the phase imbalance. Ω_c is the frequency to be down converted. The filtered $\tilde{I}(t)$ with IQ imbalance is given as:

$$S(t)LO_I = \tilde{I}(t) = (1 - \alpha) \left\{ I(t) \cos\left(\frac{\theta}{2}\right) + Q(t) \sin\left(\frac{\theta}{2}\right) \right\}. \quad (20)$$

I/Q imbalance is the result of the phase and gain discrepancies between the quadrature and real LO paths. For advanced monitoring applications, such as chip shape processing, I/Q imbalances make it impossible to separate orthogonal components. The GPS L1 C/A and P(Y) are orthogonal to one another. With I/Q imbalances, distinguishing energy between the P(Y) and C/A code is difficult.

The homodyne receiver architecture is the least complex and easiest to implement. Current RF semiconductor technology has the capability to integrate an entire direct conversion receiver onto a single monolithic microwave integrated circuit (MMIC). This greatly simplifies the schematic and PCB layout. Software defined radios have benefited

enormously from these ICs due to their flexible band selectivity, high sample rate, and low power. However, they are inadequate for high-fidelity monitoring due to the reasons described above.

2.9.2 Direct RF Sampling

The direct RF sampling receiver architecture requires the least number of analog components. Rather than down converting the desired RF signal, a high-speed ADC with a high analog input bandwidth samples the signal directly at RF. For multi-frequency receivers there would be digital channelizers and band limiting processing to get equivalent functionality of an analog-heavy architecture. There are stringent requirements for the phase noise performance for the sample clock [7]. Figure 2.9.3 displays the RF-sampling architecture.

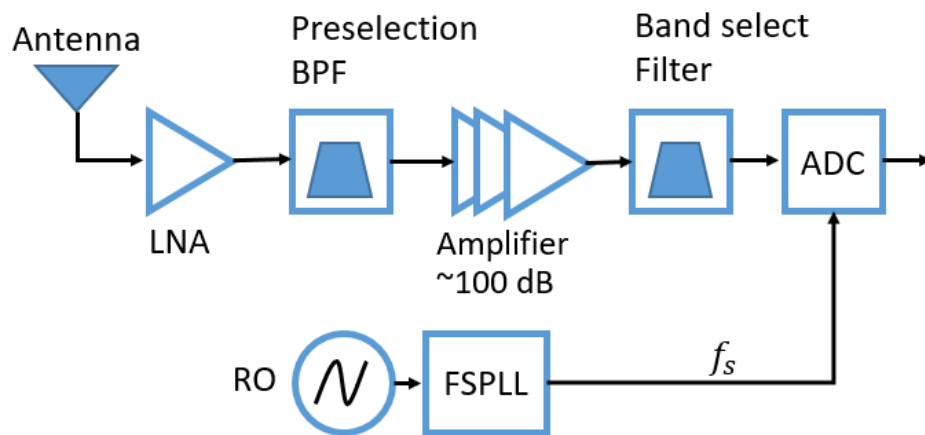


Figure 2.9.3: Direct RF Sampling Receiver Architecture

This architecture requires approximately 100 dB of gain at L-Band frequencies to amplify the thermal noise power of GNSS bands to the required minimum ADC input level. Since all this amplification must be done at RF, high input/output isolation is necessary to prevent feedback oscillation. The high gain differential must be physically separated to

achieve this isolation, thus greatly increasing the size of the front-end. Furthermore, high speed ADCs consume large amounts of power and produces large amounts of data. Intensive amounts of digital processing are then required to filter, decimate, and (optionally) store the data – further increasing power and cost.

Due to power consumption and physical size of the direct RF sampling receiver, it is a less preferable architecture for multi-element arrays.

2.9.3 Superheterodyne Receiver with Bandpass Sampling

The superheterodyne receiver with bandpass sampling (also referred to as IF sampling) converts the desired signal down to an IF where it is sampled by a high bandwidth ADC. In this case the ADC acts as a second mixer by intentionally aliasing all Nyquist zones within the analog bandwidth of the ADC. Figure 2.9.4 displays the superheterodyne block diagram.

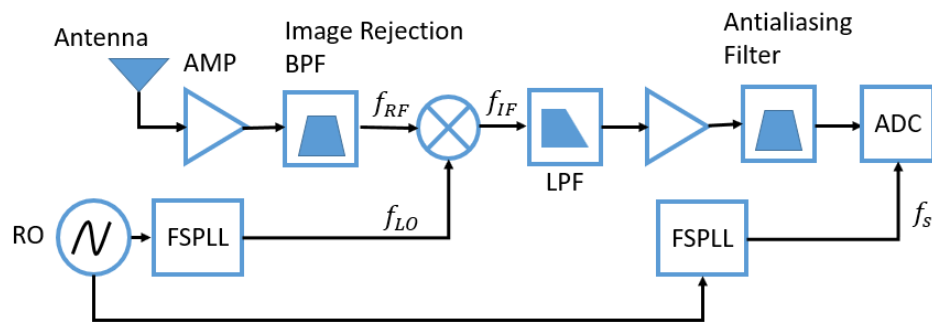


Figure 2.9.4: Superheterodyne Receiver Architecture

The front-end’s complexity is increased, as is the total number of components. However, the superheterodyne receiver with bandpass sampling has fewer signal distortions than the direct-conversion receiver and occupies much less space than the direct-sampling receiver making it better suited for multi-element implementations and

satnav signal quality monitoring and timing applications. The superheterodyne receiver is free from I/Q gain and phase imbalances because the signal is real sampled, and the conversion to baseband I/Q happens digitally.

In this architecture, the RF image rejection filter must attenuate any frequency content at the image frequency to keep it from being mixed onto the IF frequency. The phase noise and spurs of the FSPLL can degrade the satnav signal and limit the pre-detection integration time [2] and is discussed in Section 2.11. The choice of IF frequency and LO frequency are important to the performance of the receiver. By having a higher IF frequency, and thus a lower LO frequency for low-side mixing, there is greater separation of the image frequency to the RF frequency. This is an enormous benefit for the requirements of the RF image rejection filter. By increasing the distance between the RF and image frequency, the image rejection filter does not need to have a steep response, and can be a lower Q. However, having a higher frequency at IF can be a challenge to filter and match. Filters at a higher IF are more difficult to design due to parasitics of the components and lower Q factors.

2.10 Reference Oscillator

The output of the FSPLL is phase locked to the RO. The RO is essentially multiplied and divided in a closed loop to obtain a desired frequency. Any frequency offset or drift of the RO will manifest itself in the FSPLL's frequency and will need to be tracked by the receiver's satnav signal carrier tracking loops. Crystal ROs used in satnav receivers typically have good short-term frequency stability but drift over the long term. Oven controlled crystal oscillators (OCXOs) extend this short-term stability by

minimizing temperature variations – making them more desirable for instrumentation satnav receivers which require long pre-detection integration times.

A second-order random process model is used to approximate the oscillator's random walk and random frequency modulation [8]. The flicker frequency modulation is left out of the model in Figure 2.10.1.

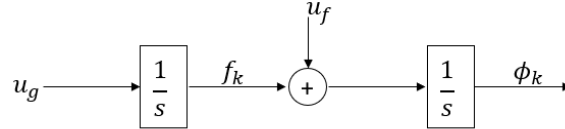


Figure 2.10.1: Two State Clock Process Noise Model [8]

The additional phase and frequency error of the oscillator are given by ϕ_{k+1} and f_{k+1} as:

$$\begin{bmatrix} \phi_{k+1} \\ f_{k+1} \end{bmatrix} = \begin{bmatrix} 1 & dt \\ 0 & 1 \end{bmatrix} \begin{bmatrix} \phi_k \\ f_k \end{bmatrix} + C \begin{bmatrix} \varepsilon_1 \\ \varepsilon_2 \end{bmatrix}. \quad (21)$$

The random process vector, ε , is normally distributed, independent, and uncorrelated. C is the Cholesky decomposition of the process noise covariance matrix Q :

$$Q = \begin{bmatrix} S_f \cdot dt + \frac{S_g}{3} \cdot dt^3 & \frac{S_g}{2} \cdot dt^2 \\ \frac{S_g}{2} \cdot dt^2 & S_g \cdot dt \end{bmatrix}. \quad (22)$$

The terms S_f and S_g correspond to the power spectral density (PSD) of the oscillator through their relationship to the Allan variance power coefficients:

$$S_f = \frac{h_0}{2}, \quad (23)$$

$$S_g = 2\pi^2 h_{-2}. \quad (24)$$

The Allan variance power coefficients are used to identify the power law noise types. In this model, we are using the white frequency modulation (WFM) term, h_0 , and the random walk frequency modulation (RWFM), h_{-2} . Modeling the flicker frequency modulation (FFM) would require an infinite amount of states to this model. However there are techniques to approximate it [9],[10]. The PSD of the phase fluctuations as a function of the power coefficients is given as:

$$S_\phi(f) = \frac{2\pi f_0}{(2\pi f)^2} \left(\frac{2\pi^2 h_{-2}}{(2\pi f)^2} + \frac{\pi h_{-1}}{2\pi f} + \frac{h_0}{2} \right) \left(\frac{\text{rad}^2}{\text{Hz}} \right), \quad (25)$$

where f_0 is the frequency of the carrier. The signal-sideband (SSB) phase noise, expressed in $\frac{dBc}{Hz}$, is in decibels with respect to the carrier. The relation between the PSD of the phase fluctuations to the carrier power ratio is [11]:

$$\mathcal{L}(f) = 10 \log \left[\frac{1}{2} S_\phi(f) \right] \left(\frac{dBc}{Hz} \right). \quad (26)$$

Some power coefficients are included in Table 2.10.1 for common oscillators used in GNSS receivers and satellites [9].

Table 2.10.1: Allan Variance Power Coefficients for Typical Oscillators

Oscillator	WFM h_0	Flicker h_{-1}	RWFM h_{-2}
Standard Quartz	2E-19	7E-21	2E-20
TCXO	1E-21	1E-20	2E-20
OCXO ₁	8E-20	2E-21	4E-23
OCXO ₂	2.51E-26	2.51E-23	2.51E-22
Rubidium	1E-19	1E-22	1.3E-26
Cesium ₁	1E-19	1E-25	2E-32
Cesium ₂	2E-20	7E-23	4E-29

The power law coefficients are used to calculate the PSD of OCXO₁ using (25) (26) is shown in Figure 2.10.2.

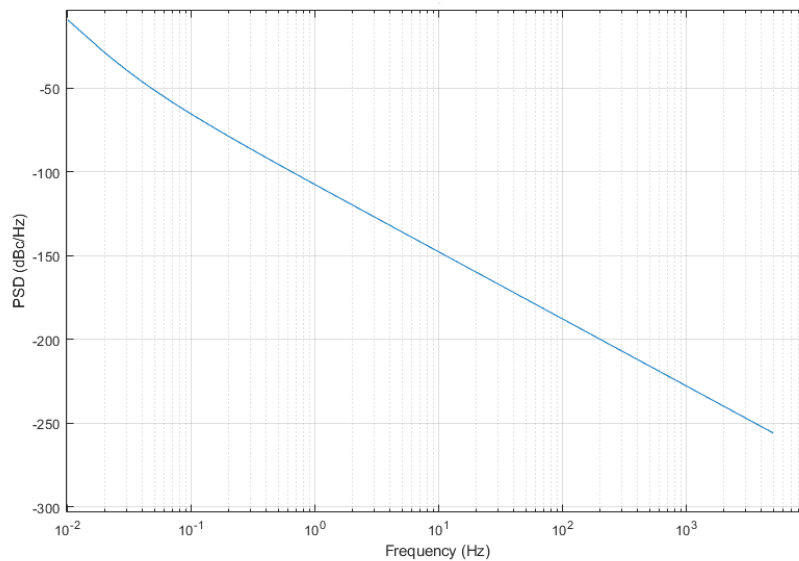


Figure 2.10.2: SSB Calculated Phase Noise of OCXO¹

The Allan variance curve can be calculated from the power coefficients from a particular oscillator through [11]:

$$\sigma_y^2(\tau) = \frac{h_0}{2\tau} + 2 \ln(2) h_{-1} + \frac{2\pi^2\tau}{3} h_{-2}, \quad (27)$$

where y denotes the fractional frequency difference from the carrier:

$$y = \frac{f(t) - f_0}{f_0} \quad (28)$$

The calculated Allan variance for the OCXO₁ is shown in Figure 2.10.3, the FFM term is left in.

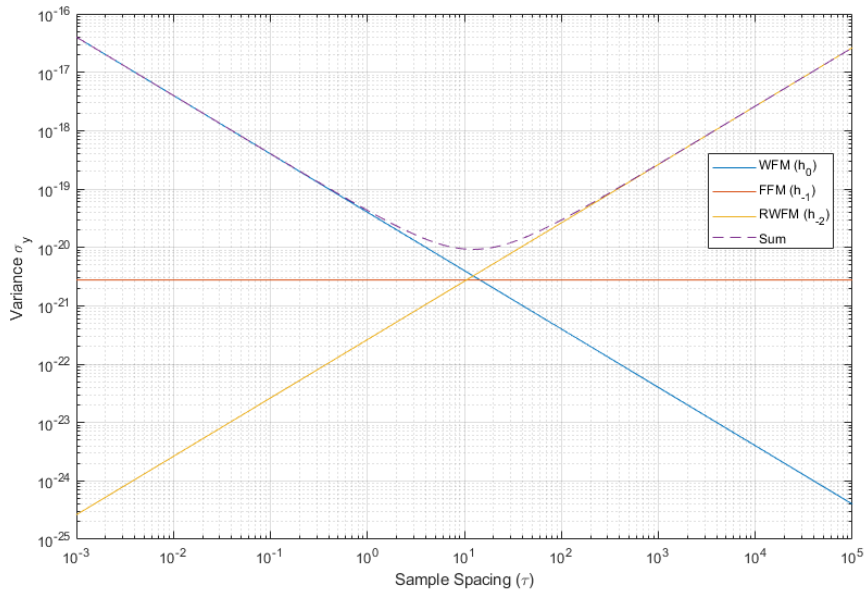


Figure 2.10.3: Allan Variance Calculation

For wide-sense stationary (WSS) and ergodic random process, the variance converges over time. For random processes with non-white frequency modulation noises, the variance of the phase fluctuations does not converge over time. Allan variance is one attempt to measure the frequency stability of oscillators that contain WFM, FFM, and

RWFM noise. The overlapping Allan variance is the most common technique and is given as [11],[8]:

$$\sigma_y^2(\tau) = \frac{1}{2(N - 2m)\tau^2}, \quad (29)$$

where $x(t)$ is the time error given as $\frac{\phi(t)}{2\pi f_0}$. Upon the discrete simulation of the clock model using the Allan Variance power coefficients from the OCXO₁ we show that the simulation matched the variance calculations from (19) as displayed in Figure 2.10.4. Note, however, that the FFM plays little effect for OCXO₁.

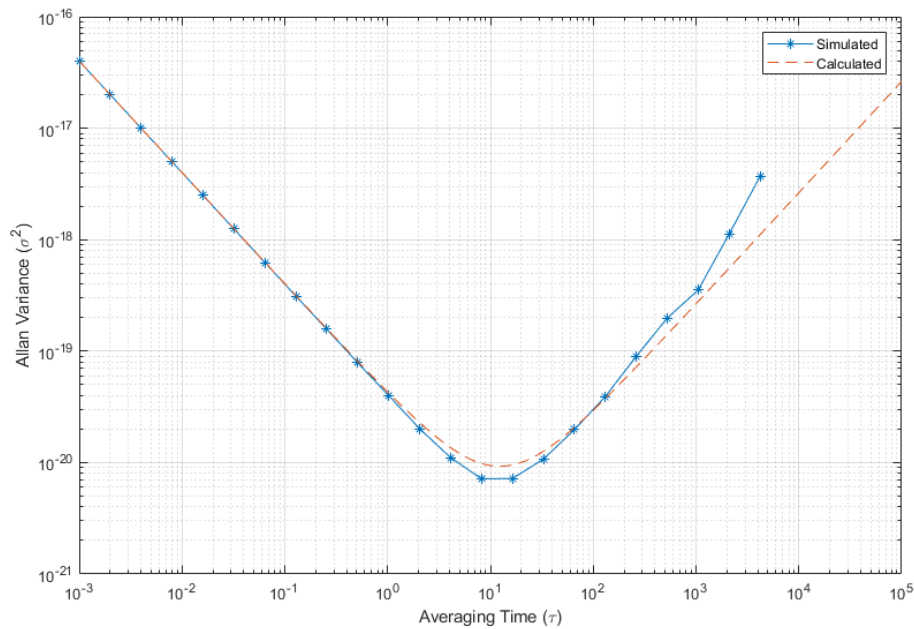


Figure 2.10.4: Simulated vs. Calculated Allan Variance

2.11 Frequency Synthesizer Phase Locked Loop

An integer-N charge pump phase locked loop (PLL) with integrated voltage-controlled oscillator (VCO) circuit diagram is displayed in Figure 2.11.1. To control the

output frequency, digital dividers $1/N$ and $1/M$ are used to divide the RO and VCO frequency to a common value f_{PFD} before the phase-frequency-detector (PFD). The PFD compares the phases of RO and the VCO. The phase error, output as positive or negative voltage pulses, whose widths are proportional to the error is used to switch constant current sources within the charge pump. The charge pump's signal is filtered with the loop filter to obtain an error voltage. This error voltage is used to adjust the frequency of the VCO such that the phase error is driven to zero. The loop filter is a low pass filter and is used to set the tracking performance, lock time, and phase noise characteristics of the FSPLL [12]. Altering M or N causes the PLL to lock to a different frequency. The output frequency of the PLL is given by:

$$f_{out} = \frac{Nf_{RO}}{M} \quad (30)$$

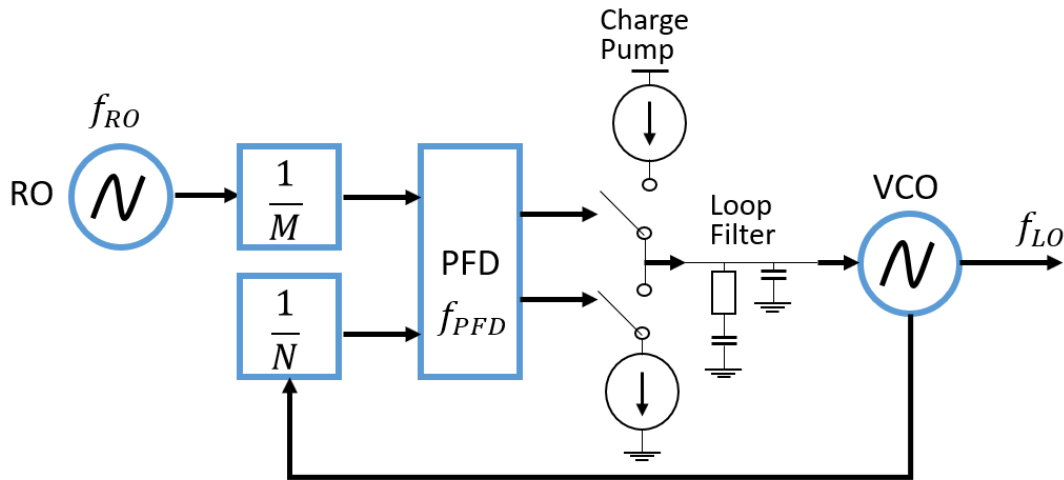


Figure 2.11.1: Integer-N PLL with 2nd-Order Loop Filter

The VCO output frequency is used as the LO, and is divided by N to match the frequency of the RO. The PFD makes phase comparisons between the LO and the divided VCO. The

PFD makes comparisons at a rate of f_{PFD} . The PFD control signals are then converted into a control current by the charge pump and filtered by the loop filter before controlling the VCO.

The closed-loop linear time-invariant (LTI) phase domain model of the PLL is displayed in Figure 2.11.2. It describes the relative additive phase noise to the model introduced by the PFD, RO, and VCO components [13],[2],[14].

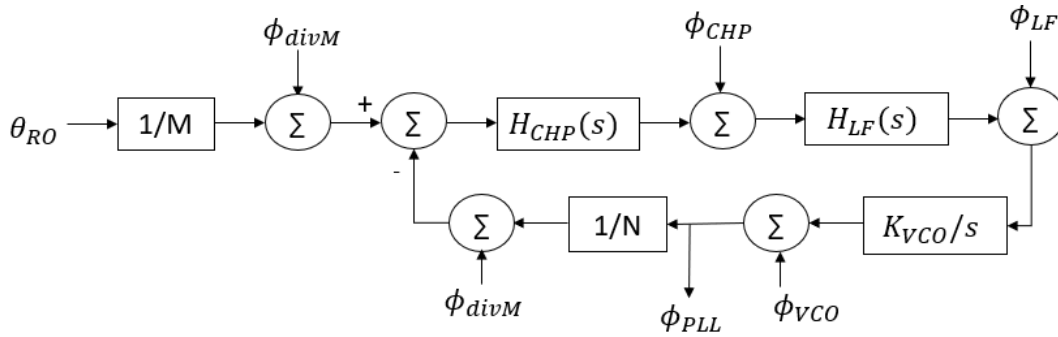


Figure 2.11.2: LTI Phase Domain Model with Additive Noise Sources

From Figure 2.11.2, θ_{RO} is the phase of the reference oscillator including phase noise. ϕ_{divM} , ϕ_{CHP} , ϕ_{LF} , ϕ_{VCO} and ϕ_{divM} are additive random processes that contribute to the phase error of the system. ϕ_{PLL} is the output phase of the LTI Phase Domain Model. $H_{CHP}(s)$ is the transfer function of the charge-pump, and can be modeled with a scalar current source. $H_{LF}(s)$ is the loop filter transfer function. Open loop transfer functions for the VCO, RO, and PFD are derived as [2],[14]:

$$H_{VCO}(s) = \frac{sN}{sN + I_p K_{VCO} H_{LF}(s)}, \quad (31)$$

$$H_{RO}(s) = \frac{NI_p K_{VCO} H_{LF}(s)}{M (sN + I_p K_{VCO} H_{LF}(s))}, \quad (32)$$

$$H_{PFD}(s) = \frac{2\pi N K_{VCO} H_{LF}(s)}{sN + I_p K_{VCO} H_{LF}(s)}, \quad (33)$$

where the loop filter transfer function is $H_{LF}(s)$, and s is the complex frequency parameter of the system. M and N are the dividers for matching the reference's frequency to the VCO's frequency before the PFD. I_p (A) is the charge pump current, this is typically a programmable value for modern FSPLLs. K_{VCO} is the gain of the VCO expressed in Hz/V. The loop filter transfer function, $H_{LF}(s)$, high passes the phase noise from the VCO and low passes the phase noise from the RO to the output. The total PSD of the FSPLL can be calculated through [2]:

$$P_\phi(f) = P_{\phi VCO}(f) + P_{\phi RO}(f) + P_{\phi PFD}(f), \quad (34)$$

$$P_{\phi VCO}(f) = |H_{VCO}(f)|^2 |H_{ii}(f)|^2 4\pi^2 f_{c,vco}^2 c_{w,vco}, \quad (35)$$

$$P_{\phi RO}(f) = |H_{RO}(f)|^2 |H_{ii}(f)|^2 4\pi^2 f_{c,ro}^2 c_{w,ro}, \quad (36)$$

$$P_{\phi PFD}(f) = |H_{PFD}(f)|^2 c_{w,pfd}. \quad (37)$$

$H_{ii}(f)$ is an ideal integrator transfer function. $f_{c,vco}$, and $f_{c,ro}$ are the frequencies of the VCO and RO respectively. $c_{w,vco}$ and $c_{w,ro}$ are spot phase noise models of their respective devices [2], [13]. The phase noise of the RO is low passed and the phase noise of the VCO is high passed by the loop filter. Thus, to best minimize the amount of phase noise

contributed by the VCO and PFD, the loop filter should have an equivalent bandwidth of where the VCO phase noise intersects the noise floor of the FSPLL [12]. Passive filters are ideal for low phase noise applications; a passive component-based second-order filter's transfer function is [12]:

$$H_{LF}(s) = \frac{1 + sC_2R_2}{s(C_1 + C_2) \left[1 + s \left[\frac{C_1C_2R_2}{C_1 + C_2} \right] \right]} \quad (38)$$

Figure 2.11.3 shows the calculated and measured PSD for the LMX 2582 integrated-VCO FSPLL IC [15] in its first configuration, which is further discussed in Section 4.4.

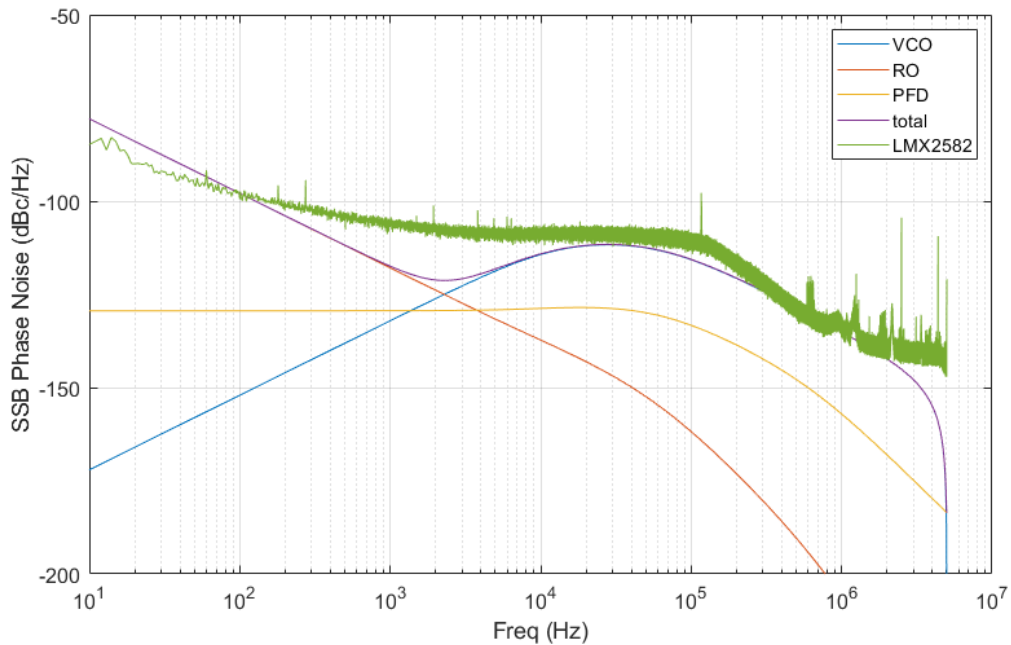


Figure 2.11.3: FSPLL Simulated Phase Noise and Measured Phase Noise from LMX 2582
In its 1st Configuration

The model is a close approximation of the phase noise from the LMX2582's 1st configuration in Chapter 4.4: Frequency Synthesizer Evaluation. However, this is not

adequate to be able to gain detailed insight into vendor-specific devices, or other features that are not included in the FSPLL model. An instrumentation grade receiver benefits from the lowest possible phase noise from an FSPLL. Thus, it is more beneficial to the community to conduct measurements on vendor's evaluation boards. Vendors also supply tools to aid frequency synthesizer design for their specific devices, which may provide a more accurate phase noise model than (26).

Figure 2.11.3 shows that the RO is the greatest contributor to the close-in phase noise (i.e. phase noise at frequencies < 100 Hz offset from center). The PFD dominates around 10^3 to 10^4 Hz while the VCO is dominant $>10^4$ Hz. Of course, the bandwidth of the loop filter, $H_{LF}(s)$, determines how the phase noise of the respective devices are passed to the output.

2.12 Group Delay Variations

Group delay is the derivative of the phase response of a device under test (DUT) with respect to frequency. It is the time it takes for a wave of a given frequency to propagate through a DUT:

$$\tau_g(\omega) = -\frac{d\phi(\omega)}{d\omega}. \quad (39)$$

Depending upon the application, group delay can become a problem. If the group delay variation of a filter is changing due to temperature changes, then the group delay will change all the pseudoranges by the same amount. This effectively comes out as a clock error. The position is not affected. The position derivation can be affected for FDMA signals like GLONASS. Each SV's signal centered at a different frequency will

experience a different delay in the front-end. This will manifest itself as a position error if the group delay is not accounted for.

Advanced monitoring applications such as chip transition characterization, otherwise known as “chip-shape” [1], [3], requires minimum group delay variations over the front-end passband. Delay variations over the passband adds distortions to the signal that are not characteristic to the satellite. Shorter spreading codes, such as GPS C/A (1023 chips) and GLONASS C/A (511 chips) are most impacted by these group delay variations due to the wider-spread and overall smaller number of spectral lines in the spreading code’s PSD that can lead to inter-PRN pseudorange biases [4],[5]. The spacing between spectral lines of a pseudorange sequence is inversely proportional to the period of the sequence. As spreading sequences become longer, the group delay variations in the front-end’s passband becomes less of an issue [16].

2.13 RF Filters for Satnav Instrumentation

There are several types of RF filters that suitable for satnav applications. The surface acoustic wave (SAW) filter, the cavity filter, distributed element, and the ceramic cavity filters offer different performance, cost, size, and weight. The SAW filter is the cheapest and the smallest. Unfortunately, the SAW filter is not appropriate for instrumentation satnav receivers due to large group delay variations in the passband and sensitivity to temperature changes. SAW filters offer an excellent brick wall response, but may not offer enough attenuation in the stopband, especially at higher frequencies. Cavity filters are the most expensive and offer the best frequency response. However, their large size and weight does make them ideal for size and weight constrained designs. Distributed

element filters can be built onto the PCB substrate but will take up large amounts of space for L-Band signals. Ceramic cavity filters can be custom ordered and PCB mounted. The response and group delay variations are consistent over temperature.

The RF filter's purpose is to select the band of interest and attenuate any out-of-band interference. The RF filter's other purpose is image rejection for superheterodyne receivers. As stated in Section 2.7, group delay variations over the passband of the filter need to be minimized.

2.14 IF / Antialiasing Filters

The construction of the antialiasing filter prevents outer-band interference from aliasing into the sampled signal. The filter response shape should have at least 74 dB of attenuation outside the passband of the filter to prevent the ADC from quantizing outside interference. This number is derived from the ENOB and dynamic range of the ADC. The filter also adds its own group delay to the signal that must be minimized. Surface acoustic wave (SAW) filters may have a brick wall response, but the group delay variations within the passband can be extreme making them non-ideal for instrumentation-grade satnav signal monitoring applications [3]. The group delay of SAW filters is also highly temperature dependent, adding error in advanced timing applications [4]. Specially tuned inductor-capacitor (LC) filters can have a reasonably flat group delay response in the passband that does not vary as much as SAW filters over temperature [4]. The drawback is being able to design a filter with practical LC components that meet the stopband attenuation, passband width, and reasonably small size. For example, high-Q inductors are desired to obtain a sharp stopband response. However, the highest realizable Q inductors

tend to be air-core types which are much larger in size compared to ferrite-core types. Air-core inductors are also more sensitive to temperature variations, and have wider variations on labeled value (i.e. tolerances) due to manufacturing variations.

2.15 Receiver Carrier Tracking Loops and Errors

Tracking loops are used to recover the satnav signal's parameters. The carrier tracking loops are responsible for recovering the phase and Doppler of the satnav signal. Code tracking loops are responsible for recovering the satnav signal's code phase. From these raw observables carrier phase and pseudorange measurements can be derived, respectively [17]. A satnav receiver channel's carrier tracking loop is displayed in Figure 2.15.1.

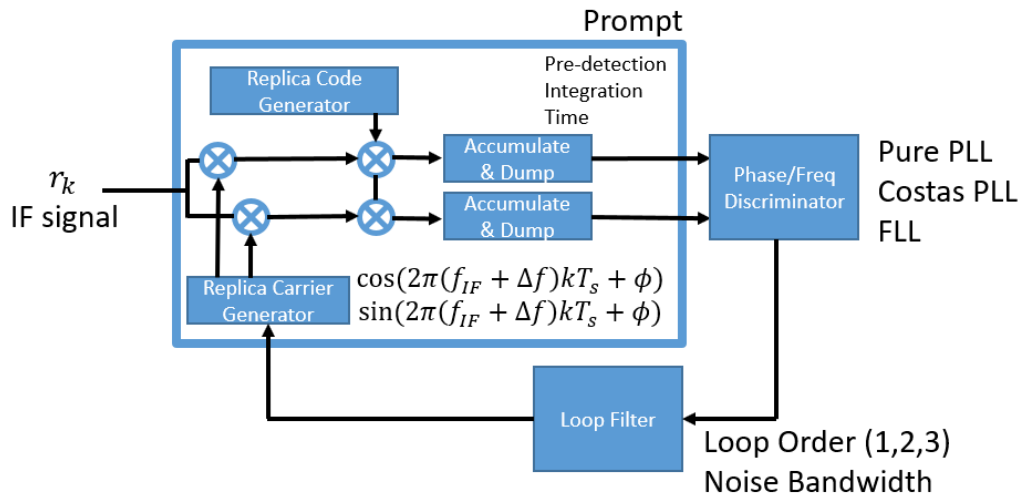


Figure 2.15.1: Receiver Carrier Tracking Loop

Thermal noise present on the sampled IF signal results in errors on the phase/frequency discriminator. The loop filter low pass filters the phase estimates from the discriminator and steers the replica generator. The thermal noise contributions for a pilot (no data) and data-containing channel are given as [17]:

$$\sigma_{t_{PLL_P}} = \frac{360}{2\pi} \sqrt{\frac{B_N}{CNR}} \text{ (degs)} \quad (40)$$

$$\sigma_{t_{PLL_D}} = \frac{360}{2\pi} \sqrt{\frac{B_N}{CNR} \left(1 + \frac{1}{2T * CNR}\right)} \text{ (degs)} \quad (41)$$

Phase noise produced by the FSPLL, ADC clock, and RO degrade the SNR of the carrier tracking loops [2], [17], [18]. The phase noise is introduced by the RO and can be quantified in terms of the Allan deviation of the oscillator, vibration or mechanical stress. The tracking threshold for the PLL tracking loop for a two-quadrant (Costas) discriminator for a data channel is [17]:

$$\sigma_{PLL_D} = \sqrt{\sigma_{t_{PLL_D}}^2 + \sigma_V^2 + \theta_A^2} + \frac{\theta_e}{3} \leq 15^\circ \quad (42)$$

where σ_V^2 is the Allan variance induced phase noise of the RO and θ_A^2 is the vibration-induced phase noise. The vibration induced phase noise is treated as negligible in this study since satnav monitoring applications are assumed to be stationary. The contributions of the Allan variance to the phase estimate is given as [18],[5],[19],[20]:

$$\sigma_V^2 = \frac{1}{2\pi} \int_0^\infty S_v(\omega) |1 - H(\omega)|^2 d\omega. \quad (43)$$

$S_v(\omega)$ is the oscillator phase noise PSD, modeled by the Allan variance clock parameters. $|1 - H(\omega)|^2$ is the inverse magnitude response of the carrier tracking loop filter and is dependent upon the loop order and noise bandwidth. It is also defined as [18]:

$$|1 - H(\omega)|^2 = \frac{\omega^{2n}}{\omega_L^{2n} + \omega^{2n}}, \quad (44)$$

where n is the loop order and ω_L^{2n} is dependent upon the loop filter values. Typical values are displayed in Table 2.15.1 [17], [18]. Where B_L is the loop noise bandwidth.

Table 2.15.1: Typical Loop Filter Values

Loop Order	Typical Filter Values
1 st	$\omega_L = 4B_L$
2 nd	$\omega_L = 1.885B_L$
3 rd	$\omega_L = 1.20B_L$

Long pre-detection integration intervals (T_{PDI}) and narrow loop bandwidths are essential to making sensitive measurements. However, the SNR of the correlation peak will begin to decrease for longer integration times due to RO instability. If the dynamics of the RO are greater than the receiver's tracking loop bandwidth then cycle slips can occur [5], [17]. Cycle slips can result from loss of lock of the tracking loop. A cycle slip is an integer cycle of the satnav signal that has not been tracked. The wavelength of L1 is approximately 19 cm; a cycle slip results in a 19 cm error in the carrier-phase pseudorange.

The FSPLL is responsible for multiplying the RO frequency to be used as the local oscillator (LO). Excessive phase noise introduced by the FSPLL degrades the SNR and reduces the resolution (i.e. sharpness) of the correlation peak [2]. This adds noise to the phase estimate of the local replica and degrades the receiver's carrier phase measurements.

The phase lock detector [21] is a measurement that can indicate the quality of the loop filter measurements. The phase lock detector (PLD) is given by the ratio of the narrow band power (NBP) and narrow band difference (NBD) as:

$$NBD_m = \left(\sum_{i=1}^M I_i \right)_m^2 - \left(\sum_{i=1}^M Q_i \right)_m^2, \quad (45)$$

$$NBP_m = \left(\sum_{i=1}^M I_i \right)_m^2 + \left(\sum_{i=1}^M Q_i \right)_m^2, \quad (46)$$

$$PLD_m = \frac{NBD_m}{NBP_m}, \quad (47)$$

where I_i and Q_i are the in phase and quadrature phase magnitude after the coherent integration time. At phase lock, all the tracked signal's power is in the I correlator, maximizing NBD. If there is complete phase lock, the NBP and the NBD will be the same, and the PLD will be unity, indicating perfect phase lock.

III. Methodology

3.1 Chapter Overview

The aim of this thesis is to design, fabricate, and test a satnav front-end receiver capable of instrumentation grade characterization of satnav signals. The front-end of any RF receiver is responsible for frequency selectivity, frequency translation, and digitization. A high-fidelity front end preserves the original signal characteristics and contributes as little noise, distortion and colorization as possible given the specified dynamic range of operation. The front-end design shall also support multi-element antenna arrays for obtaining spatial and polarization information about an environment.

An instrumentation satnav receiver must be able to make high fidelity measurements under the duress of strong interference and signal fading. The satnav receiver is designed to handle 100 dB Jamming-to-Signal ratio (J/S) while preserving linearity of the components in the signal path. Filters at RF and IF frequencies contribute group delay distortions to the received satnav signal. Group delay variations causes inter-pseudorange biases for short PRN codes and also contribute chip-shape deformations to the nominal satnav signal [4]. Satnav signals from the USAF's GPS are broadcast in three separate bands, L1, L2, and L5. The methodology for an L1 RF front-end is covered here. The same procedure will apply to the other bands. The key focus points of the design methodology are:

- Frequency plan with +50 MHz of usable bandwidth for wideband satnav signal monitoring.
- Minimal group delay variations over the passband contributed by the filters.

- Configuring a FSPLL for minimal phase noise and spurs.
- Gain control and preserving linearity of the front-end.

3.2 Receiver Architectures

The first task in designing a satnav receiver front-end is to derive the frequency plan. There are several receiver architectures used in satnav receiver front-ends: direct-sampling, direct-conversion, and superheterodyne.

The superheterodyne receiver architecture with bandpass sampling was chosen for superior selectivity, linearity, and sensitivity over the direct conversion receiver. The superheterodyne may be more complex than the direct sampling receivers, however, the superheterodyne consumes less power and space. Power and space consumption is important for employing multielement antenna arrays.

The next step in defining the frequency plan is to conduct a market assessment of available RF parts from major industry vendors. In building a satnav receiver with PCB surface mount components we benefit from the wide range of available parts that target the many wireless communication industries. Perhaps the most important part to select first is the analog-to-digital converter (ADC), as the sampling rate will drive the frequency plan for the receiver.

3.3 Analog to Digital Converter

For multi-element arrays, to perform digital beamforming, each antenna needs to be sampled coherently. An ADC with multiple channels, high sample rate, high analog input bandwidth, and high dynamic range is best suited for an instrumentation satnav receiver. Analog Device's AD9681 [22] has eight ADC channels, a sample rate of 125 MSPS per

channel, and 14 bits of dynamic range integrated into a single IC package. By integrating all of the ADC channels into a single package, each input channel can be coherently sampled, greatly reducing design complexity. The AD 9681 has an analog input of 650 MHz allowing for subsampling in higher Nyquist zones.

Figure 3.3.1 shows the different Nyquist zones for the AD9681 with a sample rate of 125 MSPS. The sample bandwidth of the AD9381 is 62.5 MHz. The excessive amount of bandwidth has several benefits to the receiver. The RF satnav signal does not need to be downconverted in the exact center of a Nyquist zone. This allows for the LO to be an integer multiple of the RO, greatly improving spurs and phase noise. The RF image rejection filter and antialiasing filter are wider in bandwidth. Because group delay variations are higher at the edges of filters and relatively flat in the center; the variations over the satnav signal in the center of the passband are decreased.

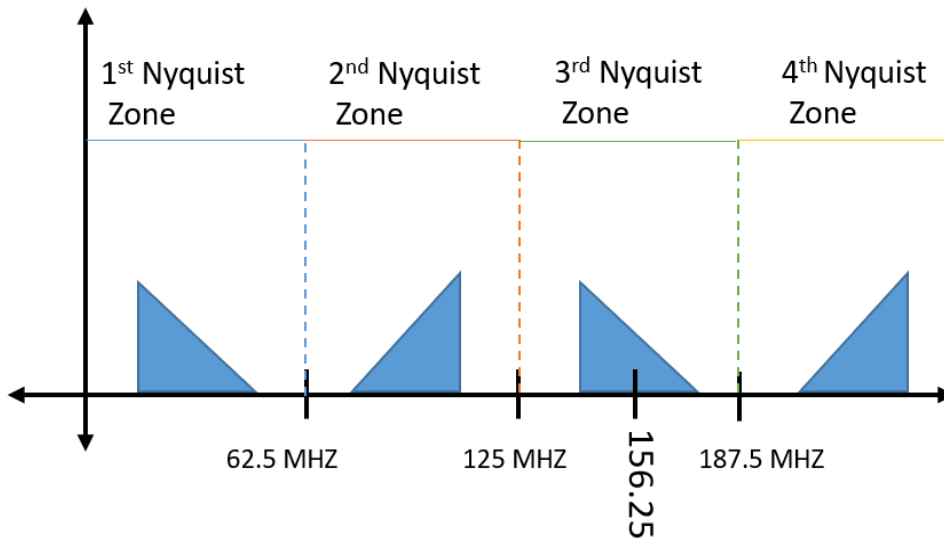


Figure 3.3.1: Nyquist Zones of the Analog Devices AD 9681 ADC

If the IF were to be placed in the 1st Nyquist zone, there may be frequency overlap between the negative and positive frequency components of the signal due to the

performance of the RF image rejection filters. Frequency content overlap would be detrimental to the SNR of the satnav signal. Figure 3.3.2 displays how the antialiasing filter and RF filter may inadequately prevent contamination between the positive and negative frequency components of the signal. Shown in orange is the filter response of the antialiasing filter, and in blue, the response of the RF filter.

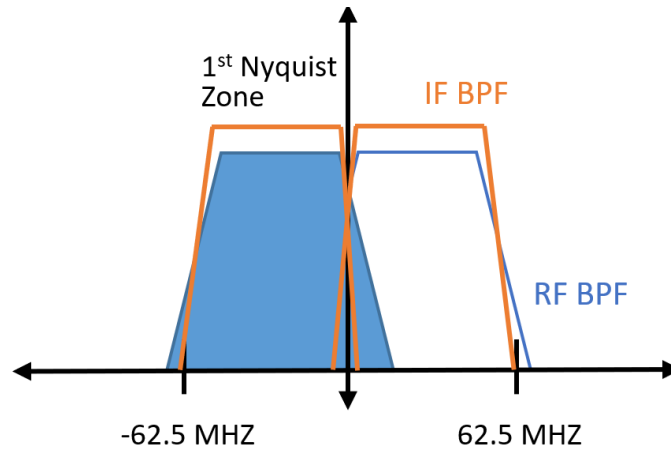


Figure 3.3.2: 1st Nyquist Zone Frequency Overlap

The third Nyquist zone was chosen as the IF due to having over 200 MHz of separation from the translated negative frequency. Having a higher IF frequency also increases the distance between the desired signal and its image frequency. The image frequency is centered at 1269 MHz. By having a larger separation between the desired signal and the image, the response of the RF filter does not need to have a brick wall response.

The 3rd Nyquist zone is centered at 156.25 MHz. When sampled, the Nyquist zones are aliased into the quantized signal. A 50 MHz antialiasing BPF is needed for the 3rd Nyquist zone to prevent outside interference from aliasing into the sampled signal. A 50 MHz filter gives 6.25 MHz for the roll-off of the filter; this ensures adequate attenuation of out-of-band interference. A wider bandwidth filter allows for a flatter group

delay response in the center of the filter. Figure 3.3.3 displays the down converted signal in blue and the 50 MHz antialiasing filter in orange.

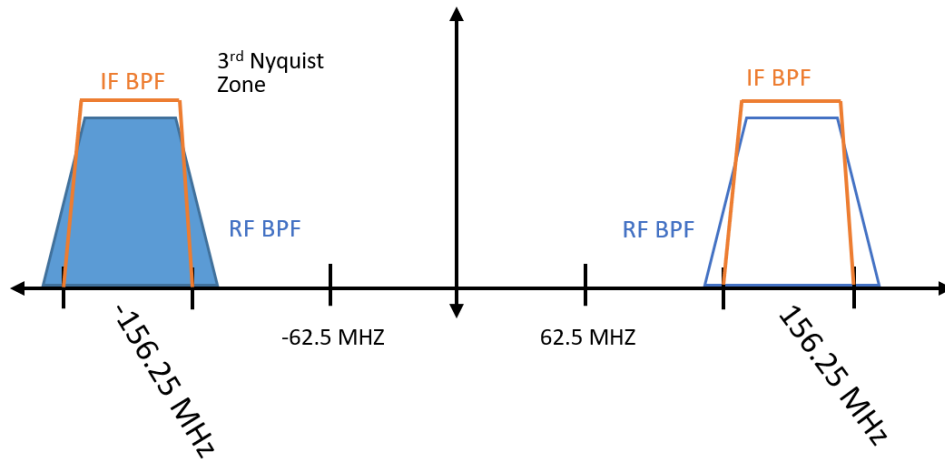


Figure 3.3.3: 3rd Nyquist Zone Frequency Response

To convert the L1 center frequency of 1575.42 MHz down to 156.25 MHz an LO of 1419.17 MHz is needed. However, as we will see in Section 3.7, synthesizing the exact frequency of 1419.17 MHz can increase the amount of phase noise from the FSPLL. Instead, an LO 1420 MHz is used for down conversion because it is an integer multiple of the RO (10 MHz). Figure 3.3.4 displays the frequency plan for L1.

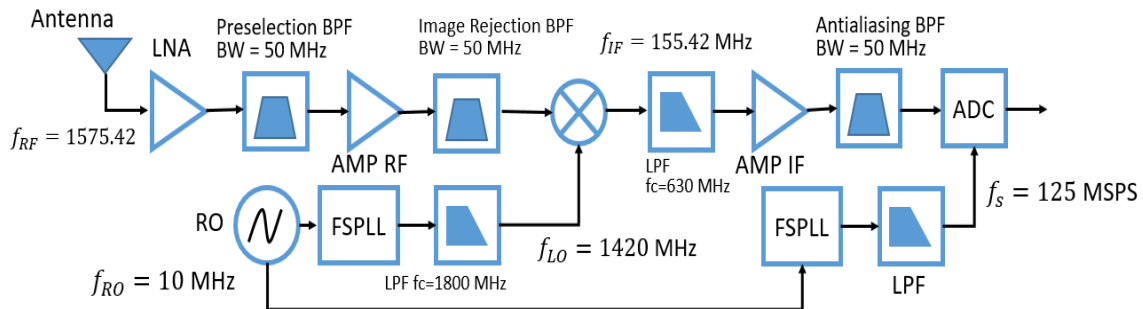


Figure 3.3.4: Frequency Plan of the Receiver Front-End

To down convert the L2 center frequency of 1227.60 MHz to 156.25 MHz an LO of 1071.35 MHz is needed. However, using an LO frequency of 1070 MHz from the frequency synthesizer will result in better phase noise performance. To down convert the L5 center frequency of 1176.45 MHz to 156.25 MHz a LO of 1020.20 MHz is needed. To improve phase noise, a LO of 1020 MHz can be used. The AD9681 operates off a 1000 MHz clock that is divided internally to a sampling frequency of 125 MHz.

The ADC has 14 bits of dynamic range. This equates to 84.3 dB of dynamic range (6 dB per bit). However, the two least significant bits are dominated by ADC background noise, giving an effective 72 dB of dynamic range. This will be important in the later design of some components. For full scale quantization, the ADC can handle up to 2 V peak-to-peak. The load is 50 Ω . The maximum input power required for full-scale excitation of the ADC is given by:

$$\left(\frac{1}{\sqrt{2}}\right)^2 \left(\frac{1}{50}\right) = 0.01 W = -20 dBW = 10 dBm. \quad (48)$$

3.4 Bandpass Antialiasing Filter

The construction of the antialiasing filter prevents outer-band interference from aliasing into the sampled signal. The filter response shape should have at least 74 dB of attenuation outside the passband of the filter to prevent the ADC from quantizing outside interference. The filter also adds its own group delay variations to the signal that must be minimized. Specially tuned LC filters can have a flat group delay response in passband that does not vary over temperature. The drawback is being able to design a filter with

realizable LC components that meet the stopband attenuation, group delay, and 3 dB bandwidth.

Group delay variations will be greatest at the edges of the passband; these variations are inevitable. The variations at the center of the filter should be as small as possible to prevent signal deformations. A high sample rate works to our advantage by allowing for higher bandwidth bandpass filters thus decreasing the amount of group delay variations over the satnav signal's bandwidth. Once the IF signal has been sampled and quantized, a finite impulse response (FIR) filters can be used to compensate for group delay variations or extract the usable portion of the spectrum. Afterwards the signal can be decimated to reduce DSP clock speed.

Filter design software exists for designing LC bandpass filters. Keysight Genesys is one tool that offers a good filter design software. Modeling of the real components' quality factor (Q), inductance, and parasitics at the designed frequency is difficult because they are dependent on the individual vendor's components. Modelithics [23] is a company that measures the S-parameters of many vendor's components and sells accurate models for designers to best utilize them. Genesys has the capability to utilize these models in their Vendor Part Synthesis (VPS) tool [24]. First the filter is designed using ideal LC components with high-Q and no parasitics. Next the designer specifies what component libraries to use. The VPS tool then tries to fit the Modelithics component models to the ideal LC filter response.

A 50 MHz, 9th order Cauer-Chebyshev minimum inductor filter was designed with the Genesys filter design software. The low frequency cutoff is 131.25 MHz and the upper

181.25 MHz with a minimum stopband attenuation of 75 dB. Figure 3.4.1 shows the filter response of the ideal filter.

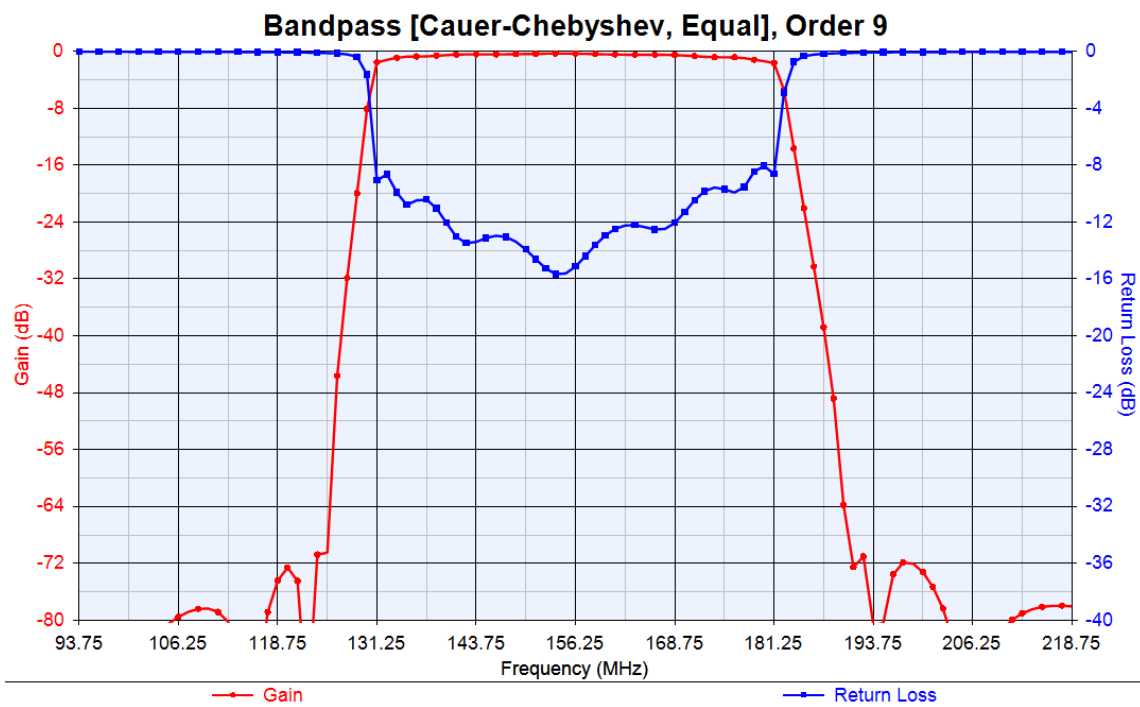


Figure 3.4.1: Genesys IF Filter Using Theoretical Components

Next the filter is designed with the VPS tool. Inductor components were chosen from Coilcraft’s 0908SQ air core line and the 1206CS ceramic chip inductors. These components covered the range of inductance needed to design the filter and had a high Q at the IF. The tool selected the best components to match the ideal response. The capacitors were modeled as ideal components due their inherent high-Q and high self resonate frequency (SRF). Figure 3.4.2 displays the filter response of the VPS tool and the response using ideal components.

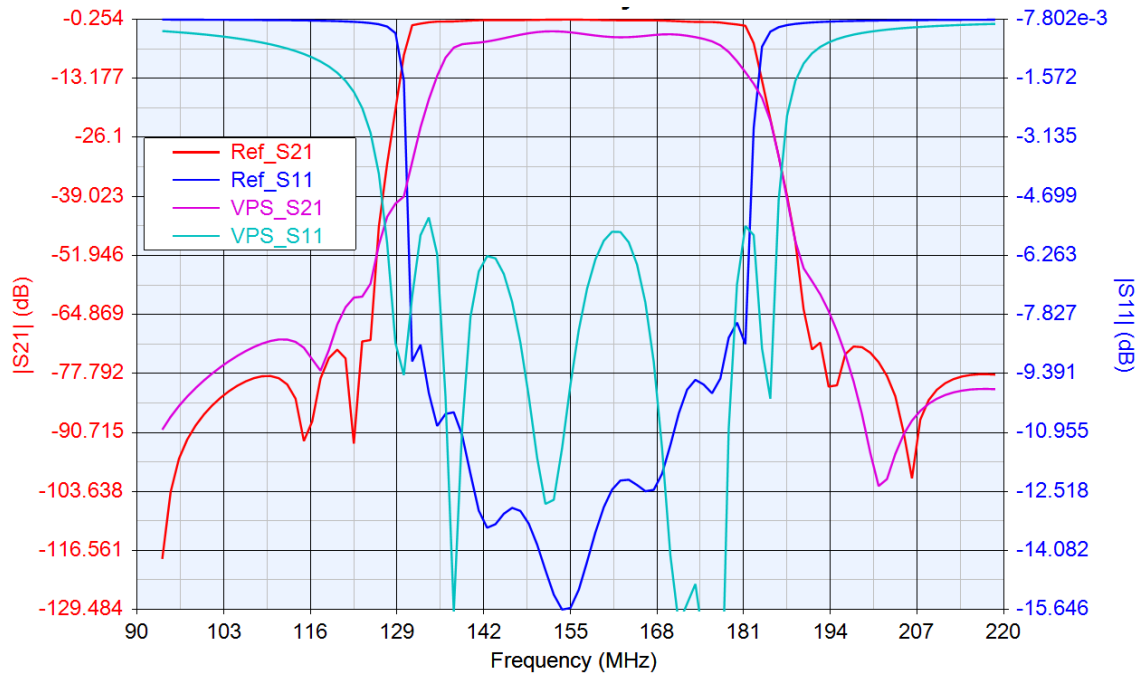


Figure 3.4.2: Frequency Response of Vendor Part Synthesis and Theoretical of IF Filter

There is a higher insertion loss using the actual component models over the ideal. This is due to the Q-factors of the inductors being lower at higher frequencies. There are also higher reflections from VPS design. Figure 3.4.3 shows the group delay from the ideal and VPS design.

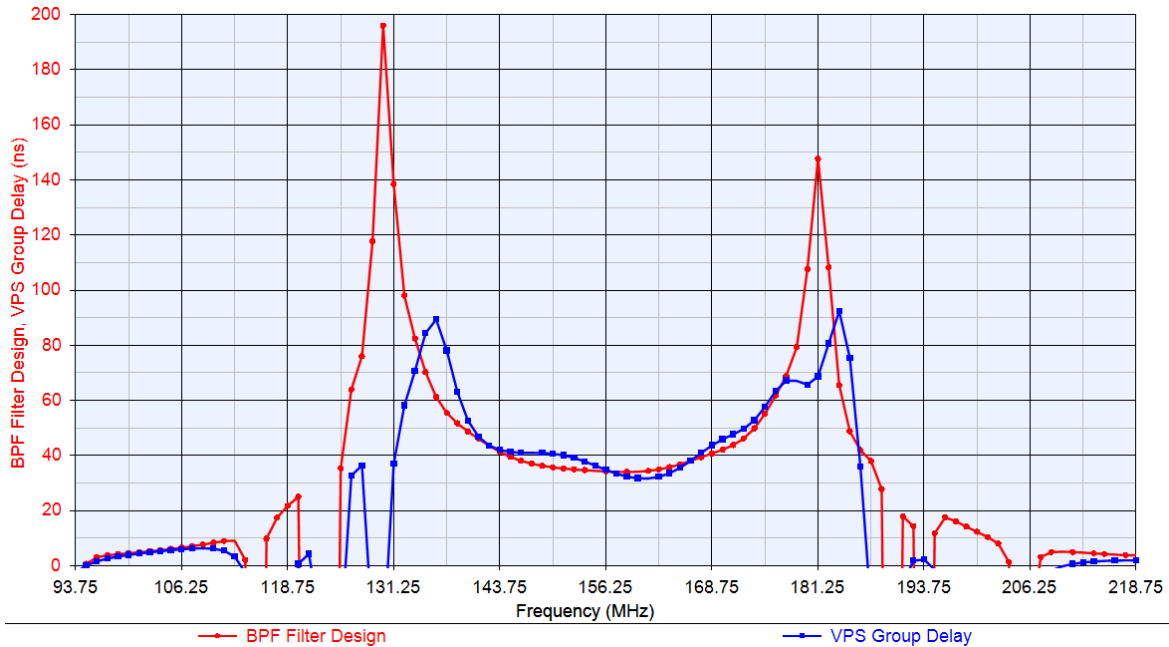


Figure 3.4.3: Group Delay Response of Vendor Part Synthesis and Theoretical Design of IF Filter

The group delay variation in the passband is of greatest concern, rather than the total delay. More analysis and tweaking of the IF filter can be done to reduce the group delay variation. Currently there is 10 ns of variation within the passband of the satnav signals.

3.5 RF Image Rejection Filter

The L1 satnav signal centered at 1575.42 MHz is low side mixed down to an IF of 155.42 MHz with an LO of 1420 MHz. Due to the low side injection mixing, the image frequency is centered at 1265.58 MHz. The center of the image is also down converted to the IF. If not adequately attenuated by an image rejection filter, any RF interference that is present at the image frequency will be sampled by the ADC, decreasing SNR. The L-band is a very spectrally dense band; it has many users and applications. Because received

satnav signals are below the thermal noise floor, RF interference present at the image frequency that is not attenuated will degrade the SNR. Therefore, the RF image rejection filters must attenuate interference at the image frequency to prevent it being sampled by the ADC.

The RF image rejection filter must also attenuate adjacent channel interference that is present. Signals that are not directly present in the L1 satnav band, but have a large signal power, may saturate components in the signal path if not filtered.

The ceramic cavity resonators have a higher dielectric constant than air, allowing for smaller cavity resonators than air filled. Cavity filters are ideal because of their small size, ease of manufacturability, and ability to be surface mounted on a PCB.

Lorch Microwave, now Smith's Interconnect, manufactures custom ceramic cavity filters to meet the designers need. Group delay variations need to be minimized in the pass band. The filter also needs over 70 dB of attenuation at the image frequency. The 70 dB of attenuation ensures that when the ADC has full scale input power, there is zero energy from the image frequency being digitized. The designer has ability to specify the number of resonator sections, the resonator size, center frequency and the 3 dB bandwidth. For L1 satnav signals, the front-end needs 50 MHz of 3dB bandwidth and a center frequency of 1575.42 MHz. Increasing the number of resonator sections increases the group delay variations while improving roll off. Filters of 5, 4, and 2 resonators were simulated in Genesys. Image rejection and group delay were assessed. Smaller resonator sizes are preferred for the PCB layout.

Only the RF filters and a low pass filter after the mixer are shown in the simulation. The antialiasing filter is not simulated. The schematic of the 5 resonator circuit is shown in Figure 3.5.1.

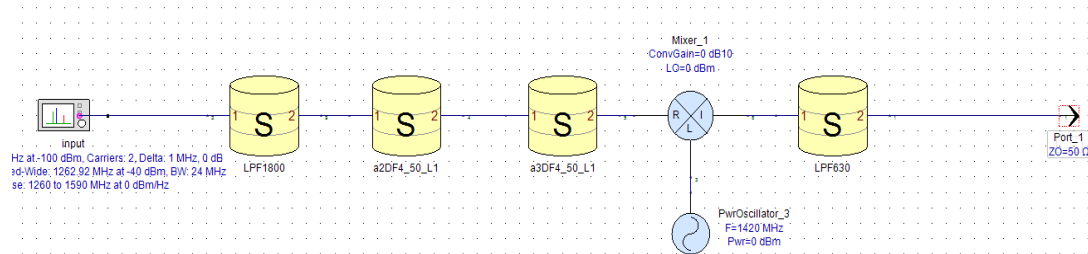


Figure 3.5.1: Group Delay, Image Rejection, and Frequency Response of RF Filter Configurations

A MiniCircuits low pass filter with a cutoff of 1800 MHz is followed by the two RF filters that are being evaluated. A mixer down converts the signal to an IF of 155.42 MHz and a second MiniCircuits low pass filter with a cut off of 630 MHz filters further. The scattering parameters were obtained from the vendor’s website. A spectrum sweep is performed over the s-parameters of the circuit. A 0 dBm signal is swept from 1200 MHz to 1700 MHz. Figure 3.5.2 shows the sweep performed on the signal path with 5-resonator components. Under this test, the desired signal at 1575.42 MHz and the image signal at 1265.58 MHz have the same power. In the real world this will not be the case, as any signals present at the image frequency can have stronger signal powers than the satnav signals.

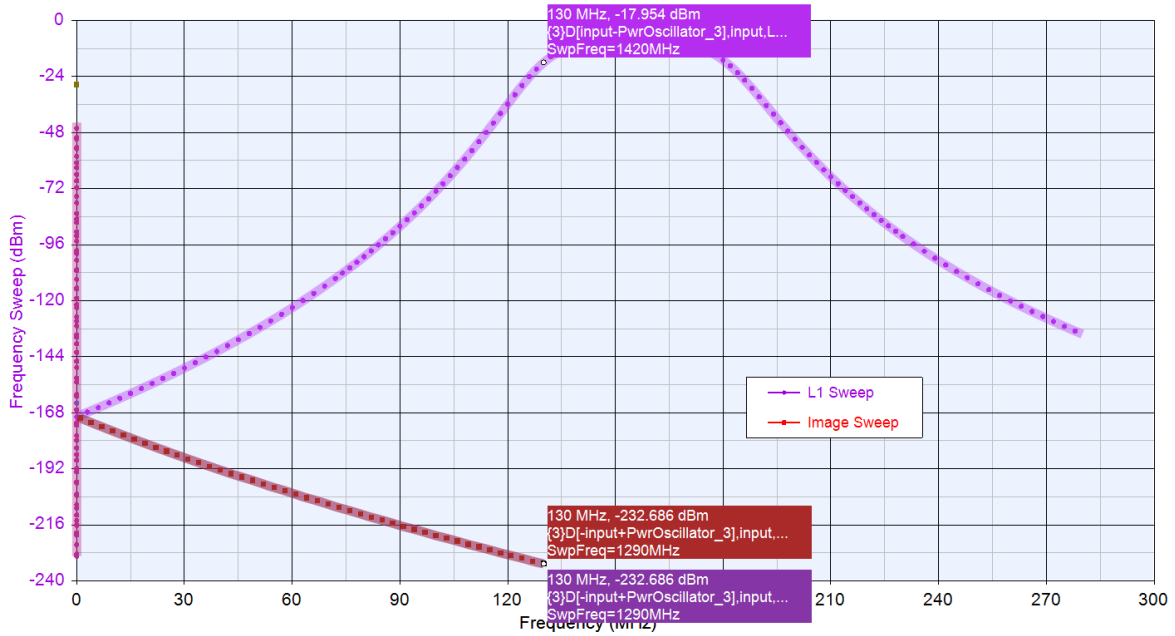


Figure 3.5.2: Five Resonator Ceramic RF Filter Image Rejection

The passband L1 signal is shown in light purple, the image frequency is shown in dark purple. There is over 214 dB of attenuation of the image frequency, far exceeding the minimum amount required. There is 18 dB of insertion loss, which will degrade the noise figure of the front-end.

Fewer resonators can give a better group delay response while still filtering the image frequency. Figure 3.5.3 displays the spectrum sweep using four resonators.

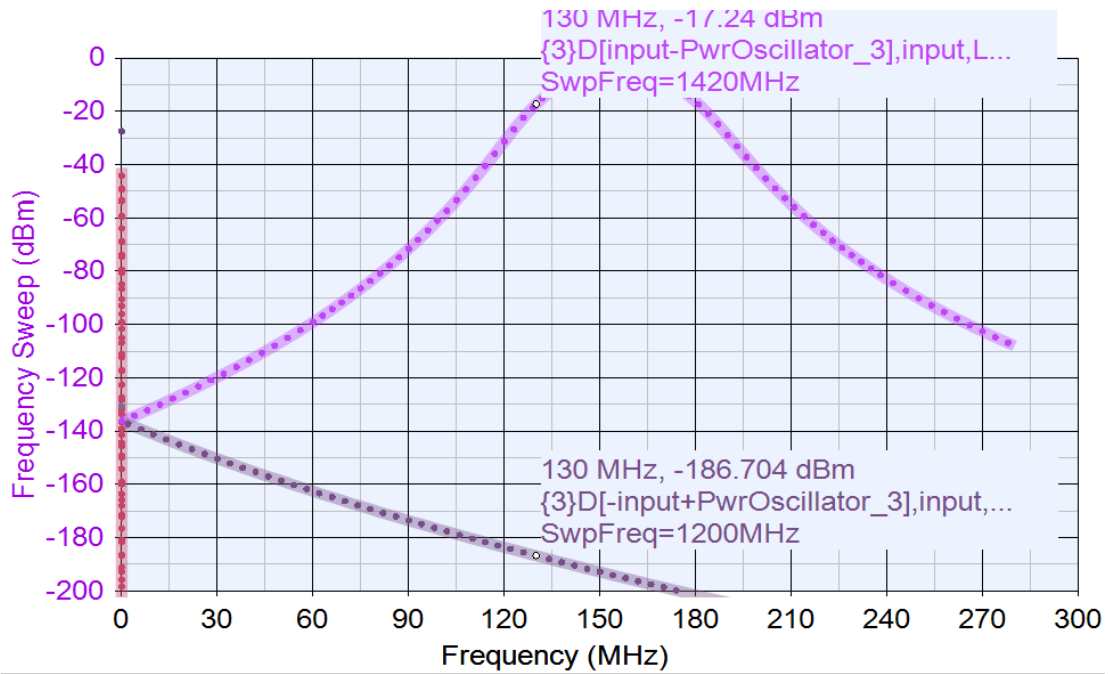


Figure 3.5.3: Four Resonator Ceramic RF Filter Image Rejection

The 4-resonator design offers 175 dB of attenuation at the image frequency. A signal path that utilizes a single filter with two resonators may offer adequate image rejection. Figure 3.5.4 shows the spectrum sweep results.

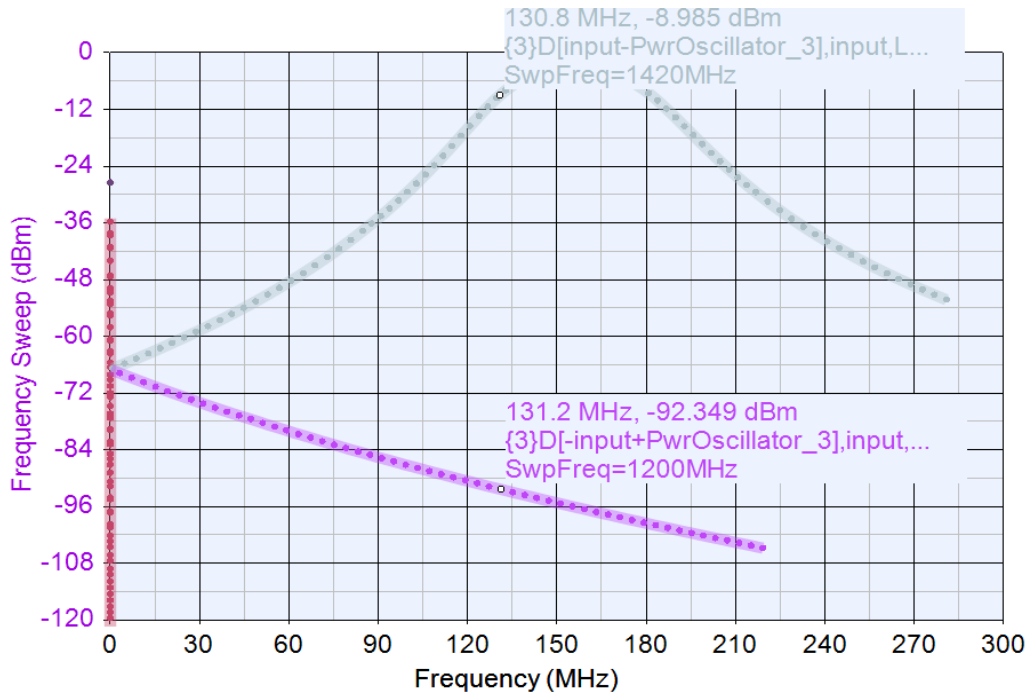


Figure 3.5.4: Four Resonator Ceramic RF Filter Image Rejection

A single 2-resonator filter offers 83.3 dB of attenuation to the image. In some scenarios or applications, this may be adequate. In applications where minimum group delay variations are required, such as satnav signal deformation monitoring, a single 2-resonator filter would suffice.

Figure 3.5.5 displays the group delay variations of all resonator combinations.

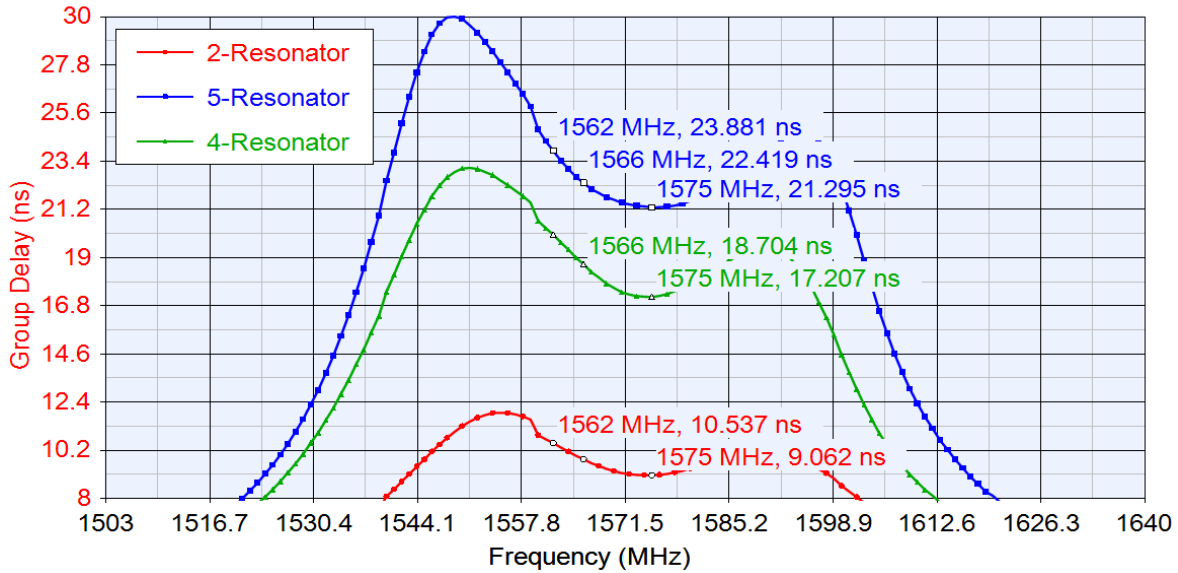


Figure 3.5.5: Group Delay of RF Bandpass Filters

The large group delay variations within the passband is undesirable. A flat group delay response in the center of the passband will add minimal signal deformations to the satnav signal. Large group delay variations at the edges of the filters are unavoidable in resonator filters. There is a minimum of 21.8 ns of delay at the center of the passband. If we desired 32 MHz of bandwidth for signal processing, the group delay variations will be 4 ns. The group delay variations are sparse for the single 2-resonator filter. Depending upon the amount of bandwidth needed for signal processing, the maximum group delay variations will be approximately 2 ns for larger bandwidths. In building the layout for the front-end the operator has the ability to choose to either use the two 2-resonator filters or one by flipping capacitors on the PCB.

3.6 Reference Oscillator

Choosing a RO with the lowest phase noise is a good way improve receiver tracking loops measurements. The stable RO allows for longer integration times and narrow tracking loop bandwidths. The output of the FSPLL is phase locked to the RO. The RO is essentially multiplied and divided in a closed loop to reach a desired frequency. Any frequency offset or drift of the RO will manifest itself in the FSPLL's frequency and will need to be tracked by the receiver's satnav signal carrier tracking loops. Crystal ROs used in satnav receivers typically have good short-term frequency stability but drift over the long term. OCXOs extends this short-term stability by minimizing temperature variations – making them more desirable for instrumentation satnav receivers which require long pre-detection integration times. A Wenzel 10 MHz triple oven OCXO was chosen as the reference oscillator [25]. Figure 3.6.1 displays the SSB phase noise of the device.

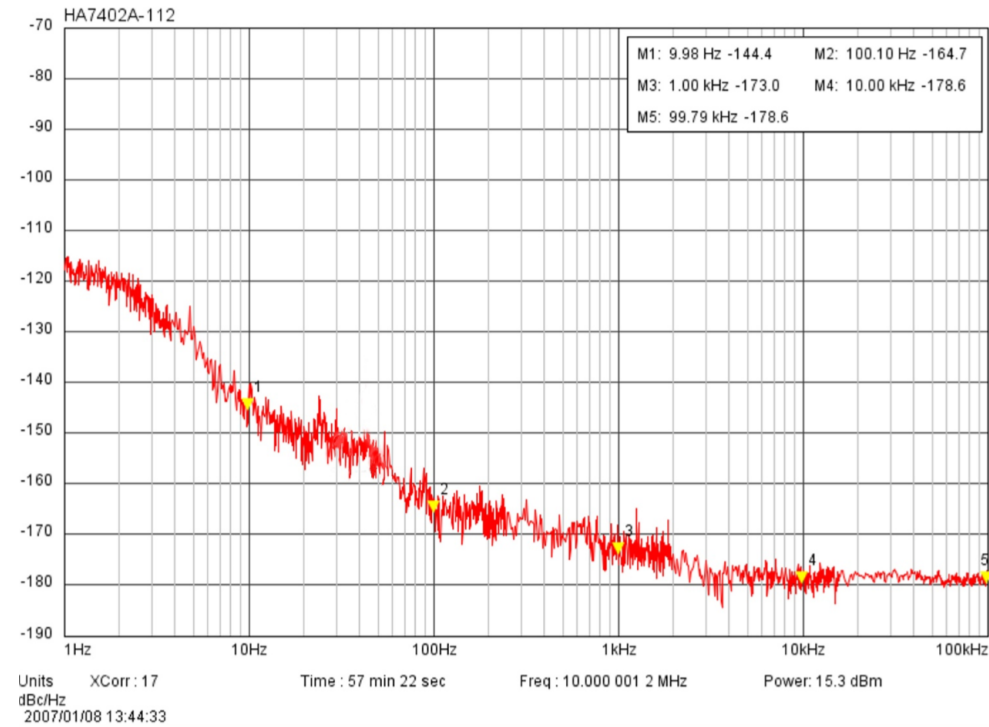


Figure 3.6.1: 10 MHz OCXO Reference Oscillator SSB Phase Noise

By multiplying the RO frequency of 10 MHz by 142, we are increasing the phase noise in Figure 3.6.1 by $10 \log_{10} 142$, or by 21.5 dB. Thus, the phase noise at M1 will be $-144.4 + 21.5 = -122.9$ dBc at 1420 MHz.

3.7 Frequency Synthesizer Phase Locked Loop

The FSPLL is responsible for synthesizing the LO frequency using the RO as the reference. Any phase noise on the FSPLL's LO will be added to the phase of all received satnav signals.

Spurs are considered to be 1-Hz bandwidth, and do not contribute much to the overall integrated phase noise. The degradation caused by the spurs in the receiver's tracking loops are difficult to quantify. The spurs can mix in out-of-band signals into the

IF passband, decreasing the SNR [12], [26]. Integer boundary spurs will occur at offsets at multiples of the PFD frequency [12]. This is due to the harmonics of the harmonics of the PFD and charge pumps. Spurs can be created through voltage supply pins by injecting spurious energy onto the ground and power rails causing crosstalk with the VCO and charge pump [12].

The FSPLL's lock time is of little concern in the given frequency plan, as only one LO frequency is required for a given RF front-end.

There are several major contributing features of a FSPLL that impact the phase noise and spur performance. The following attributes were derived for reducing phase noise and spurs for FSPLL's with integrated VCOs, charge pump, and PFD. The loop filter is the only external component. Several of industry's FSPLLs were configured and evaluated for their performance in a high-fidelity satnav receiver, their results are in Section 4.4.

3.7.1 Integer-N Feedback Divider and the PFD Operation Frequency

For best spur and phase noise performance, the PLL should be operated in Integer-N mode with a high PFD frequency. This limits the frequency step size of the FSPLL to integer divisions of the RO. This may be a problem in frequency plans which require fine frequency resolution of the LO. In which case Fractional-N may be more beneficial. Fractional-N mode dithers between N and N+1 divide ratios to achieve fractional division for finer frequency resolution on the output. However, the phase noise suffers, and spurs are created closer to the LO. The spur locations are also difficult to predict and account for in Fractional-N mode. Thus Integer-N division is preferred in FSPLLs for high-fidelity

satellite navigation and timing (satnav) receivers. Higher Integer-N divisions result in increased phase noise by $20 \log_{10} \frac{N}{M}$, M being the input divider [12].

3.7.2 The RO input divider/multiplier M

Avoid using the RO divider if possible because it is best to operate the PFD at a higher frequency, resulting in a lower N value. The ADF 4355-2, MAX 2871, and the LMX 2582 all have the option of a low noise reference frequency doubler. This is useful for lowering the Integer-N divider but can increase spur power.

3.7.3 Loop Filter's Bandwidth, Phase Margin, Order, and Pole Ratio

The loop filter, $H_{LF}(s)$, is the most important component for determining phase noise, stability, and spurs of the FSPLL. The loop filter is designed for a fixed value of N , I_p , and K_{VCO} . The bandwidth of the loop filter should be significantly smaller than the Nyquist criteria set by the PFD frequency. For best integrated phase noise performance, the FSPLL loop bandwidth is set to where the VCO phase noise intersects the PFD's [12], [26]. The phase margin controls the stability, lock time, and peaking of the phase noise filter shape. High phase margins are desired because lock time is of little concern, greatly reduces integrated phase noise, and increases loop stability. Higher-order filters may be desirable for filtering spurs and improving lock time. If spurs are well outside the bandwidth of the loop filter, second order filters will work best.

3.7.4 The Loop Gain

The loop gain is determined by the charge pump gain I_p and the VCO sensitivity K_{VCO} . The designer has little control over the VCO sensitivity and is usually retrieved

from the devices' data sheet or software tool provided by the manufacturer. The designer can control the charge pump gain, I_p . For best phase noise performance, a high I_p works best. However larger I_p results in larger loop filter passive components and spur power.

The loop gain is given by [12]:

$$K = \frac{I_p K_{VCO}}{N}. \quad (49)$$

The user can best improve phase noise between 0 Hz and 100 Hz by selecting a stable RO. The VCO performance is manufacture specific. Wideband FSPLL are equipped with multiple VCOs that are tuned to specific frequency ranges through switching capacitors internal to the device. It is best to let the device pick and calibrate its VCO based on the user defined frequency. The calibration is done during its initial pull in. The calibration time does not matter in our design case as the LO is a single predefined frequency.

3.7.5 PCB Layout and Power

The traces on the external loop filter should not be exposed to electromagnetic interference (EMI) from any RF, power, or digital signals present on the board. Any noise, or EMI on the loop filter will manifest itself as phase noise in the VCO output. Low ripple power supplies are essential for reducing spurious emissions. Ferrite beads should be used on the VCO, charge pump, and digital power supply lines of the device in order to minimize coupling. Grounded co-planar waveguide (GCPWG) RF traces should be used for the RO and LO out traces for maximum isolation. RF coupling onto the LO should be minimized. Class 1 temperature coefficient capacitors should be used in the loop filter,

such as capacitors with COG dielectric material. With large loop gains, it may be a challenge finding large COG capacitors [12], [26].

3.8 Gain Control and Linearity for the ADC

The received signal power of the GPS L1C is -127 dBm given an isotropic antenna. In a 50 MHz bandwidth receiver, the thermal noise power is -127 dBW, given through:

$$\sigma_{N_0}^2 = k_B T_0 B = (1.28 \times 10^{23})(295)(50 \times 10^6) = 1.88 \times 10^{-13} \text{ (W)}, \quad (50)$$

$$10 \times \log_{10} 1.88 \times 10^{-13} = -127 \text{ dBW} = -97 \text{ dBm}. \quad (51)$$

The GPS L1C code is 30 dB below the thermal noise power in a 50 MHz receiver. The goal of the receiver front-end is to amplify the noise floor, so it may be quantized by the ADC. Interference or jamming is considered to be broadband over the 50 MHz passband. If the receiver were to experience a 100 dB J/S environment, the thermal noise power will equivocally be -57 dBW or -27 dBm of power. The maximum power the front-end is designed for is -27 dBm. The front-end must amplify an input signal between -97 to -27 dBm to be quantized by the ADC. The AD9681 largest available input span is 2V peak-to-peak. Over a 50 Ω load this equates to a maximum signal power of 10 dBm. With an ENOB of 12, the ADC can quantize signals down to -62 dBm.

In the baseband signal processing of satnav signals, the correlators do not benefit much from having a large sample bit depth [5]. Having large bit depths can prove a hinderance in the correlation process due to computational resources required. With little or no interference present, 1, 2 or 3 bits of quantization will suffice. Therefore, the minimum amount of amplification needed is shown in Figure 3.8.1.

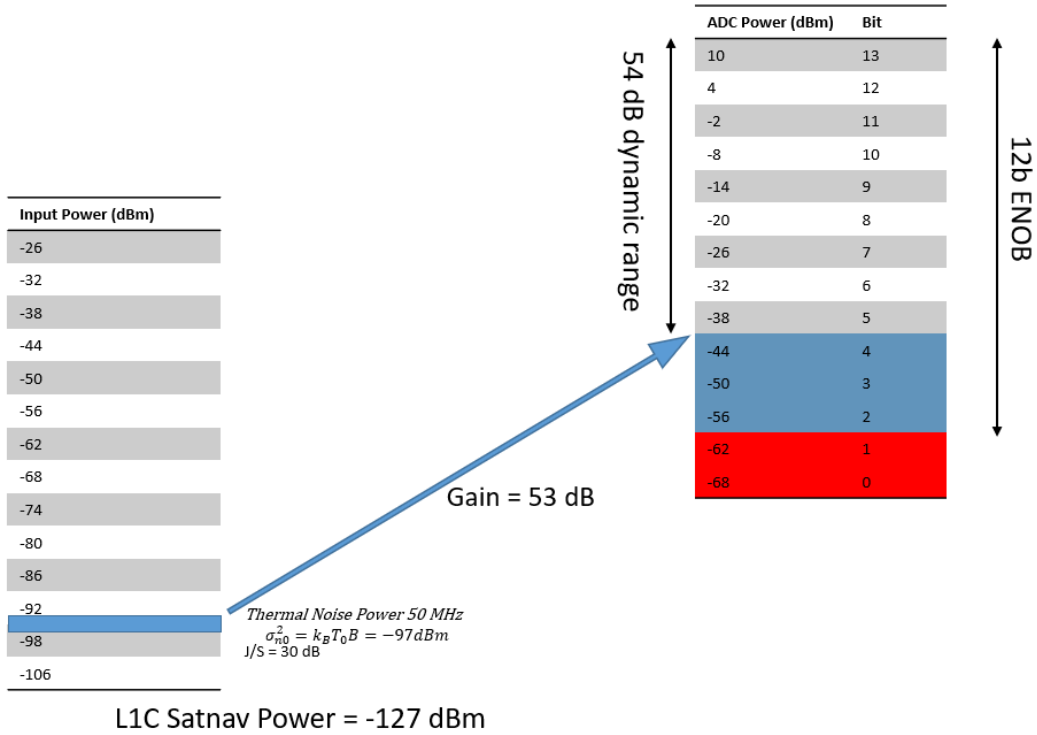


Figure 3.8.1: ADC Operation at -97 dBm Input Power

One added benefit of not amplifying the thermal noise power up the full scale of the ADC is that a receiver can quantize and analyze any interference that may present itself. When interference is present, there is 54 dB of dynamic range before attenuation is needed to keep the ADC operating within its range. Figure 3.8.2 shows the ADC operating at full scale.

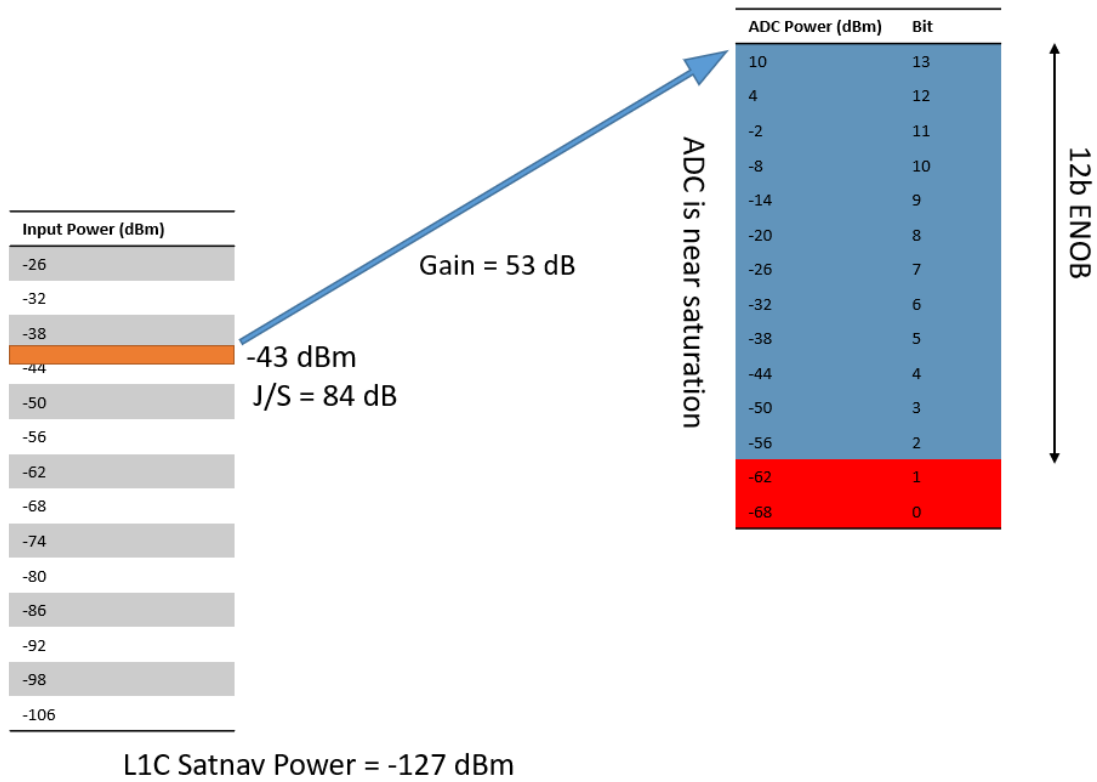


Figure 3.8.2: ADC Operation at -43 dBm Input Power

If any additional interference were to be added, attenuation will be needed to prevent the ADC and any amplifiers from saturating. To be able to handle a maximum input power of -27 dBm, the front-end need only supply 37 dB of gain.

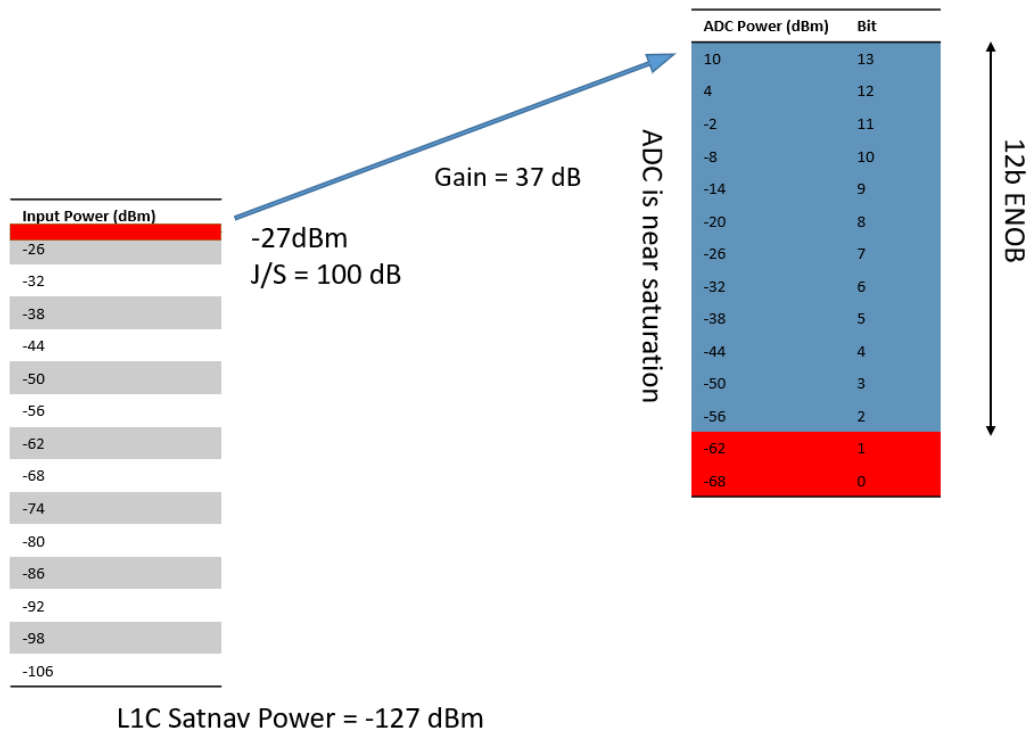


Figure 3.8.3: ADC Operation at Full Scale Input Power (-27 dBm)

Employing an automatic gain control (AGC) to adjust the level of amplification based upon on the number of bits being excited would work effectively in most satnav receivers. However, an instrumentation satnav receiver should be able to sense the amount of interference in the environment and be able to make accurate power interpretations of the amount of interference received. An AGC can dilute the precision of a power reading. Therefore, the receiver should be able to provide more than 53 dB of gain, and any additional gain control will be set by adjusting the attenuation of some variable digital attenuators (VDA). The VDA are also responsible for preventing the saturation of amplifiers in the signal path. The HMC542B [27] is an ideal candidate, the device offers 0.5 dB steps of attenuation all the way up to 31.5 dB. The device also has a frequency range of operation from DC to 4 GHz.

3.9 RMS Power Detector

An RMS power detector is useful for measuring the received signal power regardless of the modulation type. The received signal power is expected to be between -97 dBm and -27 dBm. The ADC can effectively quantize RF input signals up to -43 dBm before the attenuators need to be adjusted. The RMS power detector can provide greater insight into the true power received and can aid in adjusting the attenuation of the VDAs. The HMC1020 [28] has a 1 dB detection accuracy from DC to 3.9 GHz and an input dynamic range from -65 dBm to +7 dBm making it an ideal candidate for sensing the RF input power after the ADC is close to saturation. Figure 3.9.1 shows the position of the HMC1020 in the signal path.

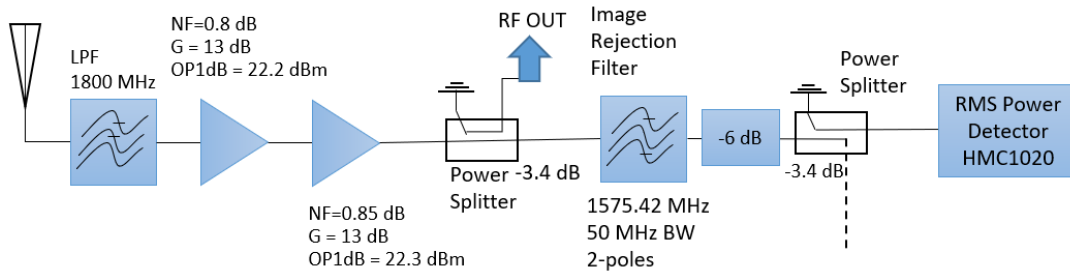


Figure 3.9.1: RMS Power Detector Signal Path

At minimum, the RMS power detector will receive -84 dBm, accounting for the losses in the power splitters and filters, well below its dynamic range. When the received signal power at the antenna is -43 dBm, the RMS power detector will receive -31 dBm, well within its dynamic range, and with the ability to sense an additional 38 dB of dynamic range. The HMC 1020 can effectively make power measurements well over the 100 dB J/S threshold the front-end is designed to handle.

3.10 Gain Control, Noise Figure and Linearity RF Calculator

The noise figure of the front-end is the amount of degradation of the SNR contributed by the antenna's temperature, transmission line loss, and LNAs. Transmission line length from the antenna to the first LNA should be minimized to keep a low noise figure. Depending on the cable quality, losses can incur from 25 dB/100ft to 1.3 dB/100ft. Antennas with integrated LNAs greatly improve the noise figure. Selecting the first couple amplifiers in the signal path sets the noise figure of the front-end. They need to be able to handle the -29 dBm input power while keeping linearity. The first two amplifiers in the signal chain were chosen to be the MAAL-010704 [29] and the TQP3M9005 [30] respectively. Cascaded, they contribute 26 dB of gain, and have a noise figure of 0.83 dB.

The fastest and simplest way to assess the performance of the signal path under certain RF input conditions is to build a spread sheet calculator that computes the RF power, noise figure, and linearity after each device in the signal path. By this method, one can see when amplifiers are operating near their saturation regions and configure the attenuators to preserve linearity. The voltage and current consumed by each device is also included. By knowing the power consumption of the front-end an appropriate voltage regulator can be selected. Table 3.10.1 shows the signal path under nominal conditions. The received signal power from a passive antenna is -97 dBm.

Table 3.10.1: Gain, Linearity and Noise Figure of Front-End with Passive Antenna -

97dBm

Component	Freq (MHz)	Description	Gain (dB)	NF (dB)	OIP1 (dbm)	OIP3 (dbm)	Current (A)	Volts (V)	Pwr (dbm)	Gain (dB)	NF (dB)	OIP1 (dbm)	OIP3 (dbm)	A	V	PWR (W)	RF Pwr > OIP1
1 Antenna			0	0	999	999	0	0	-97	0	0.0	999.0	999.0	0	0		GOOD
2 T-Line	1575.42		-0.1	0.1	999	999	0	0	-97.1	-0.1	0.1	995.9	999.0	0	0		GOOD
3 LFCN1800	1575.42	RF LPF	-0.62	0.62	999	999	0	0	-97.72	-0.72	0.7	993.8	999.0	0	0		GOOD
4 MAAL-010704	1575.42	LNA 1	13	0.8	22.2	36.2	0.08	5	-84.72	12.28	1.5	22.2	36.2	0.08	5	0.4	GOOD
5 TOP3M9005	1575.42	LNA 2	13	0.85	22.3	34	0.05	5	-71.72	25.28	1.6	22.1	33.9	0.13	5	0.65	GOOD
6 QCN-19	1575.42	Splitter	-3.4	3.4	999	999	0	0	-75.12	21.88	1.6	18.7	30.5	0.13	5	0.65	GOOD
7 2DF4	1575.42	RF BPF	-0.8	0.8	999	999	0	0	-75.92	21.08	1.6	17.9	29.7	0.13	5	0.65	GOOD
8 QCN-19	1575.42	Splitter	-3.4	3.4	999	999	0	0	-79.32	17.68	1.6	14.5	26.3	0.13	5	0.65	GOOD
9 EX8-24AT4AR3X	1575.42	Atten	-6	6	999	999	0	0	-85.32	11.68	1.8	8.5	20.3	0.13	5	0.65	GOOD
10 TOP369182	1575.42	Amp	21.7	3.9	15.1	28	0.045	5	-63.62	33.38	2.0	15.0	27.8	0.175	5	0.875	GOOD
11 HMC542BLP4E	1575.42	Var Atten	-1	1.5	999	999	0.0028	5	-64.62	32.38	2.0	14.0	26.8	0.1778	5	0.889	GOOD
12 AG203-63	1575.42	Amp	17.7	3.1	8	20	0.02	5	-46.92	50.08	2.0	8.0	20.0	0.1978	5	0.989	GOOD
13 2DF4	1575.42	RF BPF	-0.8	0.8	999	999	0	0	-47.72	49.28	2.0	7.2	19.2	0.1978	5	0.989	GOOD
14 LFS522		Mixer	-0.3	13	9	23	0.056	5	-48.02	48.98	2.0	4.8	17.5	0.2538	5	1.269	GOOD
15 LFCN630	156.25	IF LPF	-0.62	0.62	999	999	0	0	-48.64	48.36	2.0	4.2	16.8	0.2538	5	1.269	GOOD
16 TOP369182	156.25	Amp	22.8	3.9	16	30	0.045	5	-25.84	71.16	2.0	15.7	27.6	0.3016	5	1.494	GOOD
17 HMC542BLP4E	156.25	Var Atten	-2	1.5	999	999	0.0028	5	-27.84	69.16	2.0	13.7	27.6	0.3016	5	1.508	GOOD
18 AG203-63	156.25	Amp	17.7	2.9	8.2	20.3	0.02	5	-10.14	86.86	2.0	8.2	20.3	0.3216	5	1.608	GOOD
19 HMC589A	156.25	Amp	0	2.8	20	37	0.088	5	-10.14	86.86	2.0	7.9	20.2	0.4096	5	2.048	GOOD
20 EX8-24AT3AR3X	156.25	Atten	-4	4	999	999	0	0	-14.14	82.86	2.0	3.9	16.2	0.4096	5	2.048	GOOD
21 IF FILT	156.25	IF BPF	-2	2	999	999	0	0	-16.14	80.86	2.0	1.9	14.2	0.4096	5	2.048	GOOD
22 EX8-24AT3AR3X	156.25	Atten	-4	4	999	999	0	0	-20.14	76.86	2.0	-2.1	10.2	0.4976	5	2.488	GOOD
23 HMC589A	156.25	Amp	0	4	19	35	0.088	5	-20.14	76.86	2.0	-2.1	10.2	0.4976	5	2.488	GOOD
24 EX8-24AT3AR3X	156.25	Atten	0	0	999	999	0	0	-20.14	76.86	2.0	-2.1	10.2	0.4976	5	2.488	GOOD

Some additional attenuation is needed to provide the ADC with -46 dBm of power. To preserve the noise figure, attenuation is best performed in the latter stages of the signal path. Thus, the first attenuator, Device #11, is set to -2 dB, and the latter attenuator, Device #17, to -23 dB. The RF power at the end of the signal path is -46.14 dBm. If more bits are desired, the attenuation can be decreased on Device #17 to increase the signal power to the ADC. If the variable attenuators were to not add attenuation to the signal path, the ADC will receive -20 dBm of power. The ADC's bits 8 through 0 will be activated with -20 dBm of power. During assembly, Device #19 can be activated to provide an additional 20 dB of gain. The additional sampling dynamic range may be useful in certain applications. Total noise figure of the front-end is 2.03 dB, most of the contributions are from the transmission line, the first LNAs, and the RF image rejection filter. Once the noise figure is set by the first couple components it does not change much along the signal path.

When the signal input power is -57 dBm, Device #18 is the first amplifier to saturate. The second digital attenuator must be adjusted to prevent this. The RF signal power at the ADC is -1.14 dBm. At a signal input power of -54 dBm, Device #16 begins to saturate. The first digital attenuator must be adjusted to prevent Device #16 from saturating. As input power is increased from -54 dBm to -27dBm, the attenuation of the first digital attenuator must also increase.

Under the conditions of receiving -43 dBm with a passive antenna is shown in Table 3.10.2. If the attenuators were not adjusted, Device #s 16, 18, and 19 will pass their OIP1 saturation point. Thus, the attenuators need to be tweaked to keep the amplifiers operating in their linear region. Device #16 is before the second attenuator; thus, it is the

first attenuator's responsibility to keep Device #16 in the linear region. The second attenuator will keep Device #s 18 and 19 linear.

Table 3.10.2: Gain, Linearity and Noise Figure of Front-End -46 dBm Input

Component	Freq (MHz)	Description	Gain (dB)	NF (dB)	OP1 (dbm)	OP3 (dbm)	Current (A)	Volts (V)	Pwr (dbm)	Gain (dB)	NF (dB)	OP1 (dbm)	OP3 (dbm)	A	V PWR (W)	RF Pwr > OP1
1 Antenna			0	0	999	999	0	0	-46	0	0.0	999.0	999.0	0	0	GOOD
2 T-Line	1575.42		-0.1	0.1	999	999	0	0	-46.1	-0.1	0.1	995.9	999.0	0	0	GOOD
3 LFCN1800	1575.42	RF LPF	-0.62	0.62	999	999	0	0	-46.72	-0.72	0.7	993.8	999.0	0	0	GOOD
4 MAAL-010704	1575.42	LNA 1	13	0.8	22.2	36.2	0.08	5	-33.72	12.28	1.5	22.2	36.2	0.08	5	0.4 GOOD
5 TOP3M9005	1575.42	LNA 2	13	0.85	22.3	34	0.05	5	-20.72	25.28	1.6	22.1	33.9	0.13	5	0.65 GOOD
6 QCN-19	1575.42	Splitter	-3.4	3.4	999	999	0	0	-24.12	21.88	1.6	18.7	30.5	0.13	5	0.65 GOOD
7 2DF4	1575.42	RF BPF	-0.8	0.8	999	999	0	0	-24.92	21.08	1.6	17.9	29.7	0.13	5	0.65 GOOD
8 QCN-19	1575.42	Splitter	-3.4	3.4	999	999	0	0	-28.32	17.68	1.6	14.5	26.3	0.13	5	0.65 GOOD
9 EXB-24A13AR3X	1575.42	Atten	-6	6	999	999	0	0	-34.32	11.68	1.8	8.5	20.3	0.13	5	0.65 GOOD
10 TOP369182	1575.42	Amp	21.7	3.9	15.1	28	0.045	5	-12.62	33.38	2.0	15.0	27.8	0.175	5	0.875 GOOD
11 HMC542BLP4E	1575.42	Var Atten	-12	1.5	999	999	0.0028	5	-24.62	21.38	2.0	3.0	15.8	0.1778	5	0.889 GOOD
12 AG203-63	1575.42	Amp	17.7	3.1	8	20	0.02	5	-6.92	39.08	2.1	7.8	19.8	0.1978	5	0.989 GOOD
13 2DF4	1575.42	RF BPF	-0.8	0.8	999	999	0	0	-7.72	38.28	2.1	7.0	19.0	0.1978	5	0.989 GOOD
14 LT5522		Mixer	-0.3	13	9	23	0.056	5	-8.02	37.98	2.1	4.7	17.3	0.2538	5	1.269 GOOD
15 LFCN630	156.25	IF LPF	-0.62	0.62	999	999	0	0	-8.64	37.36	2.1	4.1	16.7	0.2538	5	1.269 GOOD
16 TOP369182	156.25	Amp	22.8	3.9	16	30	0.045	5	14.16	60.16	2.1	15.7	29.5	0.2988	5	1.494 GOOD
17 HMC542BLP4E	156.25	Var Atten	-25	1.5	999	999	0.0028	5	-10.84	35.16	2.1	-9.3	4.5	0.3016	5	1.508 GOOD
18 AG203-63	156.25	Amp	17.7	2.9	8.2	20.3	0.02	5	6.86	52.86	2.1	5.3	18.2	0.3216	5	1.608 GOOD
19 HMC589A	156.25	Amp	0	2.8	20	37	0.088	5	6.86	52.86	2.1	5.1	18.1	0.4096	5	2.048 GOOD
20 EXB-24A13AR3X	156.25	Atten	-4	4	999	999	0	0	2.86	48.86	2.1	1.1	14.1	0.4096	5	2.048 GOOD
21 IF FILT	156.25	IF BPF	-2	2	999	999	0	0	0.86	46.86	2.1	-0.9	12.1	0.4096	5	2.048 GOOD
22 EXB-24A13AR3X	156.25	Atten	-4	4	999	999	0	0	-3.14	42.86	2.1	-4.9	8.1	0.4096	5	2.048 GOOD
23 HMC589A	156.25	Amp	0	4	19	35	0.088	5	-3.14	42.86	2.1	-4.9	8.1	0.4976	5	2.488 GOOD
24 EXB-24A13AR3X	156.25	Atten	0	0	999	999	0	0	-3.14	42.86	2.1	-4.9	8.1	0.4976	5	2.488 GOOD

The ADC will receive -3.14 dBm of power, due to the losses incurred from the IF filter and the 4 dB attenuators on either side of the filter that are used for improving matching. The noise figure here is slightly worse at 2.08 dB, of course this due to the additional attenuation needed in the RF portion of the signal chain.

The maximum designed power the front can receive is -27 dBm with a passive antenna. The received signal power of an L1C signal is now 100 dB below the interference power. Table 3.10.3 shows the total signal gain and noise figure of the signal path.

Table 3.10.3: Linearity, Gain and Noise Figure of Front-End at Full Scale -26dBm

Component	Freq (MHz)	Description	Gain (dB)	NF (dB)	OP1 (dbm)	OIP3 (dbm)	Current (A)	Volts (V)	Pwr (dbm)	Gain (dB)	NF (dB)	OIP1 (dbm)	OIP3 (dbm)	A	V	PWR (W)	RF Pwr > OIP1
1 Antenna			0	0	999	999	0	0	-26	0	0.0	999.0	999.0	0	0		GOOD
2 T-Line	1575.42		-0.1	0.1	999	999	0	0	-26.1	-0.1	0.1	995.9	999.0	0	0		GOOD
3 LFCN1800	1575.42	RF LPF	-0.62	0.62	999	999	0	0	-26.72	-0.72	0.7	993.8	999.0	0	0		GOOD
4 MAAL-010704	1575.42	LNA 1	13	0.8	22.2	36.2	0.08	5	-13.72	12.28	1.5	22.2	36.2	0.08	5	0.4	GOOD
5 TQP3M9005	1575.42	LNA 2	13	0.85	22.3	34	0.05	5	-0.72	25.28	1.6	22.1	33.9	0.13	5	0.65	GOOD
6 QCN-19	1575.42	Splitter	-3.4	3.4	999	999	0	0	-4.12	21.88	1.6	18.7	30.5	0.13	5	0.65	GOOD
7 2DF4	1575.42	RF BPF	-0.8	0.8	999	999	0	0	-4.92	21.08	1.6	17.9	29.7	0.13	5	0.65	GOOD
8 QCN-19	1575.42	Splitter	-3.4	3.4	999	999	0	0	-8.32	17.68	1.6	14.5	26.3	0.13	5	0.65	GOOD
9 EXB-24AT4AR3X	1575.42	Atten	-25	25	999	999	0	0	-33.32	-7.32	8.3	-10.5	1.3	0.13	5	0.65	GOOD
10 TQP369182	1575.42	Amp	21.7	3.9	15.1	28	0.045	5	-11.62	14.38	11.7	9.7	21.8	0.175	5	0.875	GOOD
11 HMC542BLPAE	1575.42	Var Atten	-12	1.5	999	999	0.0028	5	-23.62	2.38	11.7	-2.3	9.8	0.1778	5	0.889	GOOD
12 AG203-63	1575.42	Amp	17.7	3.1	8	20	0.02	5	-5.92	20.08	11.8	7.3	19.3	0.1978	5	0.989	GOOD
13 2DF4	1575.42	RF BPF	-0.8	0.8	999	999	0	0	-6.72	19.28	11.8	6.5	18.5	0.1978	5	0.989	GOOD
14 LT5522		Mixer	-0.3	1.3	9	23	0.056	5	-7.02	18.98	11.9	4.4	16.9	0.2538	5	1.269	GOOD
15 LFCN630	156.25	IF LPF	-0.62	0.62	999	999	0	0	-7.64	18.36	11.9	3.7	16.3	0.2538	5	1.269	GOOD
16 TQP369182	156.25	Amp	22.8	3.9	16	30	0.045	5	15.16	41.16	11.9	15.6	29.5	0.2988	5	1.494	GOOD
17 HMC542BLPAE	156.25	Var Atten	-25	1.5	999	999	0.0028	5	-9.84	16.16	11.9	-9.4	4.5	0.3016	5	1.508	GOOD
18 AG203-63	156.25	Amp	17.7	2.9	8.2	20.3	0.02	5	7.86	33.86	11.9	5.3	18.1	0.3216	5	1.608	GOOD
19 HMC589A	156.25	Amp	0	2.8	20	37	0.088	5	7.86	33.86	11.9	5.1	18.1	0.4096	5	2.048	GOOD
20 EXB-24AT3AR3X	156.25	Atten	-4	4	999	999	0	0	3.86	29.86	11.9	1.1	14.1	0.4096	5	2.048	GOOD
21 IF FilT	156.25	IF BPF	-2	2	999	999	0	0	1.86	27.86	11.9	-0.9	12.1	0.4096	5	2.048	GOOD
22 EXB-24AT3AR3X	156.25	Atten	-4	4	999	999	0	0	-2.14	23.86	11.9	-4.9	8.1	0.4096	5	2.048	GOOD
23 HMC589A	156.25	Amp	0	4	19	35	0.088	5	-2.14	23.86	11.9	-4.9	8.1	0.4976	5	2.488	GOOD
24 EXB-24AT3AR3X	156.25	Atten	0	0	999	999	0	0	-2.14	23.86	11.9	-4.9	8.1	0.4976	5	2.488	GOOD

3.11 Nonlinear Simulation of Front-End

Keysight Genesys 2018 offers an alternative method for simulating the signal chain. Component vendors typically offer Touchstone files to designers [31]. The Touchstone files ‘.s2p’ provide the scattering parameters of the device which can be used in linear simulations. A linear simulation is helpful for understanding the gain and phase relationships in the design. The component vendors also provide OIP3, OIP1, and OIPSAT points which clarify the nonlinearities of the devices. Genesys can provide linear and nonlinear simulations of the devices to gain a better insight into the behavior of the signal chain. Figure 3.11.1 shows the signal path of Genesys simulations. All passive components are modeled with the s-parameters. All active components are modeled with their OIP3, OIP1, and OIPSAT. The IF filter that was designed with VPS is inserted into the design as well as the two 2-resonator RF image rejection filters. The same signal path that was used in the simple RF calculator is used here.

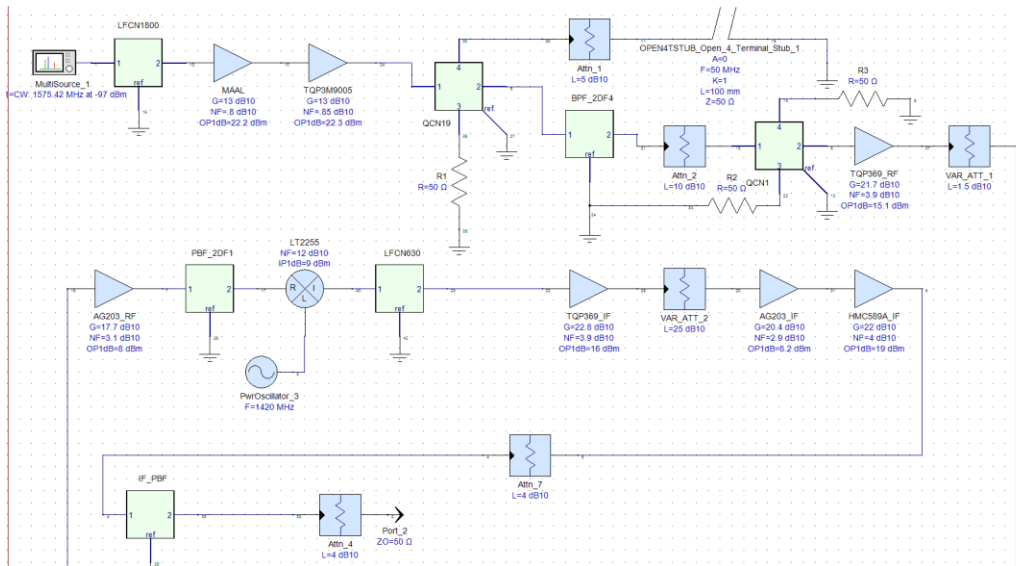


Figure 3.11.1: Genesys Nonlinear Signal Path Simulation

Considering the first scenario that was calculated with the -97 dBm input power from Table 3.10.1; the first attenuator was set to -2 dB and the second to -25 dB. By running a power compression curve, insight into the linearity of the front-end is achieved. The RF input power is swept from -97 dBm to -27 dBm. Figure 3.11.2 shows the gain at the output vs the input.

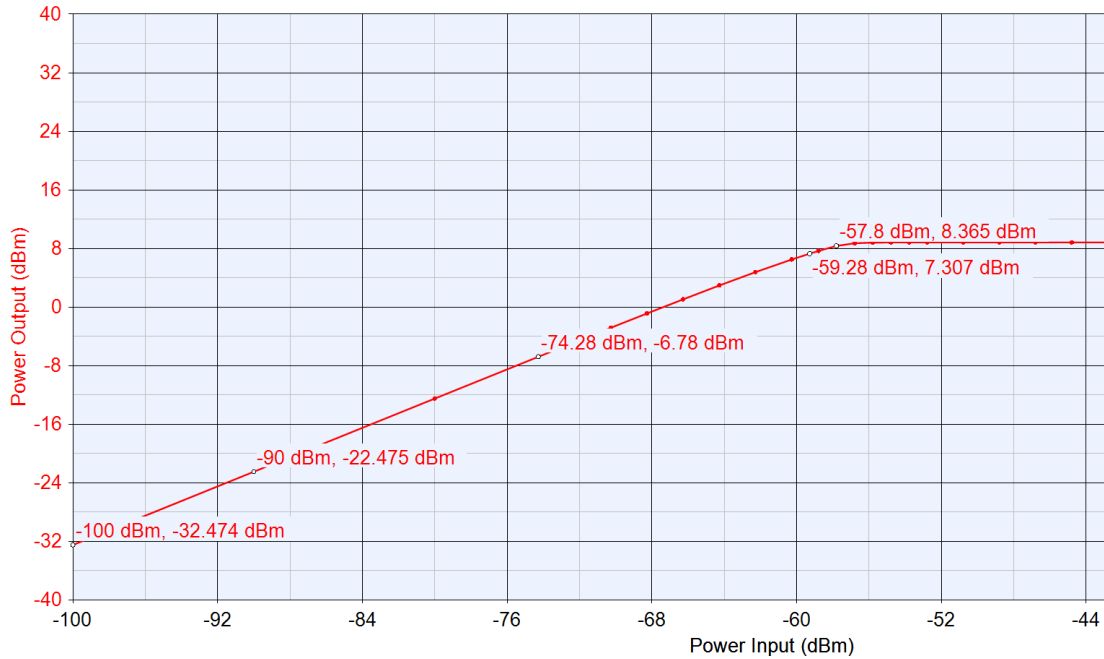


Figure 3.11.2: Gain and Linearity at -97 dBm Operation

As shown by the calculator, the front-end begins to saturate right before -57 dBm input. The digital attenuators must be adjusted to keep linearity. Under the full duress of -27 dBm input power, the attenuators are adjusted to that is displayed in Table 3.10.3. The gain and linearity sweep is shown in Figure 3.11.3.

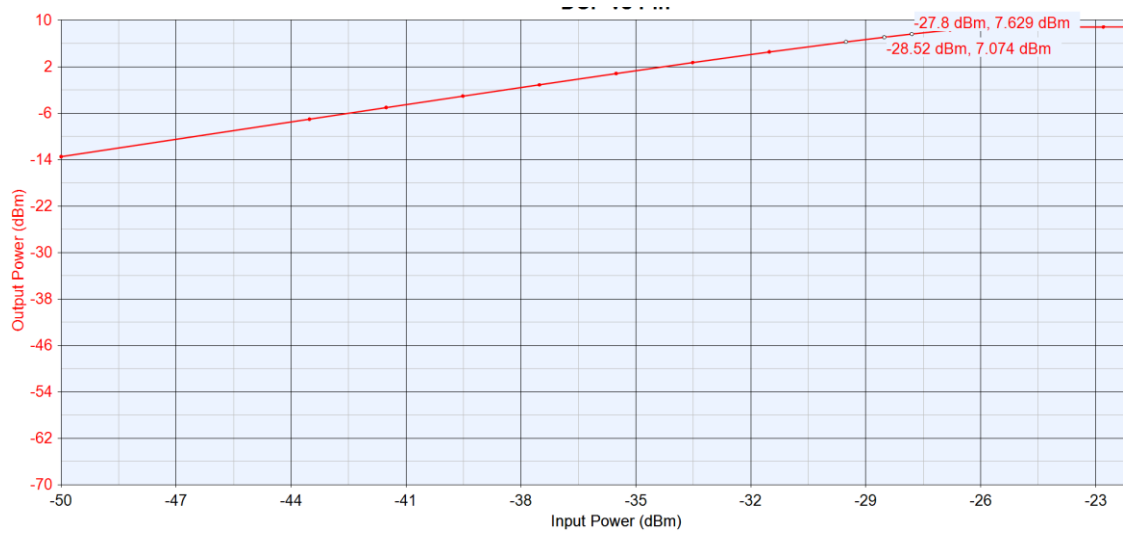


Figure 3.11.3: Gain and Linearity at -26 dBm Operation

The output power just begins to go nonlinear after the -27 dBm input power. Therefore, the system requirements of sustaining linearity in the signal chain for 100 dB J/S has been achieved.

IV. Analysis and Results

4.1 Introduction

This chapter attempts to validate the design methodologies and show performance of the front-end. Specialized RF components were evaluated and constructed for a high-fidelity satnav receiver.

Waveguides were constructed and evaluated on a chosen PCB stack-up. Insertion loss and reflections were evaluated over the satnav frequencies of operation. The first LNA in the antenna electronics or the front-end is essential for determining the noise figure and sensitivity. Careful evaluation of a high performing LNA was evaluated for its linearity, gain, and power consumption. The LO in the frequency plan is essential for determining the sensitivity of carrier phase measurements. Careful evaluation of several industry leading FSPLLs with integrated charge pumps and VCOs was conducted for use in a satnav receiver.

The front-end was then assembled and portions tested for performance. Simulated and live-sky signals were then injected into the front-end. Data was sampled, recorded and evaluated in a software defined receiver. The front-end's LO was compared against a proven FSPLL that has been used in satnav instrumentation receivers. The front-end's tracking performance was also compared against an industry leading manufacture of satnav reference receivers.

4.2 Waveguide Evaluation

The CPWG was chosen for its wideband matching and isolation. To find the best trace width and conductor spacing, an evaluation board was designed with different trace dimensions. The board was built with a Rogers 4003C controlled dielectric material, 8 mils thick [32]. High performance Amphenol end-launch SMA connectors were used for interfacing to the board. Advanced Circuits was used for the PCB fabrication [33]. Figure 4.2.1 displays the constructed CPWG under isolation testing.



Figure 4.2.1: CPWG Evaluation Board

Measurements were made with a Copper Mountain Planar 304/1 3.2 GHz Vector Network Analyzer (VNA) [34]. Figure 4.2.2 shows the reflected wave magnitude for the evaluated dimensions of the CPWG.

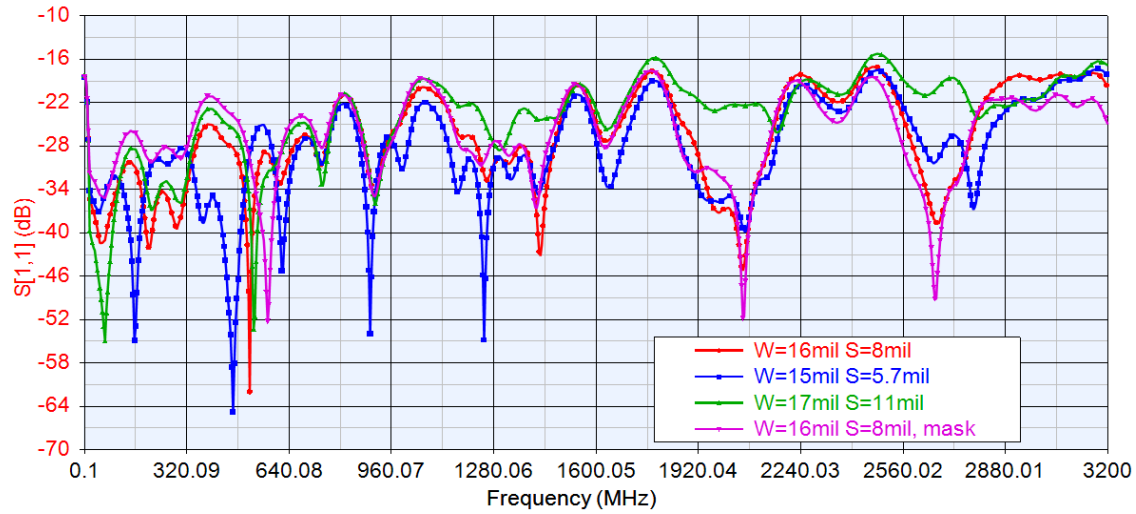


Figure 4.2.2: CPWG S11 for Difference Dimensions

From Figure 4.2.2, W is referring to the width of the conductor, and S is referring to the space between the conductor and ground plane.

Isolation is important to evaluate to eliminate mutual coupling in the layout. Figure 4.2.3 shows the isolation achieved at different distances from a CPWG covered in solder mask.

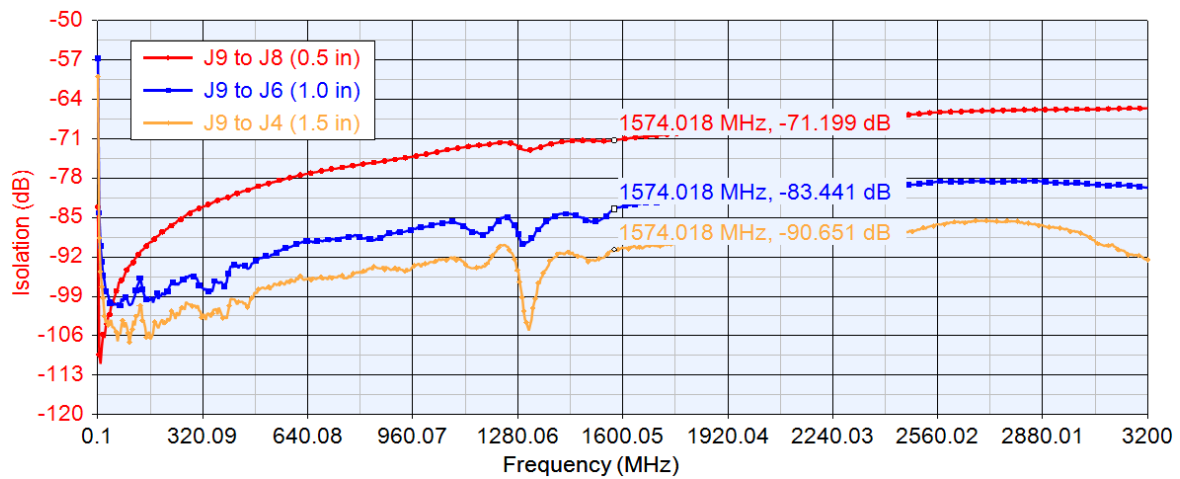


Figure 4.2.3: CPWG Isolation

Half an inch of separation gives 71 dB isolation, one inch gives 83.4 dB, and one and half inch gives 90 dB of isolation. Mutually coupling will be greatest when traces are parallel on the PCB.

4.3 Front-End Low Noise Amplifier Evaluation

The first LNA in the signal chain is imperative for the sensitivity of the overall front-end. The MACOM MAAL-010704 LNA [29] was chosen to be the first LNA due to its wideband matching, low noise figure, and high gain and linearity over the L-band. The amplifier's circuit was constructed on the same RO4003C material and stack up as the CPWG. The MACOM evaluation board was also purchased as a reference for design and performance. Figure 4.3.1 shows the MACOM evaluation PCB on the left, and the constructed PCB on the right.

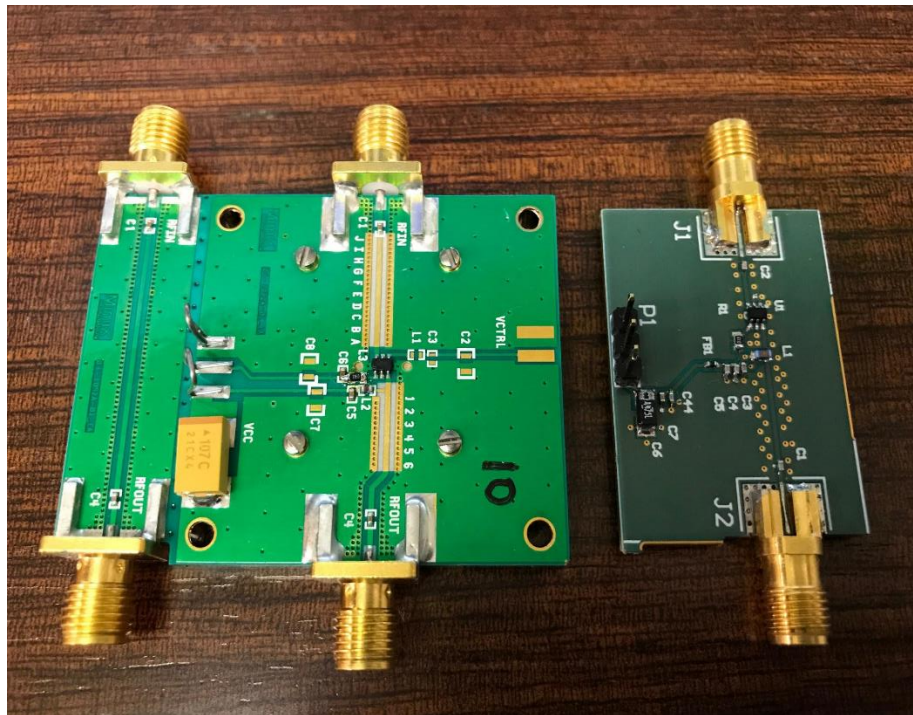


Figure 4.3.1: Left: MACOM Evaluation Board, Right: Constructed Evaluation Board

The designer has the ability to apply a voltage bias to a pin on the LNA that controls the gain and power consumption of the board. Gain and linearity is favorable, if the max current draw isn't being exceeded. Different resistors were evaluated for their performance. The Planar 403/1 VNA was used for collecting measurement data. Figure 4.3.2 shows gain of the device as a function of input power. The device begins to saturate as the gain begins to tail off under higher input power.

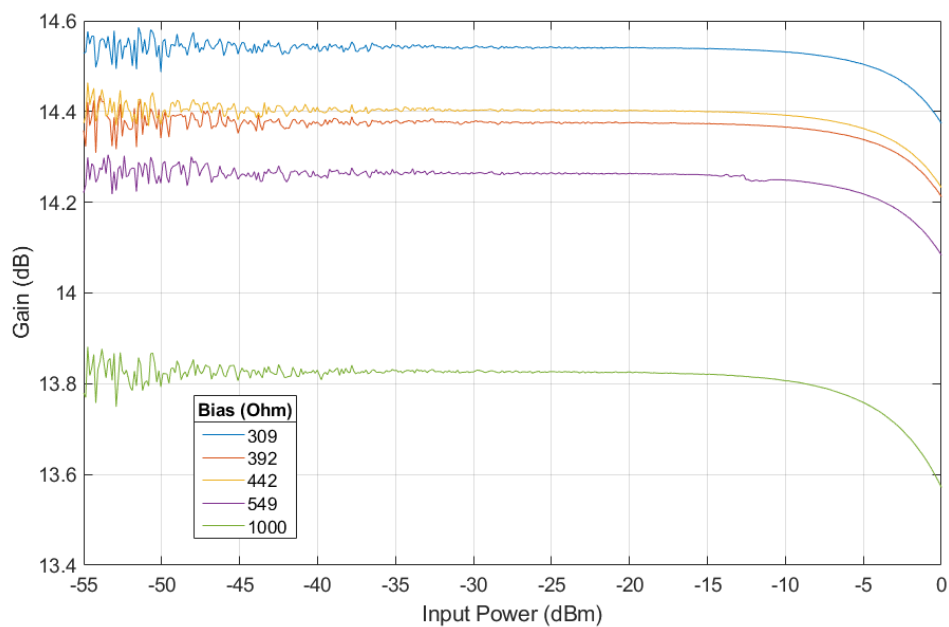


Figure 4.3.2: MAL-010704 LNA Gain and Linearity vs. Bias

The current consumption under each test was recorded in Table 4.3.1. This aids in calculating the power consumption of the entire front-end.

Table 4.3.1: MAL-010704 LNA Current Consumption

Bias Resistor (Ω)	Current Consumption (mA)
309	81
392	72
442	67
549	59
1000	38

Matching of the amplifier is shown Figure 4.3.3. The amplifier is well matched over the span of the L-band. This eliminates the need for requiring external matching components that contribute their own losses to the signal.

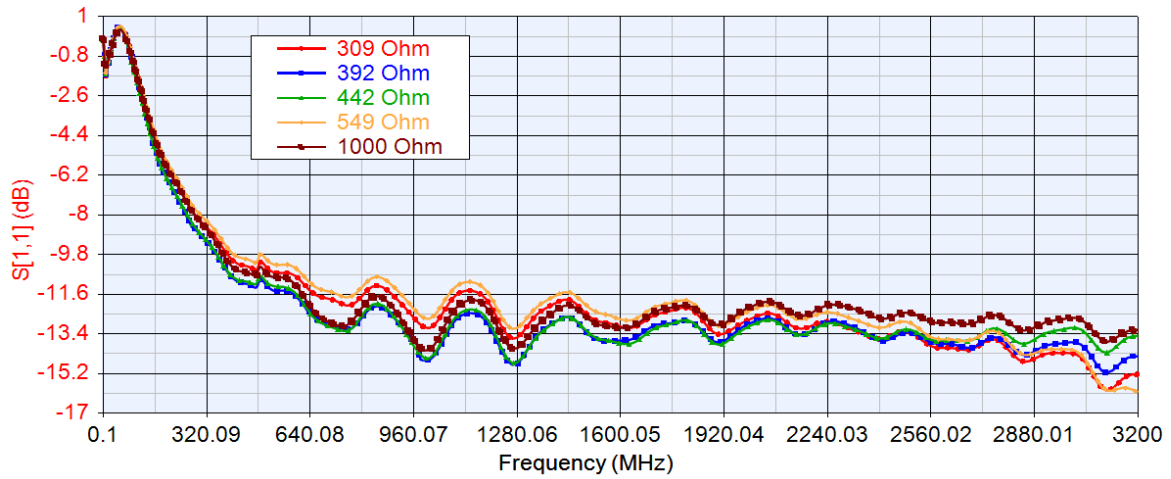


Figure 4.3.3: S11 of MAL-010704 LNA

The 309 Ω bias resistor was chosen for operation due to its higher gain and linearity over the other bias resistors.

4.4 Frequency Synthesizer Evaluation

Several PLLs with integrated charge-pumps and VCOs were evaluated for their performance as a LO in the frequency plan. A single-ended 10 MHz triple OCXO is used to supply the RO to all device evaluation boards. Some boards contained their own linear

power regulation circuitry. Power to all boards was supplied through a BK Precision 9130 power supply [35]. All devices are operated in Integer-N mode and only used to generate a single LO at 1420 MHz. All devices' loop filter bandwidths were configured for where the free running VCO's phase noise crosses the PFD's noise floor. All loop filters are 2nd order RC low pass filters shown in Figure 4.4.1. All loop filters used 0402 or 0603 package X7R capacitors due to footprint constraints on the evaluation boards.

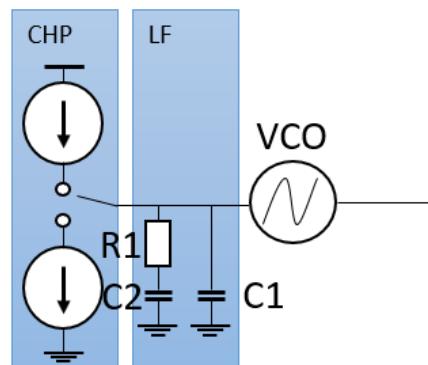


Figure 4.4.1: Charge Pump, Loop Filter components and VCO Circuit

4.4.1 Texas Instruments LMX 258

Figure 4.4.2 shows the LMX 2582 evaluation board from Texas Instruments [15]. The TCXO oscillator on the evaluation board was disabled. Power is supplied directly to the chip by the BK Precision 9130 power supply [35].

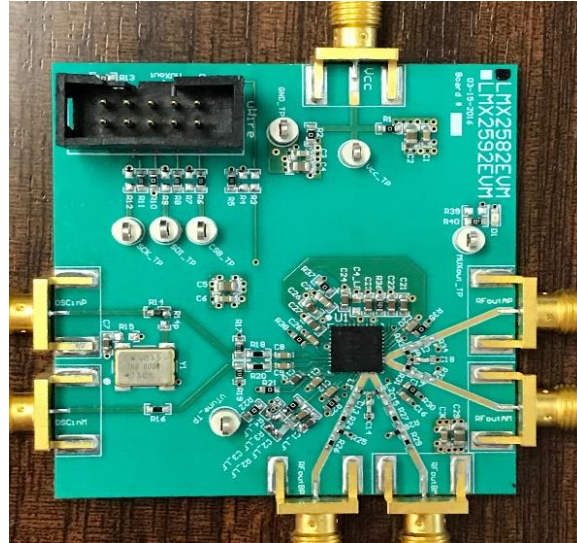


Figure 4.4.2: LMX 2582 Evaluation Board from Texas Instruments

The RO doubler and different pre-scalars were evaluated for spur and phase noise. Two loop configurations of varying gain were evaluated for their performance. The device's charge pump contains a gain multiplier that is capable of higher charge pump currents. Out of all devices evaluated, the charge pump multiplier is unique only to this device. The frequency of the VCO is divided by 4 using the output divider on the device to reach 1420 MHz. Table 4.4.1 displays the different configurations that were evaluated.

Table 4.4.1: LMX 2582 Configurations

#	I_p	K_{VCO}	f_{VCO}	N	M	BW	Phase margin	PFD	Pre-scalar
1	9.375 mA	40 MHz/V	5680 MHz	284	0.5	70 kHz	75 deg	20 MHz	2
2	24.22 mA	40 MHz/V	5680 MHz	71	0.5	70 kHz	75 deg	20 MHz	4
3	9.375 mA	40 MHz/V	5680 MHz	142	1	70 kHz	75 deg	10 MHz	2
4	9.375 mA	40 MHz/V	5680 MHz	142	1	70 kHz	75 deg	10 MHz	4
5	9.375 mA	40 MHz/V	5690 MHz	71	0.5	70 kHz	75 deg	20 MHz	4

4.4.2 Analog Devices ADF 4355-2

Figure 4.4.3 displays the ADF 4355-2 evaluation board by Analog Devices [36].



Figure 4.4.3: ADF 4355-2 Evaluation Board from Analog Devices

Different charge pump bleed currents were evaluated for phase noise and spurs. Out of the 4 devices evaluated, the ability to adjust the bleed current manually was unique to this device. The VCO's frequency of 5680 MHz is divided by 4 to reach 1420 MHz. Different pre-scalars on the device were also compared as displayed in Table 4.4.2.

Table 4.4.2: ADF 4355-2 Configurations

#	I_p	K_{VCO}	f_{VCO}	N	M	BW	Phase margin	PFD	Pre-scalar	I_{bleed}
1	4.8mA	20 MHz/V	5680 MHz	284	0.5	70 kHz	75 deg	20 MHz	4/9	67.5 uA
2	4.8mA	20 MHz/V	5680 MHz	284	0.5	70 kHz	75 deg	20 MHz	8/9	67.5 uA
3	4.8mA	20 MHz/V	5680 MHz	284	0.5	70 kHz	75 deg	20 MHz	4/9	82.5 uA
4	4.8mA	20 MHz/V	5680 MHz	284	0.5	70 kHz	75 deg	20 MHz	4/9	165 uA

4.4.3 Maxim Integrated MAX 2871

Figure 4.4.4 displays the MAX 2871 evaluation board by Maxim Integrated [37].

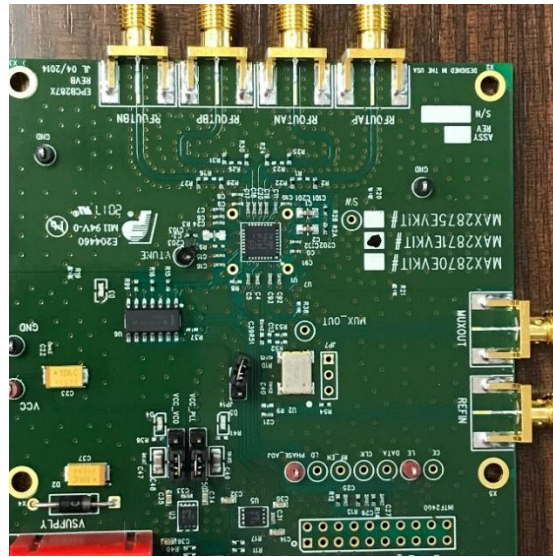


Figure 4.4.4: MAX 2871 Evaluation Board from Maxim Integrated

Utilizing a MUX, the VCO frequency or the RF out was selected to be divided by N before the PFD. The RF out signal is the 1420 MHz signal, contrived from the VCO being divided by 4. Table 4.4.3 shows the configurations.

Table 4.4.3: MAX 2871 Configurations

#	I_p	K_{VCO}	f_{VCO}	N	M	BW	Phase margin	PFD	Divider Input
1	3.2 mA	100 MHz/V	5680 MHz	284	0.5	70 kHz	75 deg	20 MHz	5680 MHz
2	3.2 mA	100 MHz/V	5680 MHz	71	0.5	70 kHz	75 deg	20 MHz	1420 MHz
3	3.2 mA	100 MHz/V	5680 MHz	142	1	70 kHz	75 deg	10 MHz	1420 MHz
4	3.2 mA	100 MHz/V	5680 MHz	142	1	70 kHz	75 deg	10 MHz	5680 MHz

4.4.4 Analog Devices HMC 830

Figure 4.4.5 displays the HMC 830 evaluation board by Hittite Microwave (Analog Devices) [38].

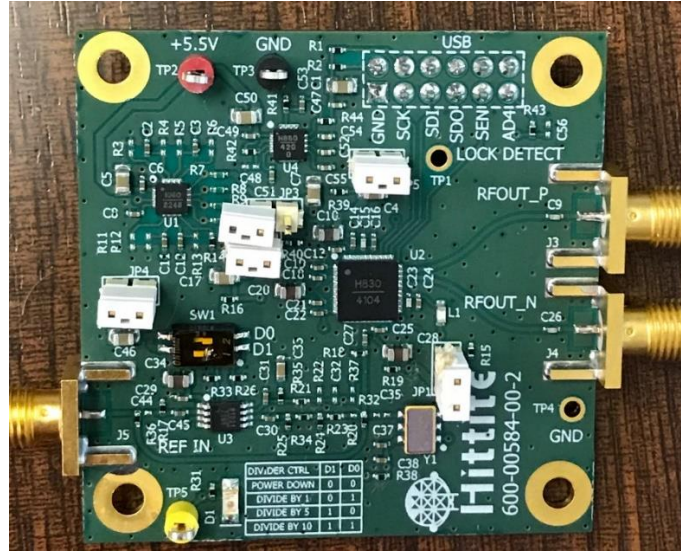


Figure 4.4.5: HMC 830 Evaluation Board from Hittite (Analog Devices)

Unlike the other devices, the HMC 830 has no reference input doubler. The HMC 830 also contains VCOs that can resonate at much lower frequencies. The benefit being that the VCO's frequency of 2840 MHz only needs to be divided by 2 to reach the desired 1420 MHz. The other devices' VCOs are not capable of operating this low in frequency.

Table 4.4.4: HMC 830 Configurations

#	I_p	K_{VCO}	f_{VCO}	N	M	BW	Phase margin	PF
1	2.54 mA	13.3 MHz/V	2840 MHz	284	1	100 kHz	75 deg	10 MHz

The phase noise and spur measurements were done with a Keysight PXA N9030B spectrum analyzer [39]. The OCXO's 10 MHz clock was used as the reference for the

FSPLLs and the spectrum analyzer. Doing so removes any oscillator drift or offset ambiguities from the phase noise measurements.

4.4.5 Spur Performance

Table 4.4.5 displays the spur performance of the LMX 2582 evaluation board under the different configurations shown in Table 4.4.1.

Table 4.4.5: LMX 2582 Spur Powers (dBc)

#	1430 MHz	1440 MHz	1450 MHz	1460 MHz	1470 MHz	1480 MHz	1490 MHz	1500 MHz	1510 MHz	1520 MHz
1	-57.34	-75.25	-76.12	-80.55	-84.65	-82.57	-89.53	-84.57	-83.66	-89.05
2	-57.14	-59.57	-76.25	-66.53	-85.15	-71.58	-91.17	-77.15	-97.19	-85.85
3	-74.90	-81.38	-84.18	-86.62	-88.05	-88.15	-89.41	-90.47	-92.13	-94.25
4	-60.93	-67.03	-70.56	-73.22	-75.51	-77.01	-78.67	-80.69	-83.10	-86.21
5	-56.76	-60.96	-75.99	-67.13	-84.37	-71.03	-89.47	-74.7	-93.71	-80.55

Figure 4.4.6 displays the captured phase noise and spurs of the LMX 2582 in its first configuration. The PXA has a frequency span 200 MHz. Spurs are present at 10 MHz offsets from the LO.

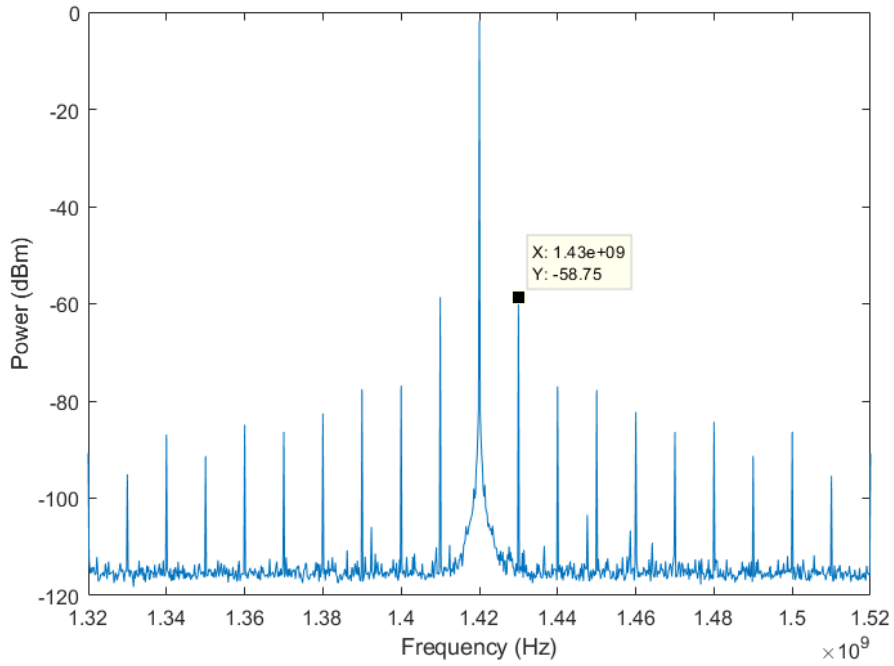


Figure 4.4.6: LMX 2582 Spurs in Configuration # 1

Spurs for the ADF 4355-2 configurations are shown in Table 4.4.6.

Table 4.4.6: ADF 4355-2 Spur Powers (dBc)

#	1430 MHz	1440 MHz	1450 MHz	1460 MHz	1470 MHz	1480 MHz	1490 MHz	1500 MHz	1510 MHz	1520 MHz
1	-41.77	-64.61	-61.37	-63.37	-71.97	-62.53	-87.80	-61.53	-80.98	-64.75
2	-42.03	-64.72	-61.84	-64.5	-72.69	-62.85	-87.88	-61.76	-83.63	-65.09
3	-42.07	-63.73	-62.40	-69.02	-72.81	-64.98	-77.00	-63.53	-74.02	-65.48
4	-42.07	-63.71	-62.39	-69.00	-72.82	-64.97	-77.08	-63.53	-74.02	-65.49

Spurs for the MAX 2871 are shown in Table 4.4.7.

Table 4.4.7: MAX 2871 Spur Powers (dBc)

#	1430 MHz	1440 MHz	1450 MHz	1460 MHz	1470 MHz	1480 MHz	1490 MHz	1500 MHz	1510 MHz	1520 MHz
1	-42.58	-72.53	-61.99	-78.87	-71.76	-82.31	-79.03	-84.43	-84.42	-85.77
2	-45.75	-73.66	-64.02	-79.58	-73.07	-83.92	-79.88	-87.96	-85.35	-91.75
3	-90.37	-88.27	-92.89	-90.61	-90.67	-92.78	-89.68	-96.13	-88.82	-98.83
4	-93.23	-98.84	-102.04	-95.14	-103.14	-93.17	-97.94	-92.84	-99.14	-92.59

Spurs for the HMC 830 are shown in Table 4.4.8.

Table 4.4.8: HMC 830 Spur Powers (dBc)

#	1430 MHz	1440 MHz	1450 MHz	1460 MHz	1470 MHz	1480 MHz	1490 MHz	1500 MHz	1510 MHz	1520 MHz
1	-84.7	-92.99	-96.63	-98.72	-101.88	-103.18	-108.08	-105.08	-107.08	-105.38

Figure 4.4.1 displays the captured spurs of the HMC 830.

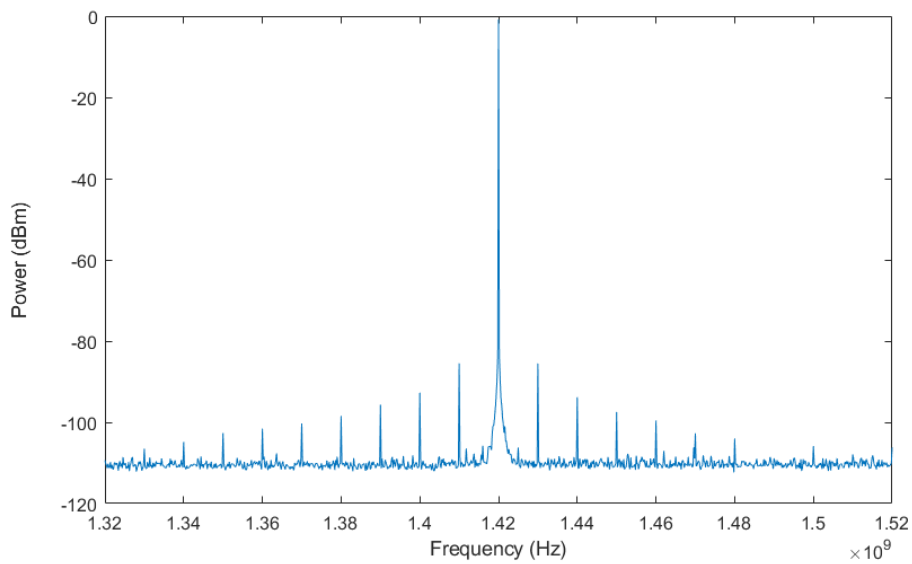


Figure 4.4.7: HMC 830 Spurs in Configuration # 1

The HMC 830 had the best spur performance for the given frequency plan. The frequency doubler used to increase the frequency of the RO before the PFD was used in the LMX 2582, MAX 2871, and ADF 4355-2. While this helps to decrease N , the spur power was increased by approximately 10 to 20 dB with the doubler enabled. The LMX 2582, MAX 2871, and ADF 4355-2 also need a VCO frequency of 5680 MHz, which is divided by 4 to reach 1420 MHz. This output divider contributes its own spurious activity to the device.

4.4.6 Phase Noise Performance

Phase noise from each configuration is calculated from integrating the SSB PSD from 10 Hz to 10 MHz and converting to RMS error in degrees by:

$$\sigma_{\phi} = \frac{180}{\pi} \sqrt{\int_{10}^{10E6} P_{\phi}(f) df}. \quad (52)$$

The PSD, $P_{\phi}(f)$, is normalized to the power of the carrier. The RMS phase error, σ_{ϕ} , is the parameter error estimate of the receiver tracking loops. Figure 4.4.8 shows how the phase noise data was gathered with the PXA N9030B [39]. 40 seconds of data were collected with a complex sample rate of 10 MHz with the PXA. The collected data were segmented into 40 blocks, each containing 1 second worth of data. A periodogram was calculated with the 40 blocks forming a reasonable estimate of the devices' phase noise with 1-Hz resolution. An RF low pass filter was placed on the output of the FSPLL to attenuate any odd-order harmonics that would otherwise be aliased by the PXA's ADC.

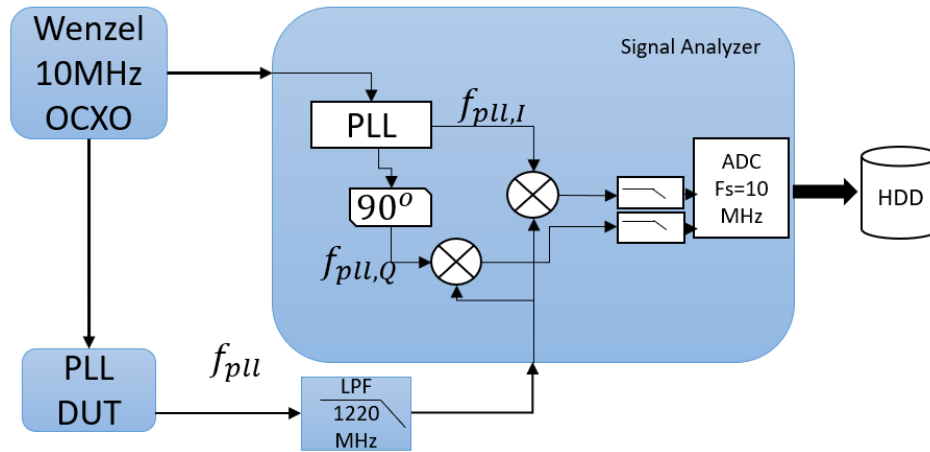


Figure 4.4.8: Phase Noise Collection with the Keysight PXA 9030B Spectrum Analyzer

[39]

Table 4.4.9 shows the integrated phase noise values for the configurations of the LMX 2582.

Table 4.4.9: LMX 2582 Integrated Phase Noise RMS Error

Configuration #	σ_{ϕ} (degs)
1	0.1187
2	0.0822
3	0.1366
4	0.1404
5	0.1079

Table 4.4.10 shows the integrated phase noise values for the configurations of the ADF 4355-2.

Table 4.4.10: ADF 4355-2 Integrated Phase Noise RMS Error

Configuration #	σ_{ϕ} (degs)
1	0.1203
2	0.1281
3	0.1209
4	0.1214

Table 4.4.11 shows the integrated phase noise values for the configurations of the MAX 2871.

Table 4.4.11: MAX 2871 Integrated Phase Noise RMS Error

Configuration #	σ_{ϕ} (degs)
1	0.1422
2	0.1312
3	0.1356
4	0.2209

Table 4.4.12 shows the integrated phase noise values for the configurations of the HMC 830.

Table 4.4.12: HMC 830 Integrated Phase Noise RMS Error

Configuration #	σ_{ϕ} (degs)
1	0.0794

Figure 4.4.9 displays the best-performing integrated phase noise configurations from each device.

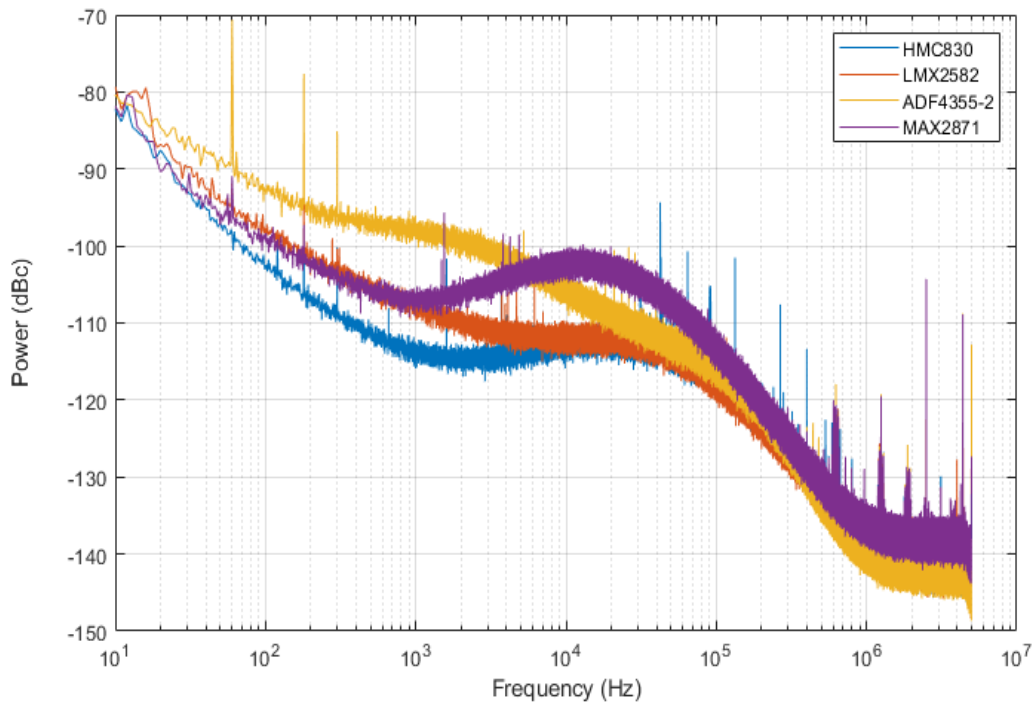


Figure 4.4.9: Phase Noise Measurements Taken from the Best Performing Configurations on Each Device

4.4.7 Frequency Synthesizer Evaluations Conclusions

The HMC 830 configuration was the best performing in terms of integrated phase noise and spurs. The device is more suited towards L-band LO synthesis due to its relatively low frequency VCOs integrated on-chip. The phase noise for the MAX 2871 looks as if the phase margin is lower than the designed value, due to the subtle peaking. The LMX 2582 performed best when utilizing the current multiplier on the charge pump, using the RO doubler and divide-by-4 pre-scalar. Small performance changes in integrated phase noise and spurs were noted in the ADF 4355-2 different configurations.

Changing the pre-scalar values or using the VCO output divider as feedback signal to reduce N had little effect on the phase noise. The feedback division still remains 284 for a VCO of 5680 MHz. Thus, the best way to reduce the feedback division is to increase the RO frequency and decrease the VCO frequency.

In the end, the LMX 2582 was chosen as the frequency synthesizer of choice due to the simple PCB layout and power requirements. While the HMC 830 did have better spur and phase noise performance, the LMX 2582 was easier to design with and offered similar phase noise performance.

4.5 Frequency Synthesizer Design

The PCB was built with the same stack up evaluated in the Section 4.2. Figure 4.5.1 displays the LMX 2582 soldered to the front-end. The various capacitors around the device are used decoupling, energy storage, DC blocking and the loop filter.

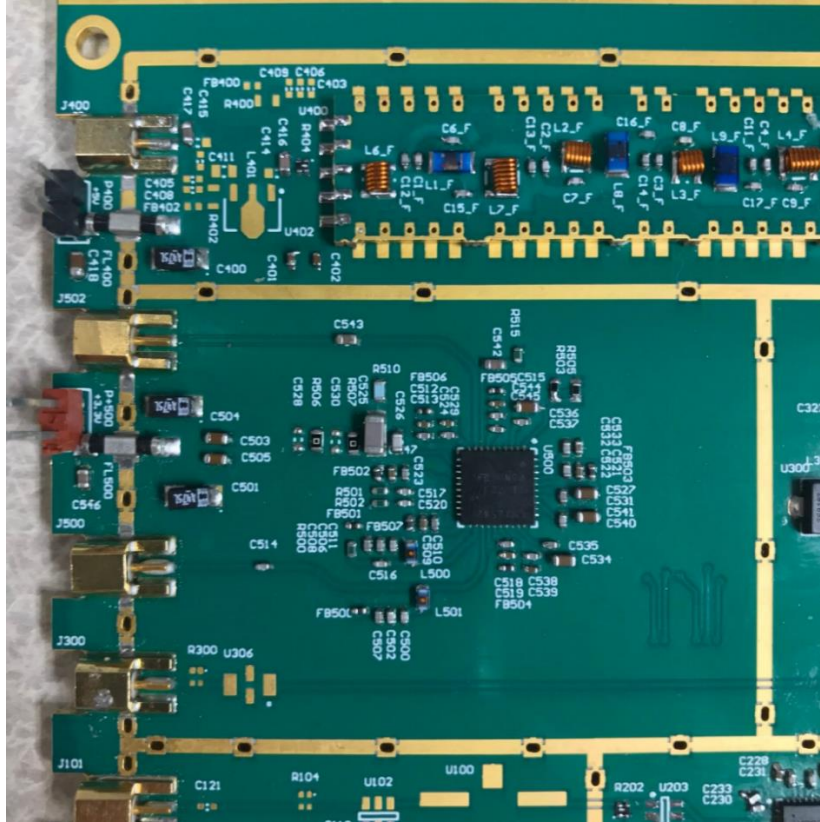


Figure 4.5.1: Constructed LMX 2582 Circuit

The LMX 2582 and loop filter were configured as # 2 in Table 4.4.1. COG temperature coefficient capacitors were used in the loop filter design. Proper RF layout guidelines and the manufacture’s recommended circuit design were followed. Ferrite beads were used on all power supply inputs of the device to prevent leakage and coupling to other inputs. The loop filter is routed on the bottom of the board, underneath the chip. Figure 4.5.2 displays the captured phase noise spectra obtained from the same procedure in Section 4.4.

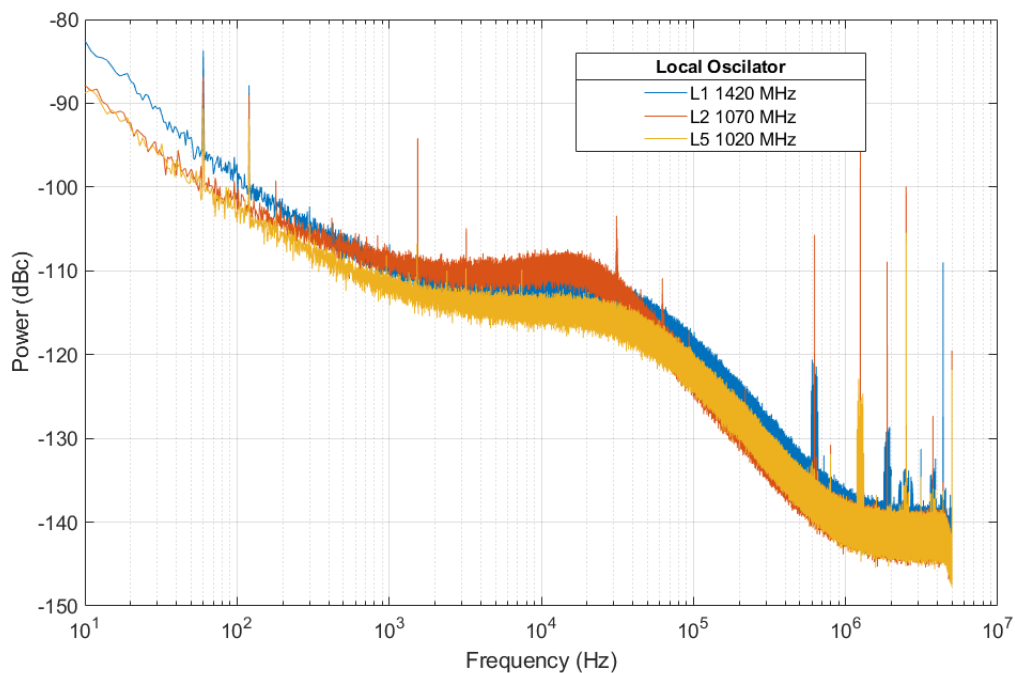


Figure 4.5.2: LMX 2582 Phase Noise at L1, L2, L5 LO

The results obtained in Figure 4.5.2 are comparable to the results from the evaluation board. If the reference oscillator's frequency of 10 MHz were to be multiplied up the L1 LO frequency of 1420 MHz, the phase noise of the reference would be increased by 21.5 dB. From Figure 3.6.1 the phase noise of the reference oscillator is increased to what it would be if it was multiplied by 142 and included in Table 4.5.1. The difference between the reference's PSD and the PLL's PSD is also shown.

Table 4.5.1: Frequency Synthesizer Performance vs Reference Oscillator

Frequency Offset (Hz)	OCCO @ 1420 MHz (dBc)	PLL @ 1420 (dBc)	Difference (dB)
10	-122.9	-82.5	40.4
100	-143.2	-98.7	44.5
1K	-151.5	-110.2	41.3
10K	-157.1	-112.5	44.6
100K	-157.1	-120.4	36.7

4.6 Power Supply Design

A 6V supply is used to power the board. Linear regulators create the required voltages for the board. Amplifiers, mixers, attenuators, and the RMS power detector run off a 5.0 V supply rail generated by low drop out regulator ADP3339 [40]. The 5.0 V supply is used by another RF linear regulator (ADM7150) [41] used to supply 3.3 V to FSPLL LMX2582. Figure 4.6.1 displays the power supply section of the PCB. A small heat sink was built to help dissipate heat created by the linear regulator.

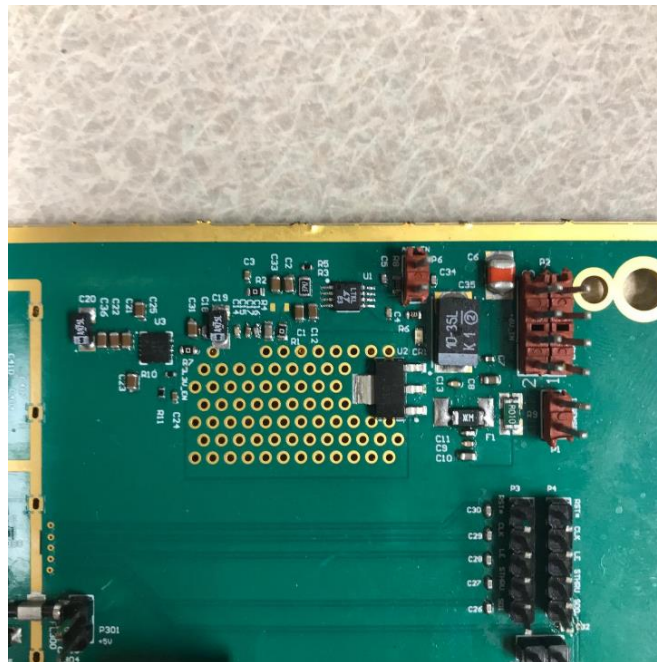


Figure 4.6.1: Front-End Power Supply Linear Voltage Regulators

RMS power measurements were made with a Lecroy 760Zi Oscilloscope [42]. The power signal is AC coupled when it sampled by the instrument. Figure 4.6.2 displays the AC coupled power rail off the 5.0 V linear regulator.

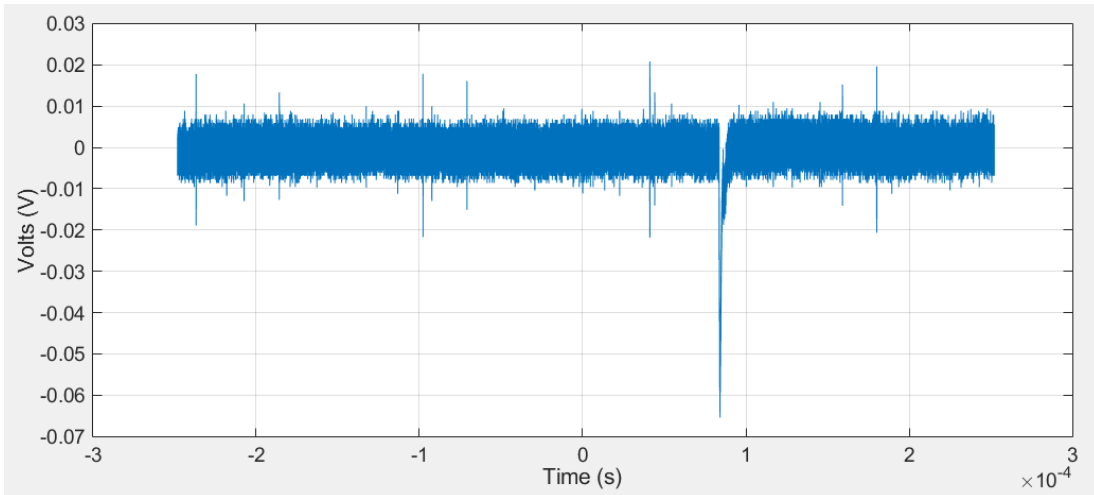


Figure 4.6.2: 5.0 V Linear Regulator Power from ADP3339 [40]

There is a definite spike in the power signal. This is caused by a power voltage supply to the regulator. The capacitance on the input and output of the regulator was not enough to filter the drop. Figure 4.6.3 displays the AC coupled output from the 3.3 V regulator used to power the LMX2582. There were no dropouts in the power due to the higher supply voltage. The LMX 2582 was active during the measurements.

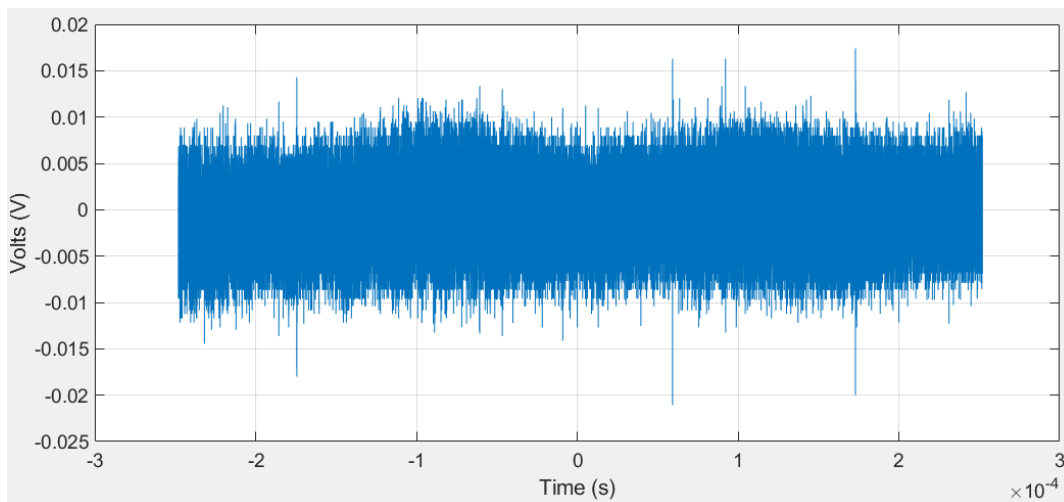


Figure 4.6.3: 3.3 V Linear Power Regulator from ADM7150 [41]

Figure 4.6.4 depicts the 6.0 V supply from the BK Precision [35].

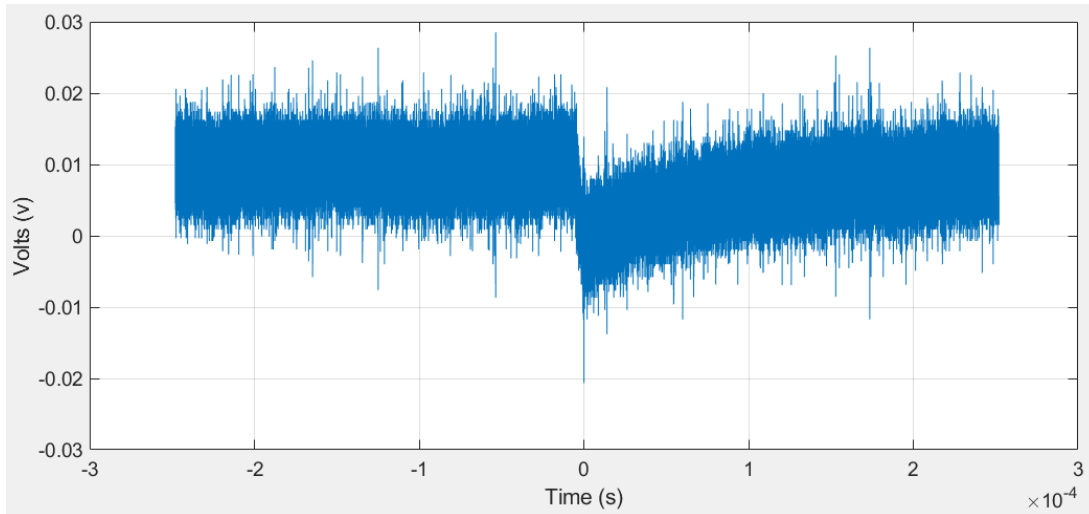


Figure 4.6.4: 6.0 V Power Supplied Through BK Precision [35]

There are some apparent voltage swings and drops in the voltage supply. In deployment of the front-end, better care in selection of the supply voltage will eliminate small dropouts in the regulators.

4.7 IF Filter Design

Three filters were assembled for L1, L2, and L5 variants of the front-end. Figure 4.7.1 displays the assembled filter on a surface mount coupon. This allows for changing the filter on the front-end as it is improved, or redesigned.

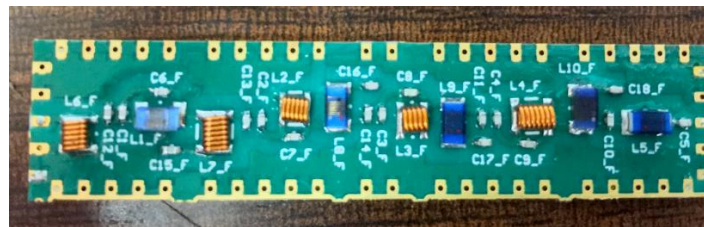


Figure 4.7.1: IF Filter Assembled on a Surface Mount PCB

Measurements of the IF filters were conducted with the Planar 403/1 VNA [34].

Repeatability of response and group delay is important for assessing the tolerance of the

design. High tolerance components were selected wherever available. The magnitude response and the group delay are shown in Figure 4.7.2 and Figure 4.7.3 respectively.

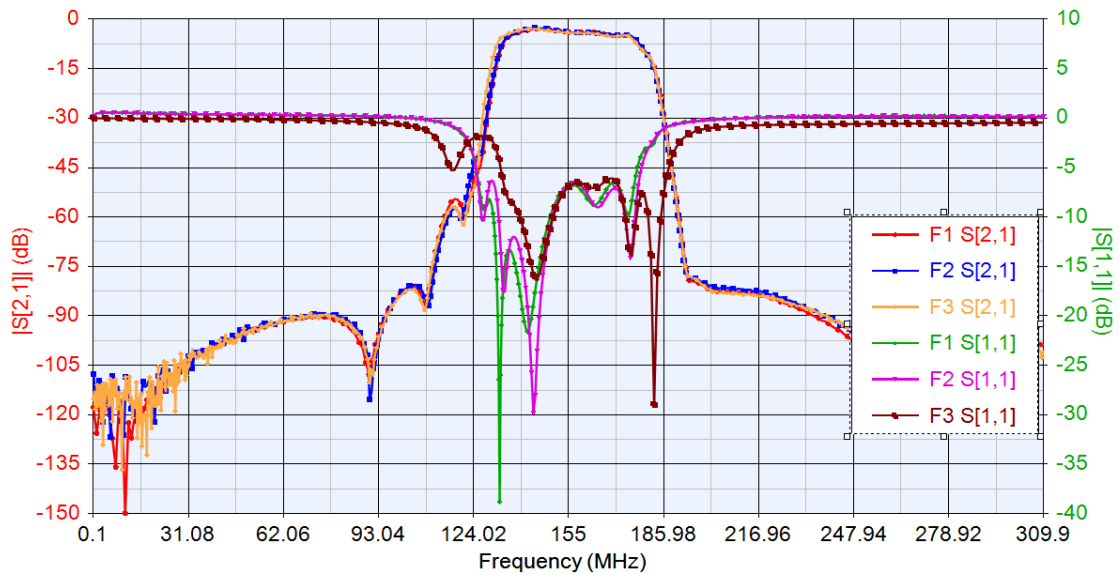


Figure 4.7.2: IF Filter Response and Repeatability

There is 4 dB of insertion loss from the filter, and -6.6 dB reflected. To improve matching of the filter, 3 dB attenuators are placed on either side. The Nyquist zone is between 125 MHz and 187.5 MHz. The attenuation at the edges of the stopband is -50 dB and -40 dB on the low side and high side respectively. A slight shift in the filter response and uncharacteristic shape at the lower end of the response are due to parasitics in the components not accounted for in the design process. The bandwidth of several GPS signals is overlaid on Figure 4.7.3 to provide a context for the amount of delay over the signal spectra.

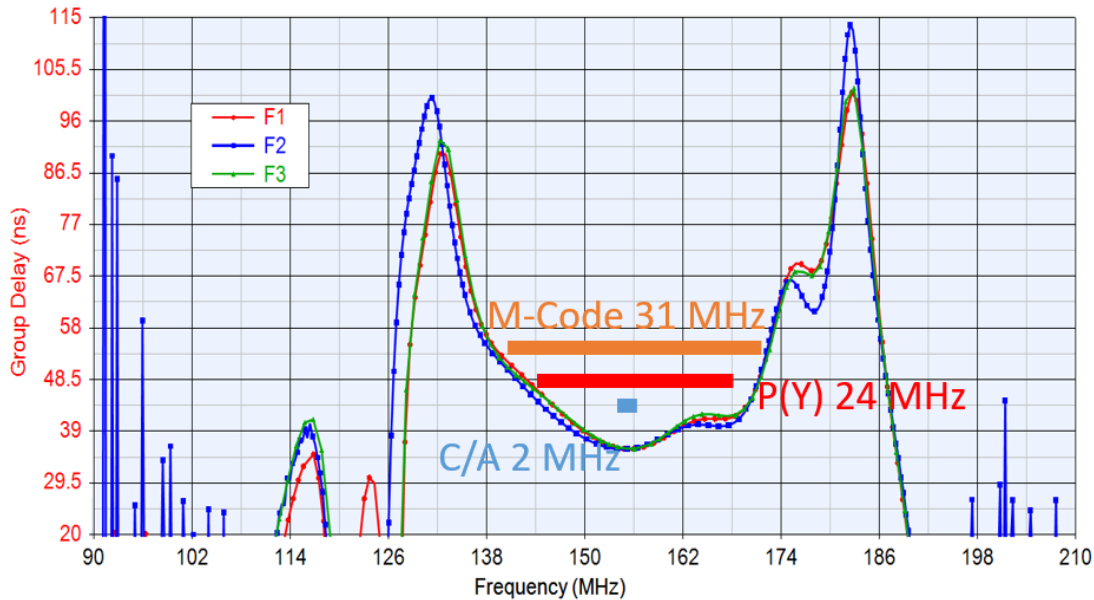


Figure 4.7.3: IF Filter Group Delay and Repeatability

In the design process, group delay variations were minimized across the satnav spectra. The satnav signals are mixed down to 155.42 MHz. At 2 MHz offsets at the center of the filter there is roughly 2 ns of group delay variations. At 6 MHz offset, it is closer to 6 ns of variation. There is an uncharacteristic shape to the group delay on the upper end of the filter; this is due to parasitics of the components or mutual coupling between inductors that were not modeled in the simulation. An electromagnetic simulation of the filter of the PCB substrate may help tune these undesirable responses out.

4.8 RF Portion of RF Front-End Design

The RF portion of the front-end is before the mixer in the signal path. Gain, linearity, image rejection, and group delay were all evaluated. Tools to evaluate noise figure were not available. Figure 4.8.1 displays the constructed RF portion of the front-end.

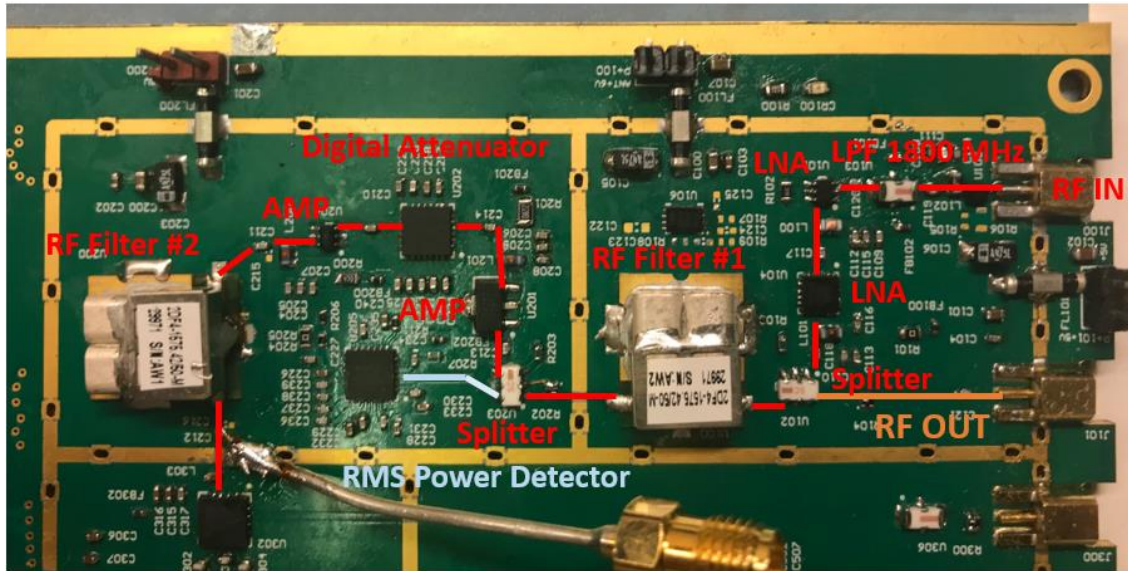


Figure 4.8.1: RF Portion and Layout of the Front-End

The RF portion consists of two rooms that will eventually be shielded to improve isolation between sections. The first RF room on the right contains two LNAs and a 50 MHz ceramic band pass filter centered at 1575.42 MHz. The signal is also split before the filter to provide an amplified RF output to other instrumentation. Figure 4.8.2 is the gain and linearity of the first RF room, measured before the RF filter.

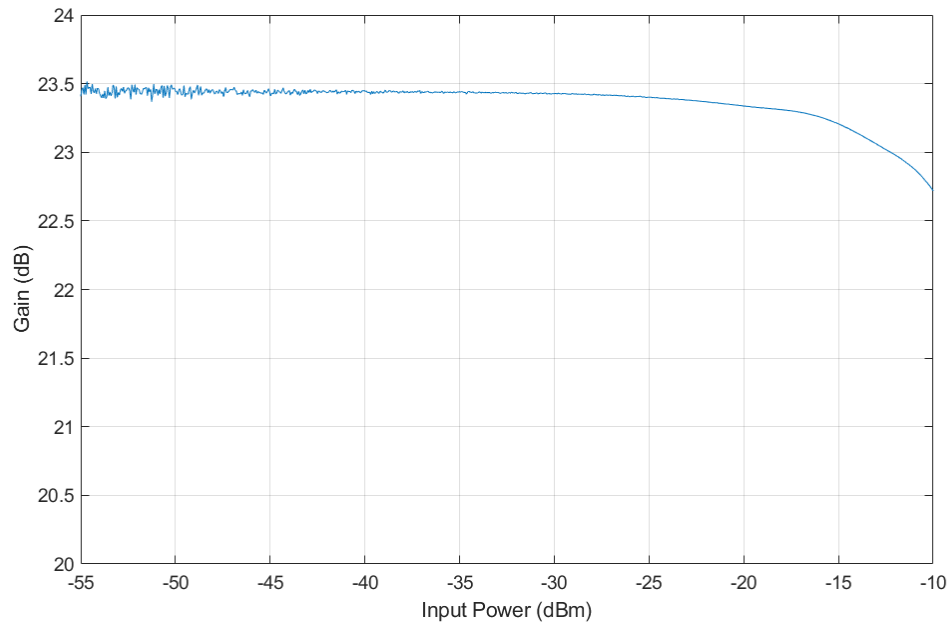


Figure 4.8.2: First RF Room Gain and Linearity

The section provides 23.5 dB of gain. The section begins to saturate at an input power of -26 dBm, the designed maximum input power of the RF front-end.

From Figure 4.8.1, after the first RF filter, the signal is attenuated by a 6 dB attenuator before being split again. One half goes to the RMS power detector, the other half to next amplifier in the signal chain. Next the gain and linearity of the entire RF portion was assessed. A digital attenuator can control the attenuator based on control signals sent from an Arduino. Figure 4.8.3 displays the gain and linearity of the entire RF portion with adjustments to the digital attenuator.

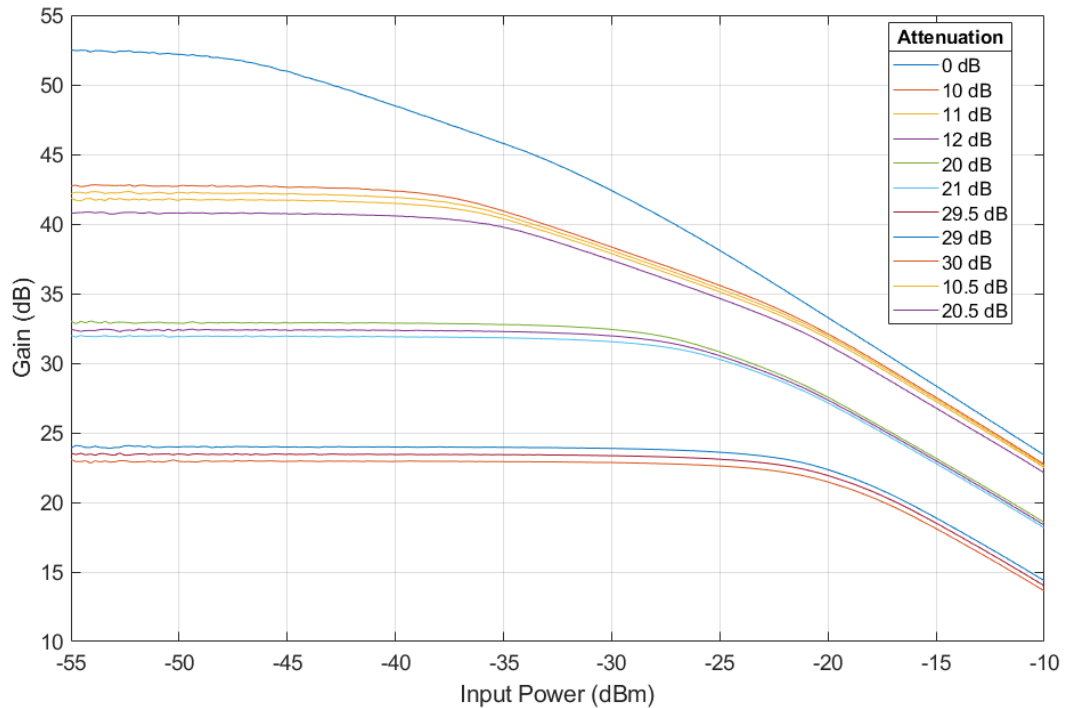


Figure 4.8.3: RF Gain and Linearity of RF Signal-Path

The attenuator has steps of 0.5 dB attenuation and offers up to -30 dB. The resolution of the attenuator step is validated in Figure 4.8.3. Once again, the RF portion begins to saturate at -26 dBm input power when maximum attenuation is provided by the digital attenuator.

Figure 4.8.1 shows two RF ceramic band pass filters populated on the board. There are many advantages to only using one filter: board space, cost, and group delay variations. Figure 4.8.4 displays the measured group delay of the RF portion using a single filter or two filters. Having minimal group delay variations over the satnav signal spectra will minimize the distortions imprinted upon the signal.

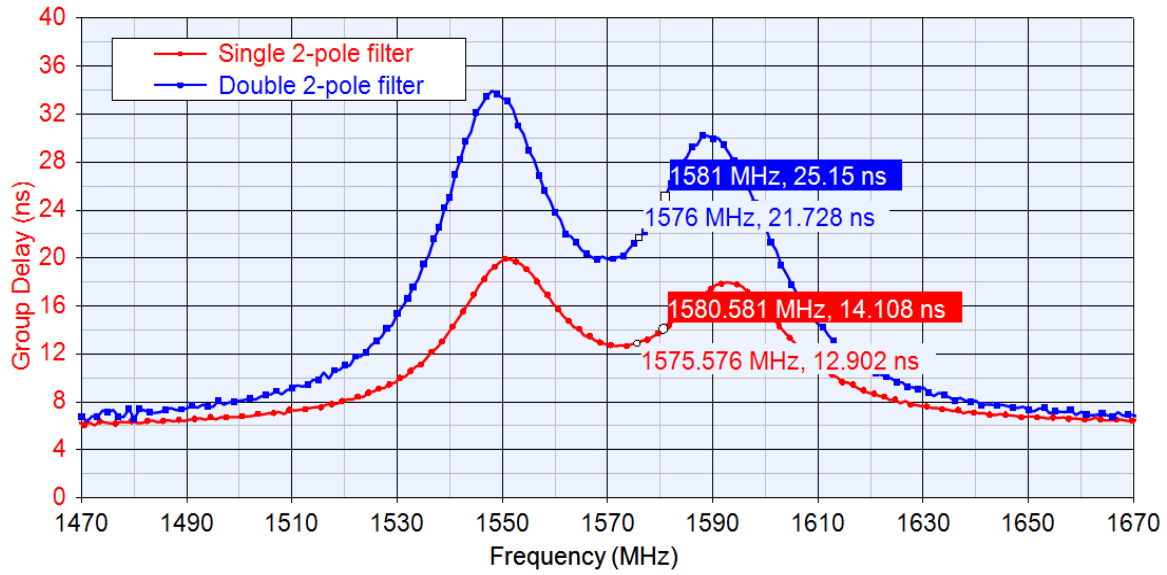


Figure 4.8.4: Group Delay of RF Signal Path

The group delay variations effectively double when using two filters. However, to make the case for using only one filter, there needs to be at least 70 dB of attenuation at the image frequency. Figure 4.8.5 displays the filter response with a signal filter, and two filters in the RF portion. 50 dBm of input power was applied, and the digital attenuator was set to -10 dB.

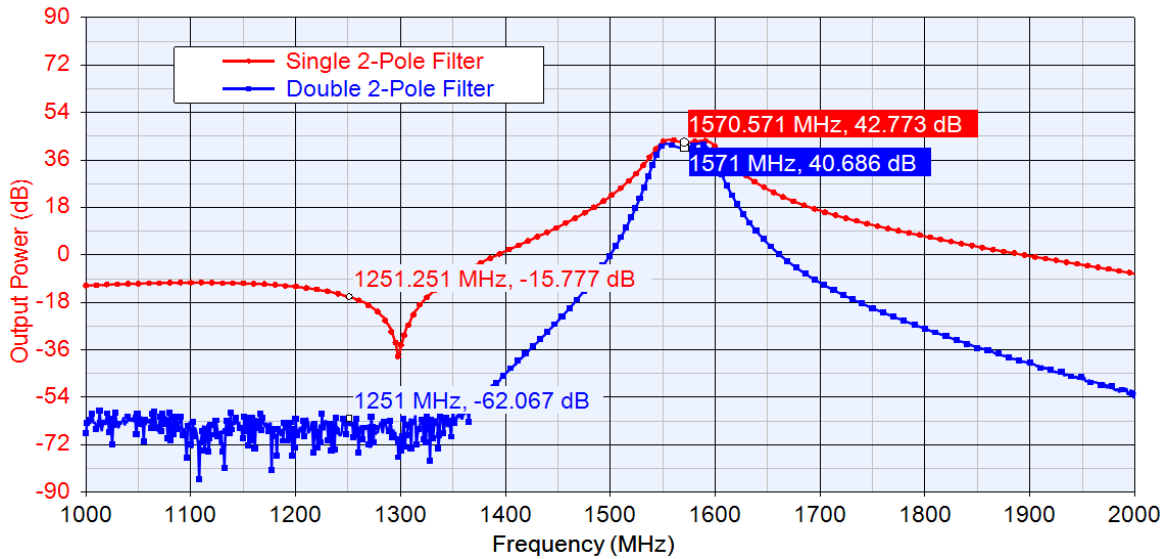


Figure 4.8.5: RF Filter Response of Signal Path

The single RF filter shows 58.47 dB of attenuation at the image. Two RF filters show 102 dB of attenuation at the image. Under certain circumstances, the image rejection of the single filter may be adequate.

4.9 IF Portion of RF Front-End Design

Figure 4.9.1 displays the IF signal path of the front-end. The IF portion of the board consists of the signal path after the signal has been down converted by the mixer to 156.25 MHz. The matching elements for the output of the mixer were taken from the mixer's data sheet. A low pass filter removes the high portion of the converted signal.

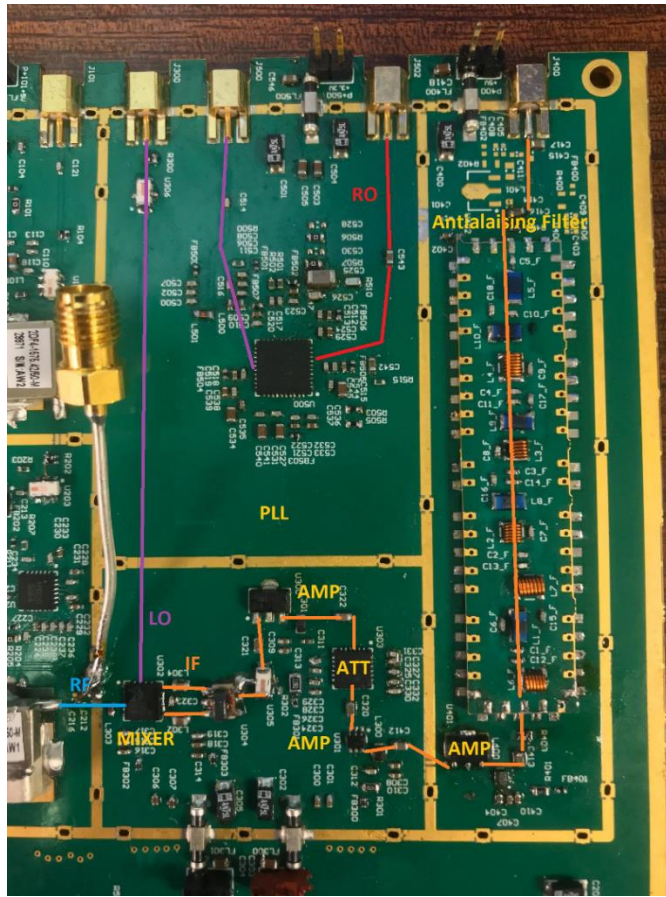


Figure 4.9.1: IF Portion of the Front-End

Gain, linearity and group delay are measured across the IF portion of the board. Figure 4.9.2 displays the gain and linearity as the digital attenuator is adjusted.

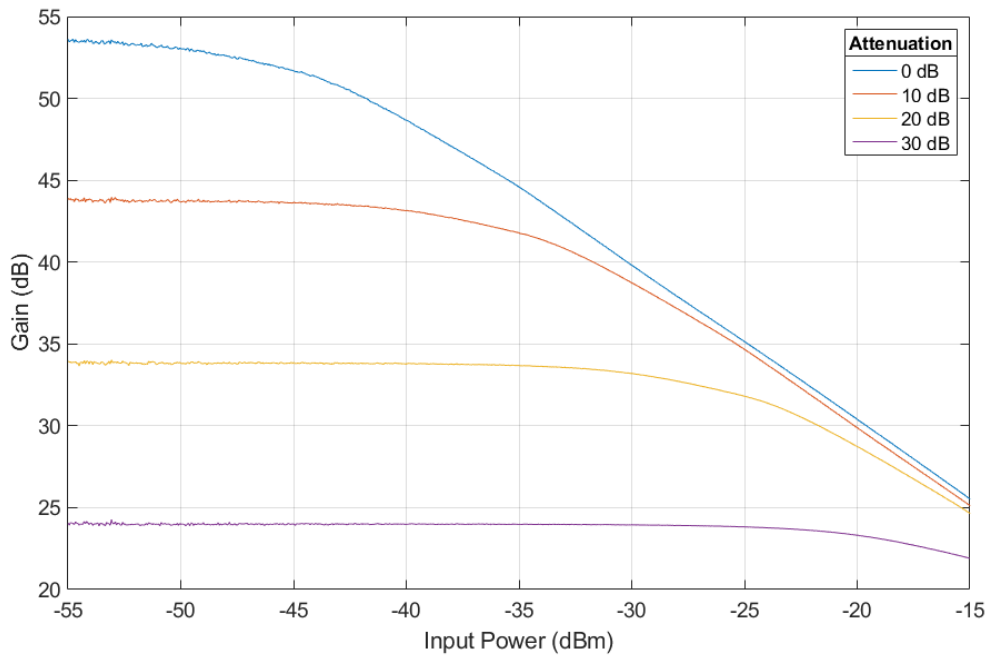


Figure 4.9.2: IF Portion Gain and Linearity of the Front-End

The RF portion of the board can supply a maximum of -7 dBm of power to the IF section, when under the duress of 100 dB J/S. The TQP369182 is the first amplifier in the signal path in the IF portion, thus it must handle the maximum input of power of -7 dBm without saturating. The TQP369182 has 15.1 dBm P1dB output power and 21 dB of gain, the max input power is -6 dBm. Thus, the device will operate in its linear region under the maximum -7 dBm. However, Figure 4.9.2 shows that IF portion can only handle a maximum -25 dBm of input power before saturating. This is due to the amplifier that was populated before the IF filter. This amplifier was not included in the simulation of the front-end, and will have the option to be excluded in future revisions.

Figure 4.9.3 displays the IF filter response and the group delay of the IF portion of the board. The input power was -40 dBm, and the attenuator was set to 20 dB.

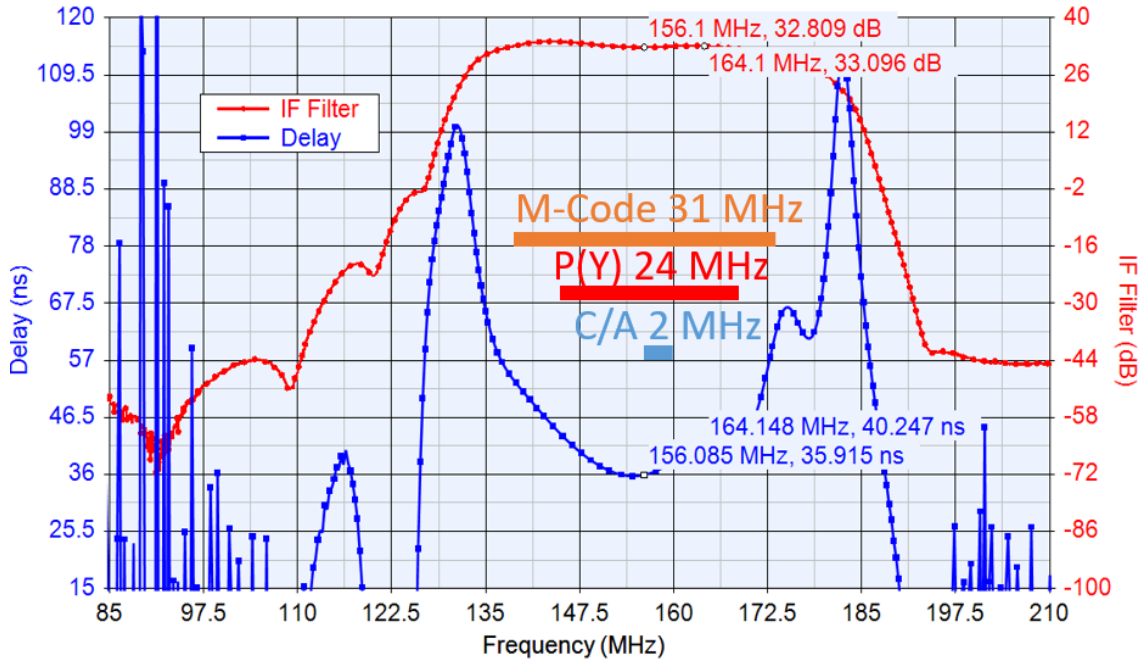


Figure 4.9.3: IF Portion Response and Group Delay of the Front-End

At an 8 MHz offset from the center of the IF, there is approximately 4.3 ns of delay. The response and the group delay of the IF portion can be improved upon.

4.10 Analog to Digital Converter Evaluation Results

The AD 9681 evaluation board [43] was purchased to validate the functionality of the constructed front-end. The Visual Analog [44] evaluation software was used to interface to the board. A 125 MHz sample clock signal to the ADC was provided by a low phase noise Keysight MXG N5182B [45]. Samples from the AD 9681 are stored in a finite buffer before being read out to a host computer over USB 2.0. Figure 4.10.1 displays the evaluation board supplied with power, the IF input signal, and the 125 MHz clock.

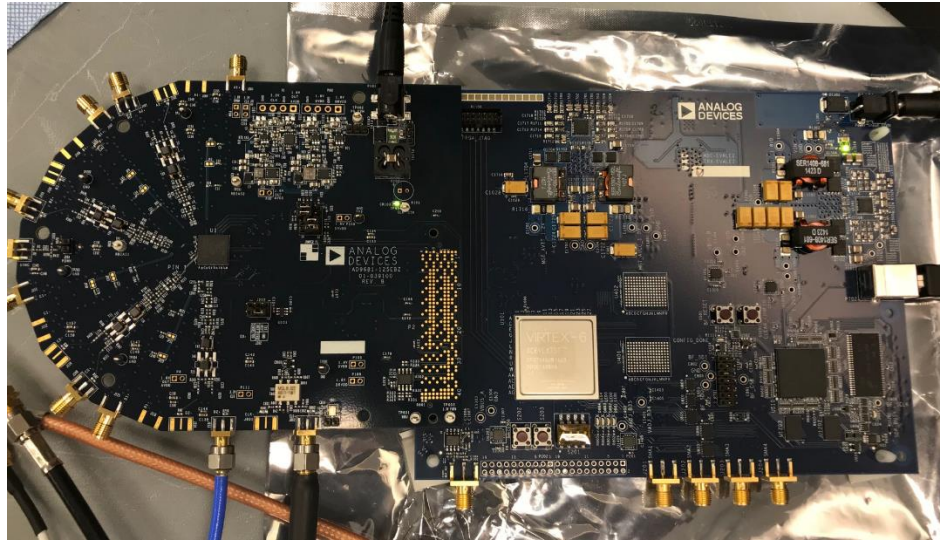


Figure 4.10.1: AD 9681 Evaluation Board

Unfortunately, the evaluation board is unable to supply the host computer with more than 2 ms of sampled data. Satnav acquisition can be run on the recorded data, but not signal tracking. Figure 4.10.2 displays a periodogram over 1 second from a live-sky antenna. There are signals present on the lower end of the captured spectrum that reside in the Space-to-Earth allocated spectrum. The center of the PSD contains noticeable hump, attributed to the many satellites broadcasting CDMA signals at that frequency. There are some other notable spectra elements on either side of the PSD that may attributed to the Compass B1 BOC(14,2) and GLONASS FDMA.

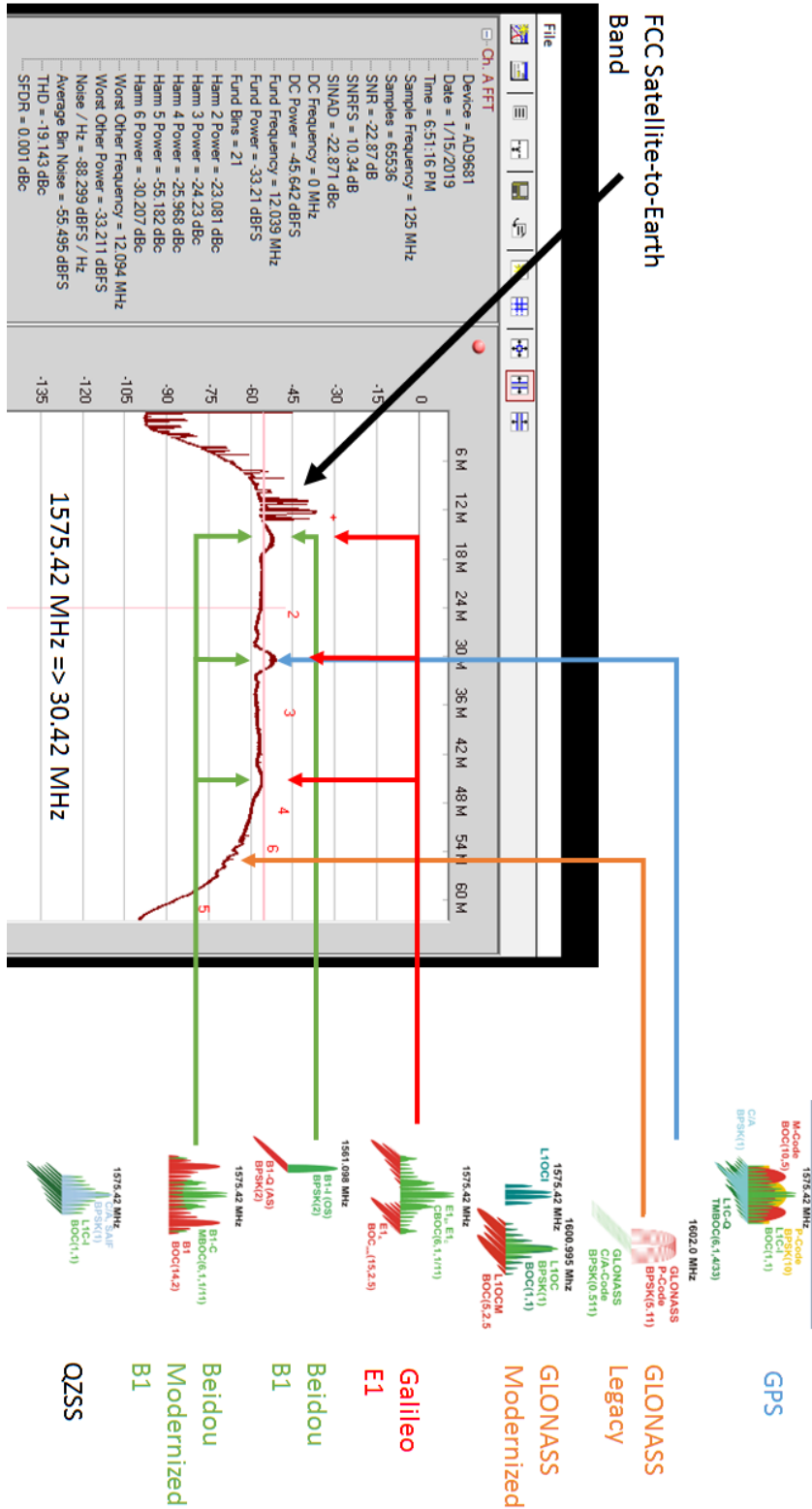


Figure 4.10.2: ADC PSD from Live-sky Antenna

4.11 Software Defined Satnav Signal Tracking & Front-End Results

Due to inability of the AD 9681 Evaluation board's software to collect and store more than 2 ms of samples, an alternative solution for collecting data from the front-end needed to be found in a short timeline. The Keysight PXA [39] spectrum analyzer has a high sample rate ADC. Similar to the method the frequency synthesizer's phase noise data was collected, so too was the IF from the front-end. Figure 4.11.1 and Figure 4.11.2 displays the front-end being evaluated end-to-end with either live-sky signals or from a simulator.

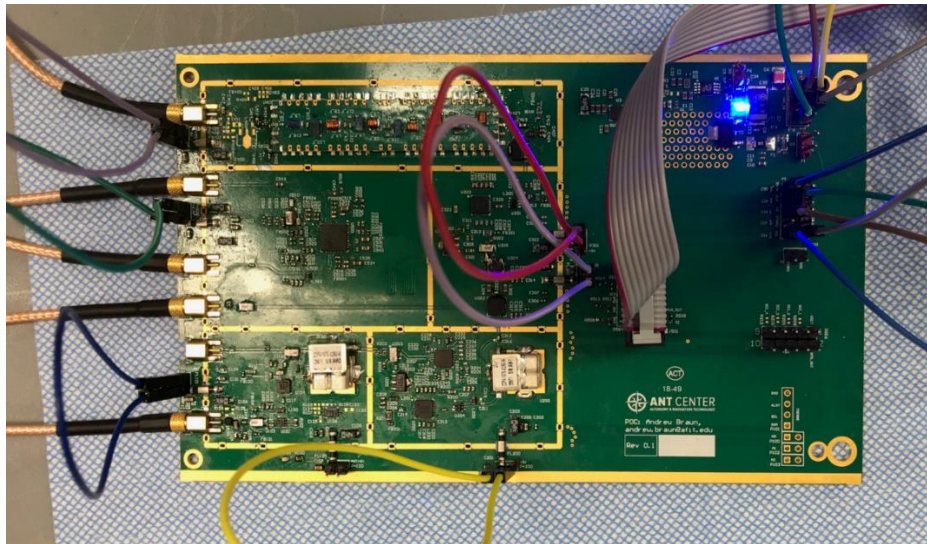


Figure 4.11.1: RF Front-End Under Test

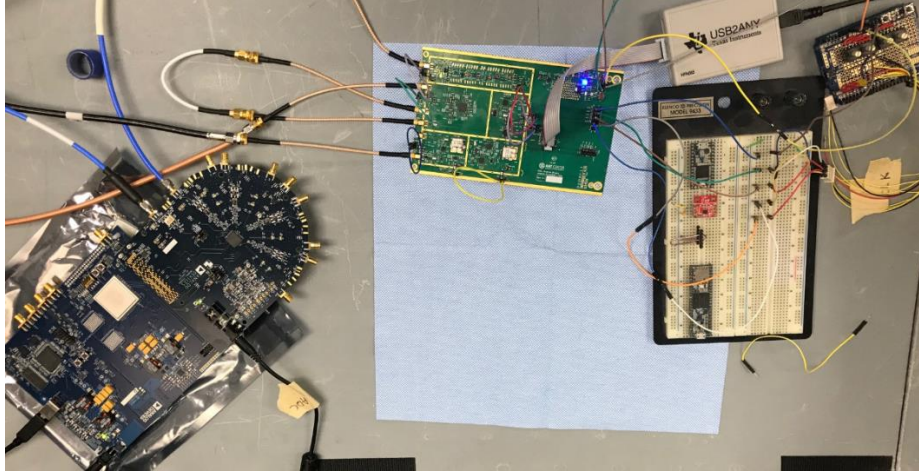


Figure 4.11.2: RF Front-End Under Test with Arduino and ADC

The Arduino is used to control the gain of the front-end through the programmable attenuators. The performance of the front-end is evaluated with different LOs, and compared against the results of pure software defined GNSS receiver.

4.11.1 Simulator Signal Tracking

Providing the front-end with a simulated satnav signal with a known doppler and code provides a constant for evaluating the quality of the LO. A Rohde & Schwarz (R&S) SMBV100A [46] Vector Signal Generator was used to supply a simulated L1 C/A satnav signal with 0 doppler and enough power for approximately 45 dB CNR. The IF output of the front-end was down converted to baseband by the Keysight PXA Spectrum Analyzer [39] and sampled with a 6 MHz span. The Synergy Microwave LFSW80210-100 was used as the baseline for providing an LO to the front-end to compare against the LMX 2582. The LFSW80210-100 is a proven frequency synthesizer used in high fidelity signal monitoring front-ends [47]. The R&S satnav simulator, the Keysight PXA spectrum analyzer, the LMX 2582 PLL on the front-end, and the Synergy Microwave synthesizer

are all locked to the same 10 MHz reference provided by an OCXO [25]. This eliminates any long-term drifts or frequency offsets of the references internal to the instruments.

Therefore, only the short-term phase noise of the LO synthesizer is evaluated.

As another baseline, the front-end's carrier phase tracking noise is compared against a Septentrio PolaRx5 [48]. The tracking loop order, pre-detection integration time, and loop bandwidth are known for the PolaRx5 receiver. The same tracking parameters are then used in the software defined receiver with the designed front-end to keep the measurements consistent. A power splitter, with 50 Ω 30 dB attenuators attached to each port to improve matching, was used to distribute power to the front-end under test and the Septentrio PolaRx5. The output power of the R&S simulator was adjusted until the Septentrio receiver reported 45 dB-Hz CNR.

4.11.1.1 LMX 2582 as the Local Oscillator

Figure 4.11.3 displays the test setup for evaluating the LMX 2582 FSPLL circuit built onto the front-end.

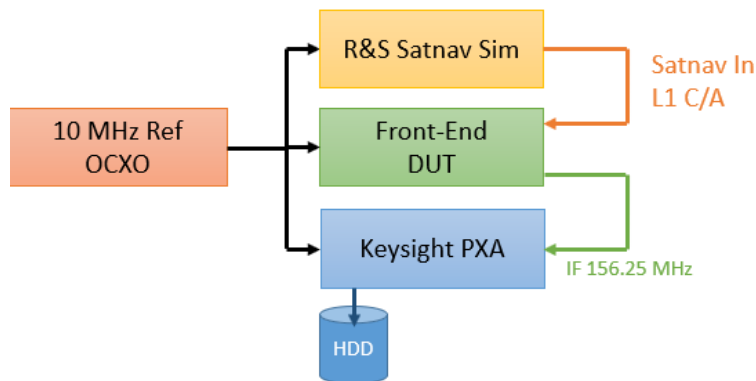


Figure 4.11.3: Simulated Satnav Signal Testbed with LMX 2582 LO

Being that there is no dynamics on the signal, a 1st order PLL with a loop noise bandwidth of 15 Hz and a prediction integration time of 10 ms was used to track the simulated signal. Table 2.15.1 contains the loop filter values that were used in the software receiver. Figure 4.11.4 shows the sampled waveform and spectrum of the captured data. The sampled data was processed in the software receiver with 8 bits of dynamic range.

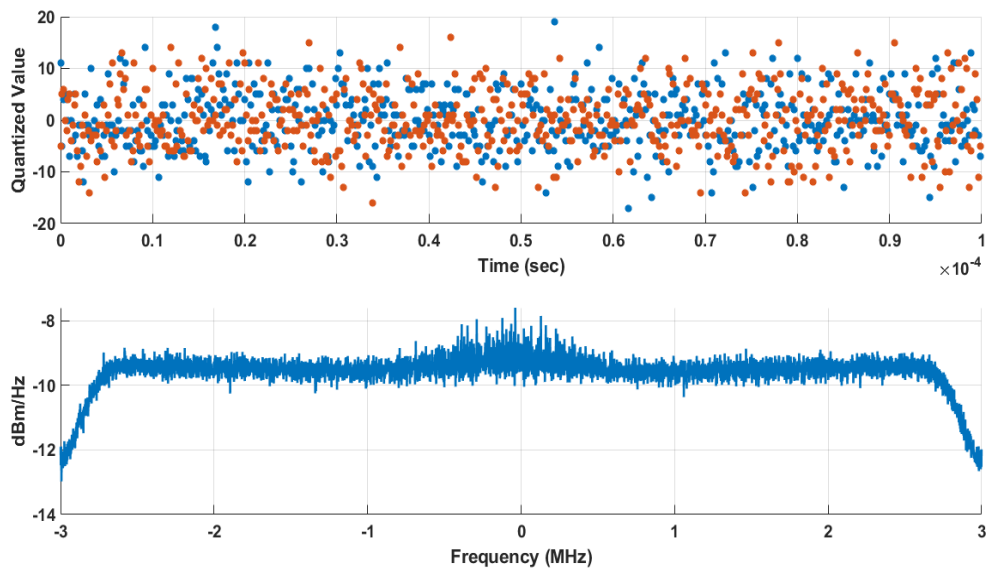


Figure 4.11.4: PSD and Time-Domain Sample Snapshot of R&S Simulated Satnav Data

The output power of the R&S satnav simulator was set to the power at which the Septentrio PolaRx5 reported 45 dB-Hz CNR. 80 seconds of data was recorded with the PXA spectrum analyzer. Figure 4.11.5 displays the measured CNR in the software defined receiver.

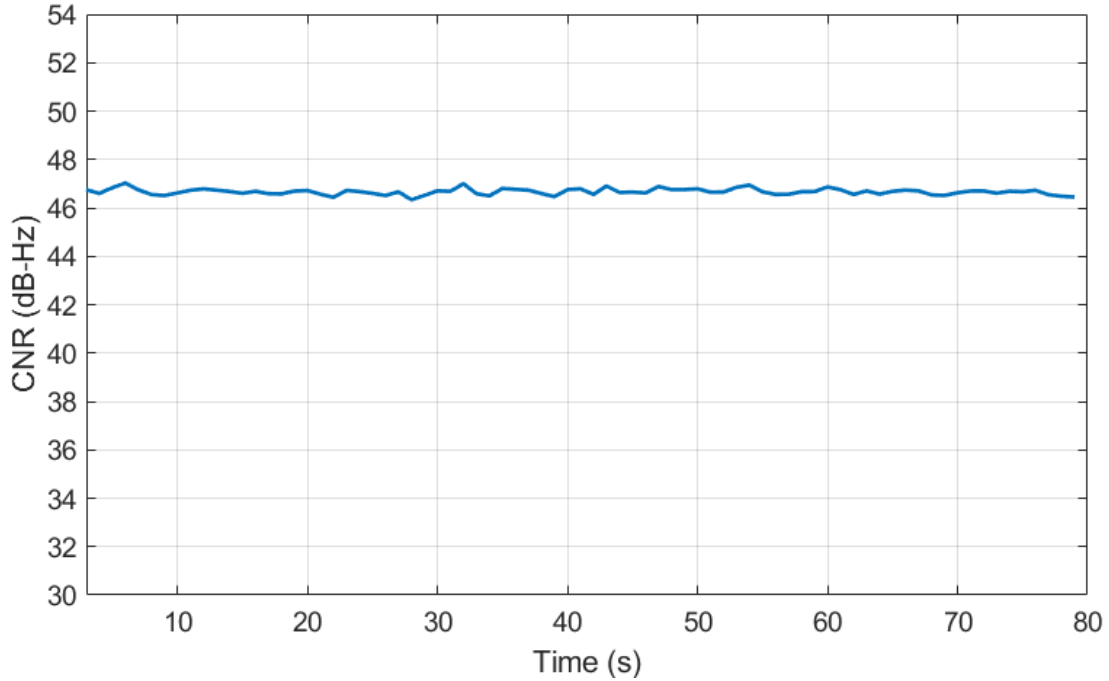


Figure 4.11.5: Measured CNR When Using the LMX 2582 as the LO

The software defined receiver’s CNR measurements from the front-end are approximately 1.5 dB higher than the Septentrio PolaRx5. This is due to the high level of sensitivity of the front-end. Based on a CNR measurement of 46.7 dB-Hz, the thermal noise contributions to the phase tracking error is:

$$\sigma_{\phi}(m) = 0.00054 (m) = \left(\frac{0.190293673}{2\pi} \right) \sqrt{\frac{15}{10^{\frac{46.7}{10}}} \left(1 + \frac{1}{2 * .01 * 10^{\frac{46.7}{10}}} \right)}. \quad (53)$$

Figure 4.11.6 displays the carrier tracking state of the PLL. The 1st order PLL pulls in the phase offset of the signal and transitions a longer integration time of 10 ms after 2 seconds into processing.

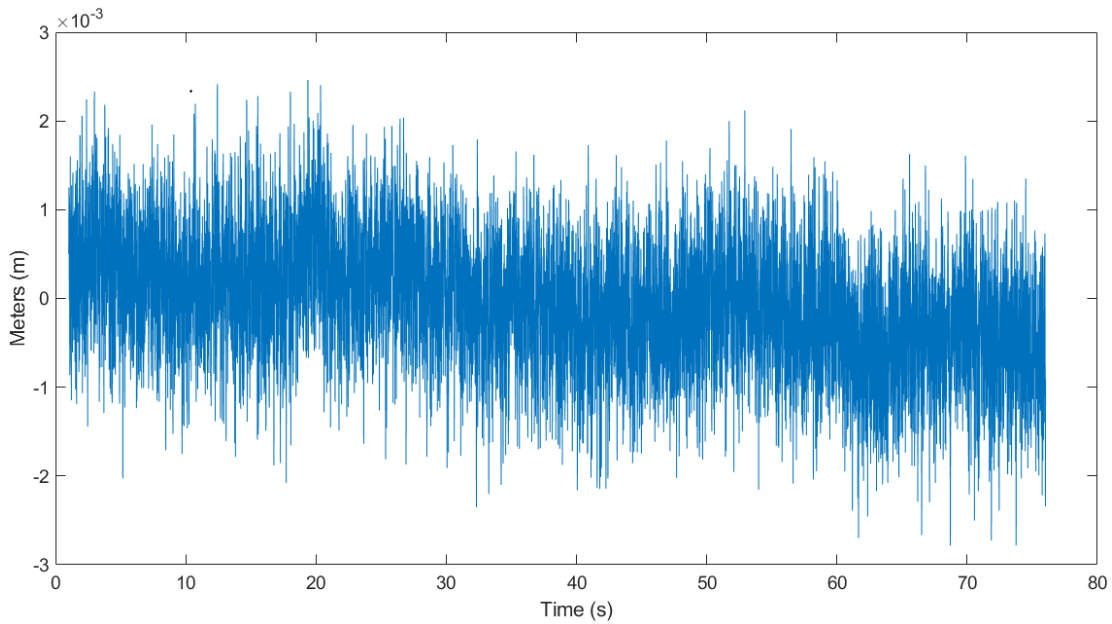


Figure 4.11.6: Carrier Filter Tracking States LMX 2582 PLL LO

The phase noise generated by the LMX 2582 LO, the R&S simulator, and the Keysight PXA will all degrade the signal tracking capability. The measured RMS carrier phase tracking error was 0.00068 (m). This is 0.00014 (m) worse than the estimated thermal noise contributions to the carrier phase error (53). Referring to Table 4.4.9 configuration #2, the integrated RMS phase noise of the LMX 2582 is 0.0822° , converting to meters is 0.00004 (m). In reality, the phase noise of the frequency synthesizers of the R&S simulator and the Keysight PXA spectrum analyzer are also going to contribute phase noise to the satnav signal which will further degrade the carrier phase measurements.

4.11.1.2 Synergy Microwave Frequency Synthesizer as the Local Oscillator

The Synergy Microwave LFSW80210-100 was used to supply the LO to the front-end as a baseline comparison to the front-end's LMX 2582 LO. The Synergy Microwave FSPLL is locked to the same external 10 MHz reference as shown in Figure 4.11.7.

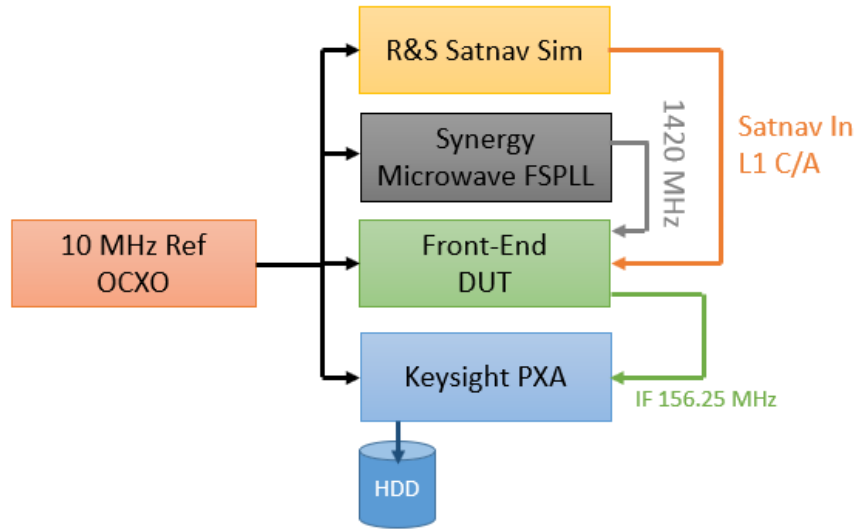


Figure 4.11.7: Simulated Satnav Signal Testbed with Synergy Microwave LO

Input power to the front-end was kept the same as the previous test. The CNR when using the Synergy Microwave LO was increased by approximately 1 dB. Figure 4.11.8 shows the CNR measurements between the LMX 2582 LO and the Synergy Microwave LO.

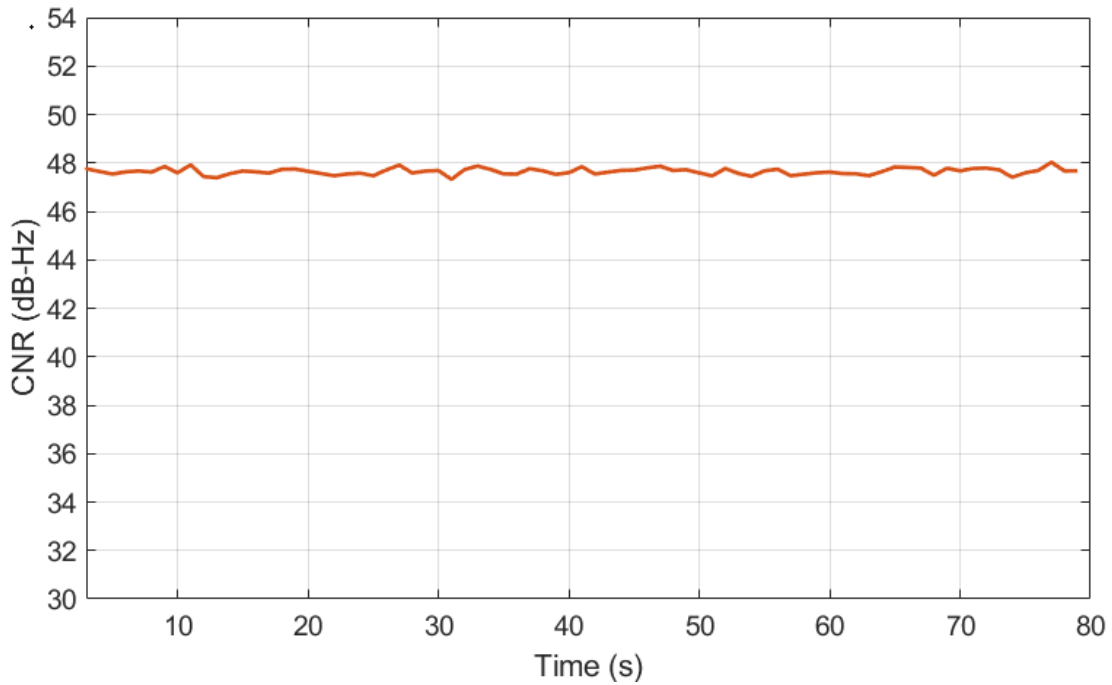


Figure 4.11.8: CNR Measurements Using the Synergy Microwave LO

The improved CNR is due to better phase noise and spur performance of the Synergy Microwave over the LMX 2582. The RMS phase tracking error can again be estimated through:

$$\sigma_{\phi}(m) = 0.00049 (m) = \left(\frac{0.190293673}{2\pi} \right) \sqrt{\frac{15}{10^{\frac{47.7}{10}}} \left(1 + \frac{1}{2 * .01 * 10^{\frac{47.7}{10}}} \right)}. \quad (54)$$

Figure 4.11.9 displays the carrier filter tracking states using the Synergy Microwave as the LO to the front-end. The same tracking parameters were used in the software defined receiver from testing the LMX 2582 as the LO.

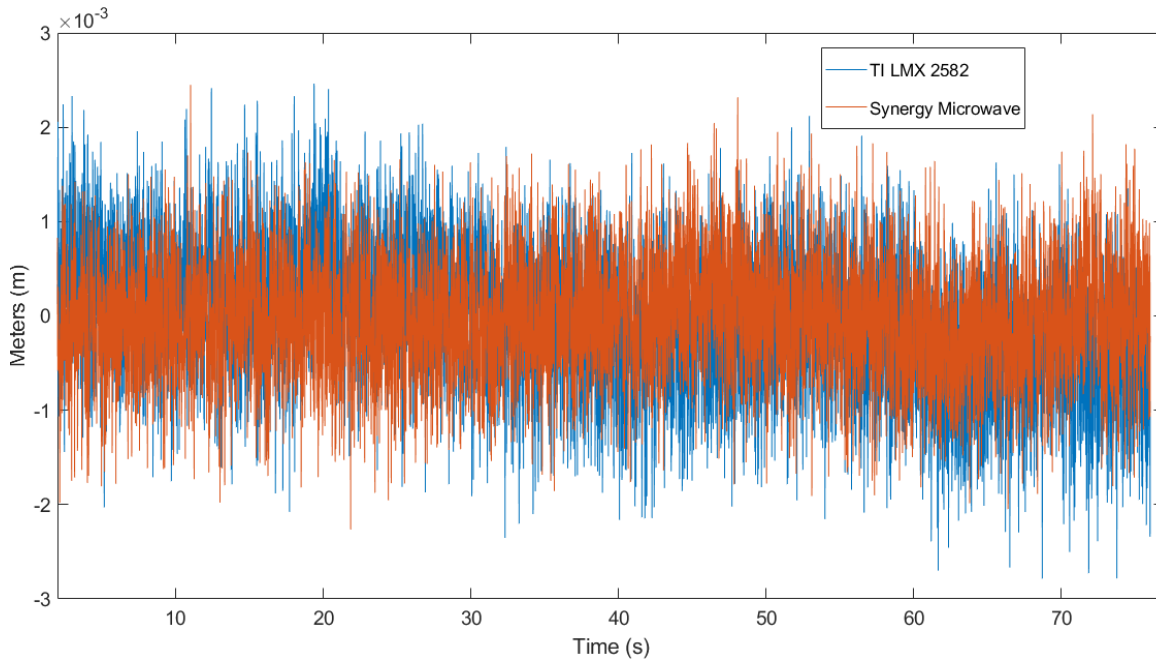


Figure 4.11.9: Carrier Filter Tracking States Using the Synergy Microwave FSPLL as LO
Plotted Overtop the TI LMX 2582

The receiver carrier phase RMS range error is 0.00056 (m). The theoretical calculated RMS error is 0.00049 (m), there is a 0.00007 (m) difference between what was measured and the estimated thermal noise. The difference is due to the phase noise of the Synergy Microwave, R&S, and Keysight PXA synthesizers. The carrier tracking RMS noise is 0.00012 (m) better than the LMX 2582, most likely due to the small amount of drift in the LMX 2582's carrier phase. There is no apparent drift of Synergy Microwave FSPLL.

4.11.1.3 Septentrio PolaRx5 Receiver vs. the Receiver Front-End

The other half of the signal from the R&S satnav simulator goes to a Septentrio PolaRx5 receiver [48]. The receiver was configured to use the same external clock as the R&S simulator. The receiver is using a loop bandwidth of 15 Hz and pre-detection integration time of 10 (ms). Longer periods of data from the Septentrio PolaRx5 receiver

could be logged than storing just the raw samples. A 500 second portion of the CNR data is displayed in Figure 4.11.10.

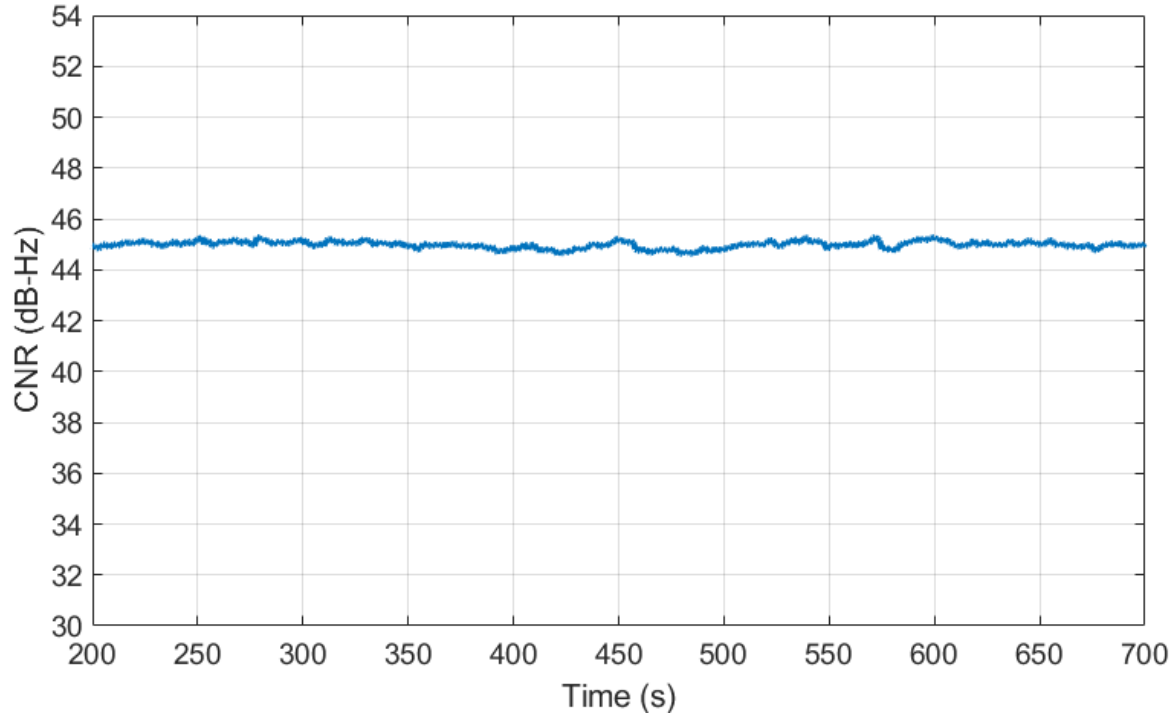


Figure 4.11.10: CNR Measured from Septentrio PolaRx5 Receiver

Based on the CNR measurements from the receiver, the carrier phase tracking error can be estimated through:

$$\sigma_{\phi}(m) = 0.00066 (m) = \left(\frac{0.190293673}{2\pi} \right) \sqrt{\frac{15}{10^{\frac{45}{10}}} \left(1 + \frac{1}{2 * .01 * 10^{\frac{45}{10}}} \right)}. \quad (55)$$

The carrier phase measurements made by the Septentrio PolaRx5 receiver are shown in Figure 4.11.11.

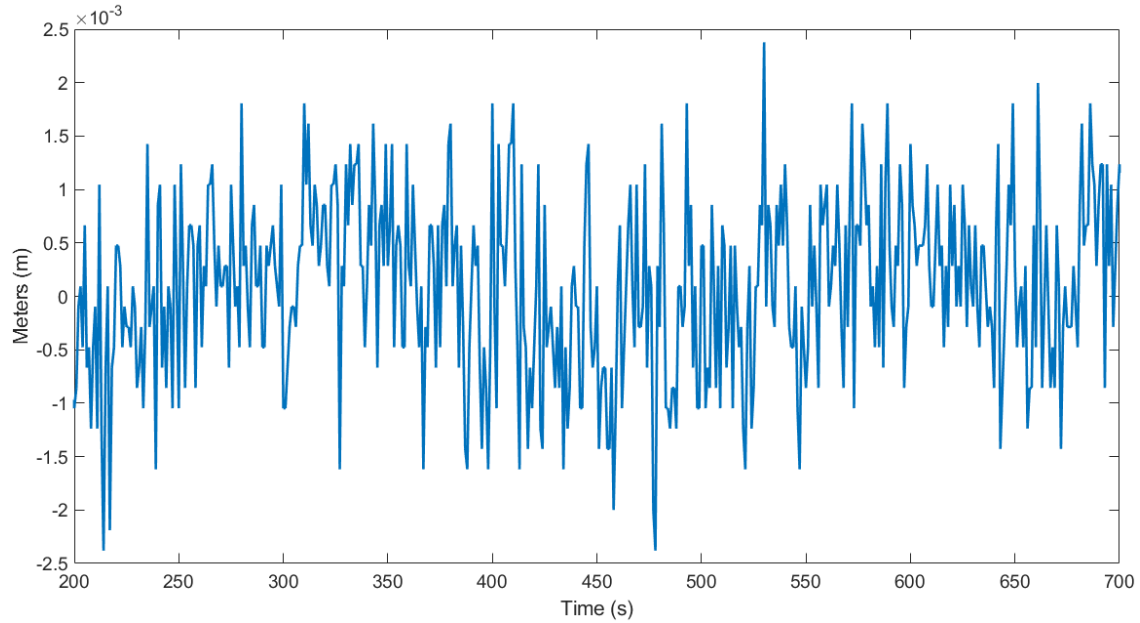


Figure 4.11.11: Carrier Phase Measurement Residuals with Septentrio PolaRx5

The measured RMS error of the tracking loops is 0.00083 (m). The measured RMS error is 0.00017 (m) off from the estimated RMS error (55).

Power was distributed equally to the Septentrio PolaRx5 and the constructed front-end. The front-end has 1.5 dB higher CNR than the Septentrio PolaRx5 due to its higher sensitivity and cleaner LO.

4.11.2 Live-Sky Signal Acquisition and Tracking

The front-end is supplied a live-sky feed from an active antenna. The Keysight PXA was set to sample the IF output from the front-end at 62.5 MHz. Figure 4.11.12 shows the experimental setup for collecting the live-sky data.

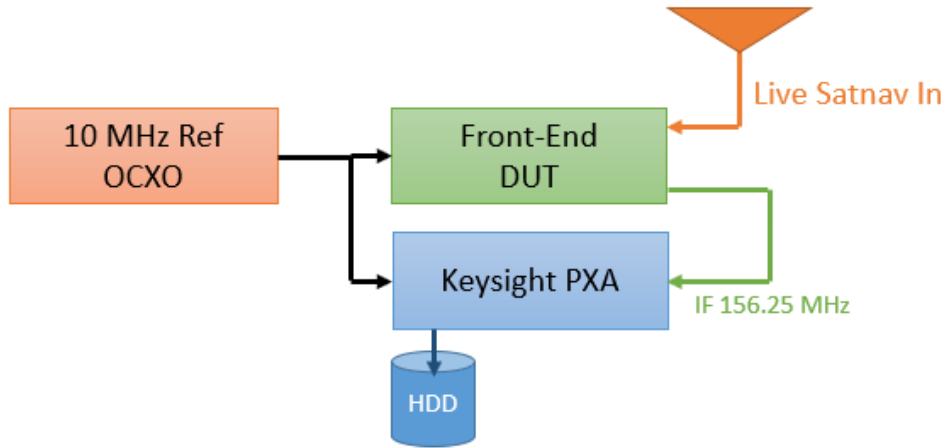


Figure 4.11.12: Live-sky Satnav Signal with LMX 2582 LO

Due to memory constraints of the PXA, only 19 seconds worth of data could be recorded at 62.5 MHz. Figure 4.11.13 displays the calculated PSD from averaging.

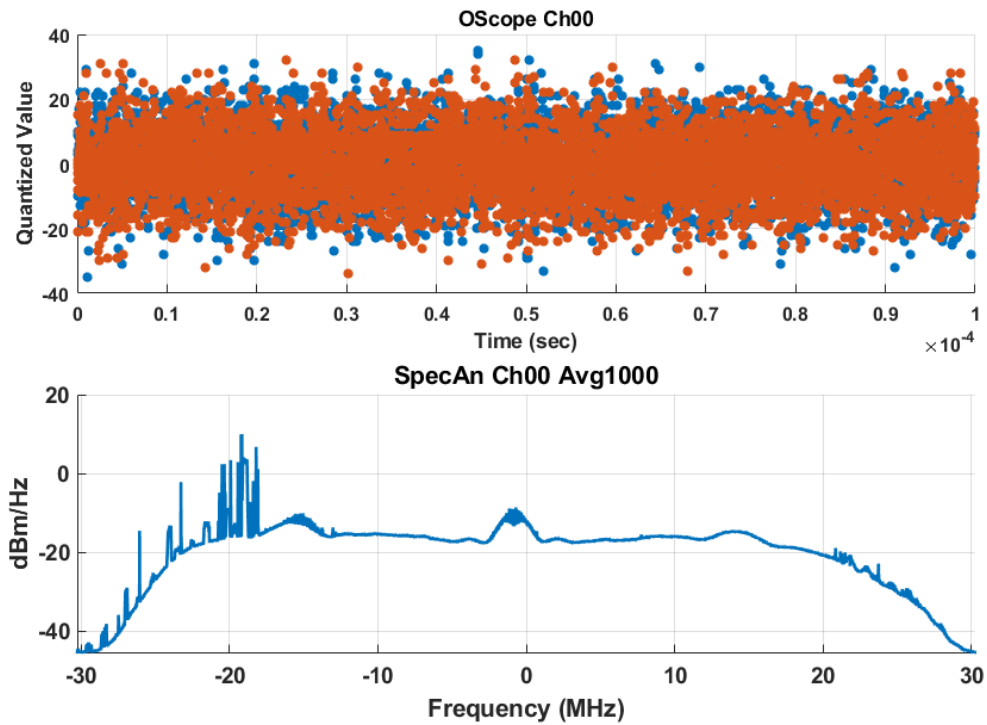


Figure 4.11.13: L1-Band Live-sky Capture 62.5 MHz of Bandwidth PSD

Several satnav signals are clearly present in the PSD, as well as some space-to-earth communication signals. A C/A acquisition algorithm was run on the saved data; the results of a high elevation, high CNR SV are shown in Figure 4.11.14. PRN 08 from SV 10 was acquired; SV 10 is a Block IIF satellite.

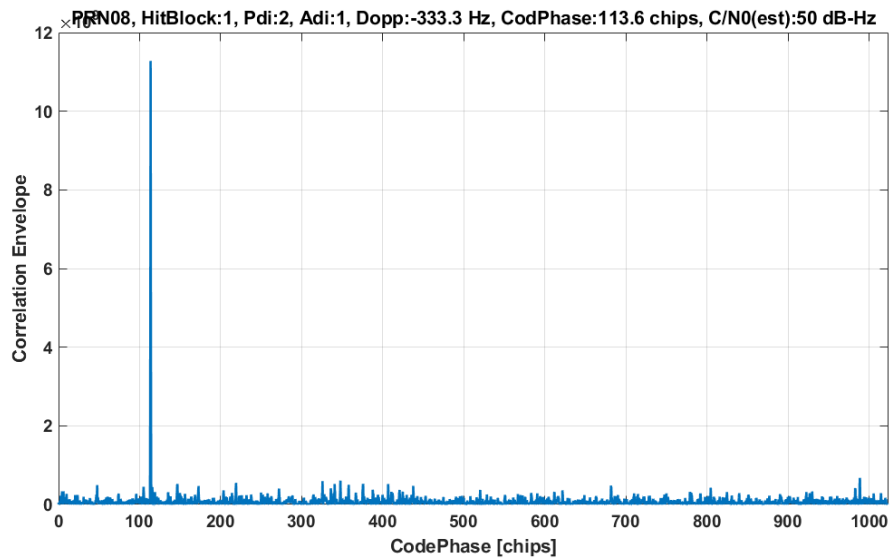


Figure 4.11.14: PRN 08 C/A Acquisition of Live-sky Signals

A 2nd order PLL with a wide bandwidth loop filter is used to lock onto the acquired signal parameters. The tracking loop then transitions to 6 Hz 2nd order PLL, with a 20 ms integration time. A high elevation, and high CNR satellite was chosen to be tracked. Figure 4.11.15 displays the carrier tracking loop filter output. The 2nd order PLL tracking loop can lock on and track the SV's signal.

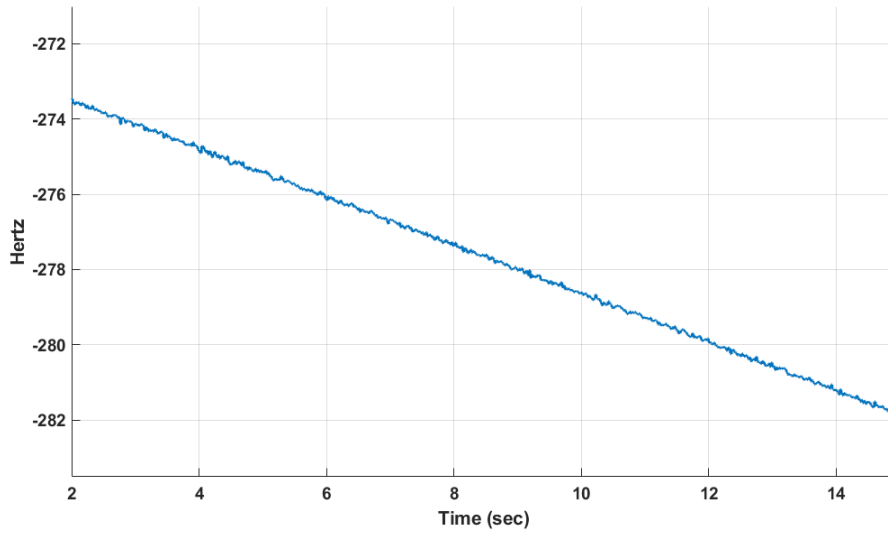


Figure 4.11.15: Live-Sky PRN 08 C/A Carrier Tracking Loop Output

When the signal is being tracked, an estimated CNR of over 50 dB was calculated. The CNR profile after the tracking loops have converged is displayed in Figure 4.11.16.

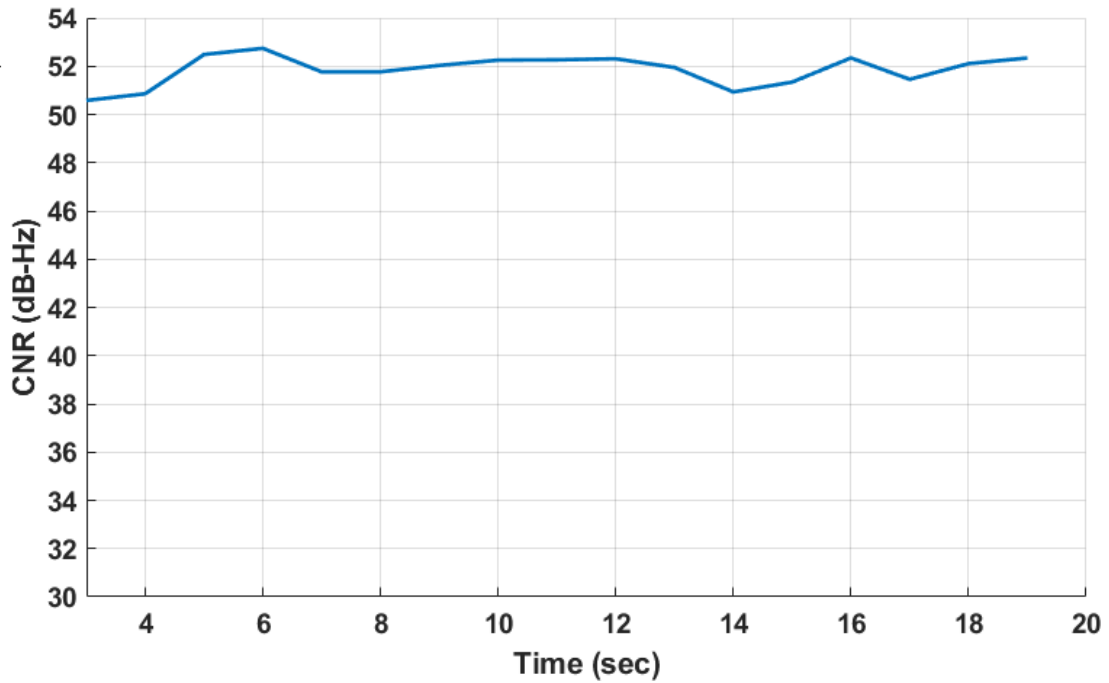


Figure 4.11.16: Live-Sky CNR of Tracked PRN 08

The carrier lock indicator is a metric that indicates the quality of the carrier tracking loop.

The lock detector indicator is displayed in Figure 4.11.17.

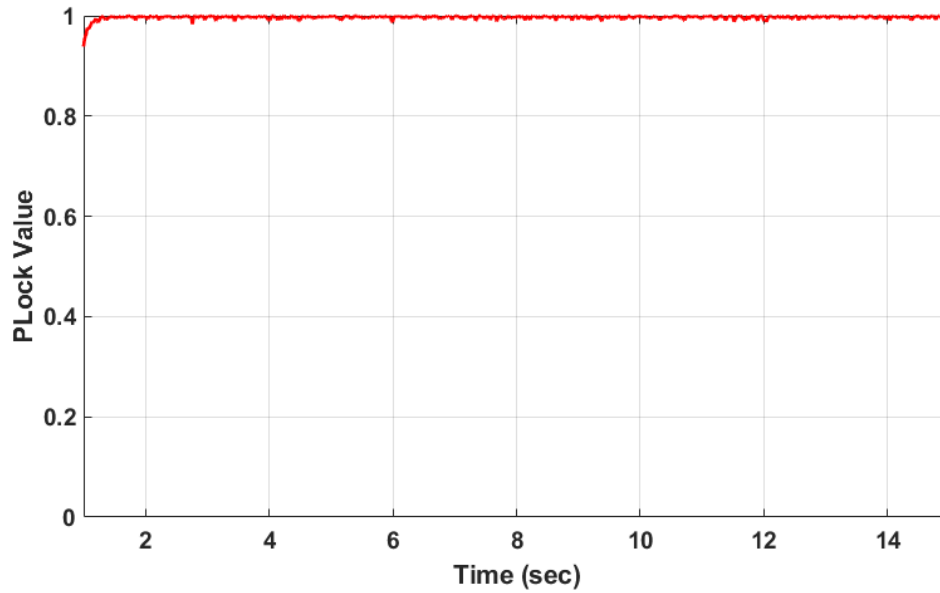


Figure 4.11.17: Live-Sky Carrier Tracking Lock Indicator for PRN 08

Figure 4.11.17 shows that once the receiver tracking loops have pulled in the satnav signal, the receiver maintains lock close to unity.

V. Conclusions and Recommendations

5.1 Conclusions of Research

A wideband instrumentation satnav front-end was designed for the purpose of high-fidelity signal and spectrum monitoring. The initial testing shows that this receiver meets the requirements. Several major achievements were met in this study:

- A validated frequency plan that is compatible with today's state of the art multi-channel ADCs.
- A Wide 50 MHz+ usable bandwidth supports M-Code and other wideband signal monitoring.
- Higher performance RF component selections and evaluations.
- RMS Power detector to accurately sense power before the mixer.
- High dynamic range to support use in high interference environments.
- Designed to support up to 100 dB J/S.
- Support for smart software-based gain control for preserving front-end linearity in the presence of high interference.
- High isolation RF PCB design using grounded coplanar waveguide.
- Temperature sensors at RF and IF stages to monitor and apply temperature compensation for temperature-induced group delay variations.
- Multiple configuration support. Multi-element, and multi-band coherent LO distribution.
- Design for high sensitivity, low phase noise, and low group delay.

- 3U Open VPX form factor to support modular assembly of various high-fidelity satnav SDR configurations for research as well as long-term deployment.
- Discrete LC IF filter design, characterization, and testing.
- Testing and validating the target ADC through the evaluation board.
- Satnav simulator and live-sky signal acquisition and tracking.
- Individual testing and characterization of group delay and linearity of the RF rooms using the VNA.
- Initial PCB and assembly of the front-end worked without any major modifications.

More quantitative analysis of the front-end developed in this study is required.

Satnav professionals demand a vetted and calibrated front-end for trusted nominal measurements. It is expected that this front-end design will meet these demanding requirements after careful analysis, characterization and additional revision/implementation/testing cycles.

5.2 Significance of Research

The design of the front-end can provide a baseline for technology transfer to other research labs or field use. As signal quality and spectrum monitoring becomes more pervasive and desirable, the design methodology, lessons-learned and contributions made through this research effort will hopefully serve as a baseline. The receiver can provide nominal signal characteristics which can enable advanced satnav signal monitoring and precision location and timing.

5.3 Recommendations for Future Research

To truly call this an instrumentation-grade satnav front-end, more focus on the FSPLL is needed. Initial testing revealed some close-in spurs at 60 Hz and 120 Hz which may be detrimental to tracking performance. Using an external VCO that has a frequency output from 1-2 GHz can greatly improve phase noise due to the lower N feedback division ratio required. A dual-loop FSPLL and increasing the RO frequency can improve spurious emissions and further reduce the phase noise. The downside of course is space and power consumption.

Software development is needed to sense the input power from either the ADC or the RMS power detector and adjust the RF and IF stage digital attenuators. Attenuation needs to be applied, adjusted, and logged during signal collections to preserve linearity.

The group delay variations of the IF bandpass filter can be greatly improved. Currently a 9th order bandpass filter is implemented. By lowering the filter order, group delay variations over the pass band can be reduced. The frequency response can also use some improvement. However, by characterizing the group delay and magnitude response of the front-end with the VNA, pre-processing can be applied to the sampled signal in order to remove group delay variations.

For advanced timing receivers, pseudorange biases caused by temperature changes in the front-end may be a problem. This can add larger variances to the time at longer sample intervals. By building temperature profiles for the front-end, the biases can be removed at either the baseband signal processing stage or post pseudorange computation stage. The sensitive temperature sensors built into this front-end can be leveraged eventually to implement this functionality.






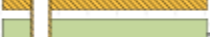
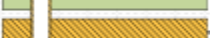






Direct conversion and direct sampling receivers have become extremely popular in satnav front-ends. An in-depth comparison between practical receivers based on these front-end architecture types can benefit the academic and industrial communities.

5.4 Summary

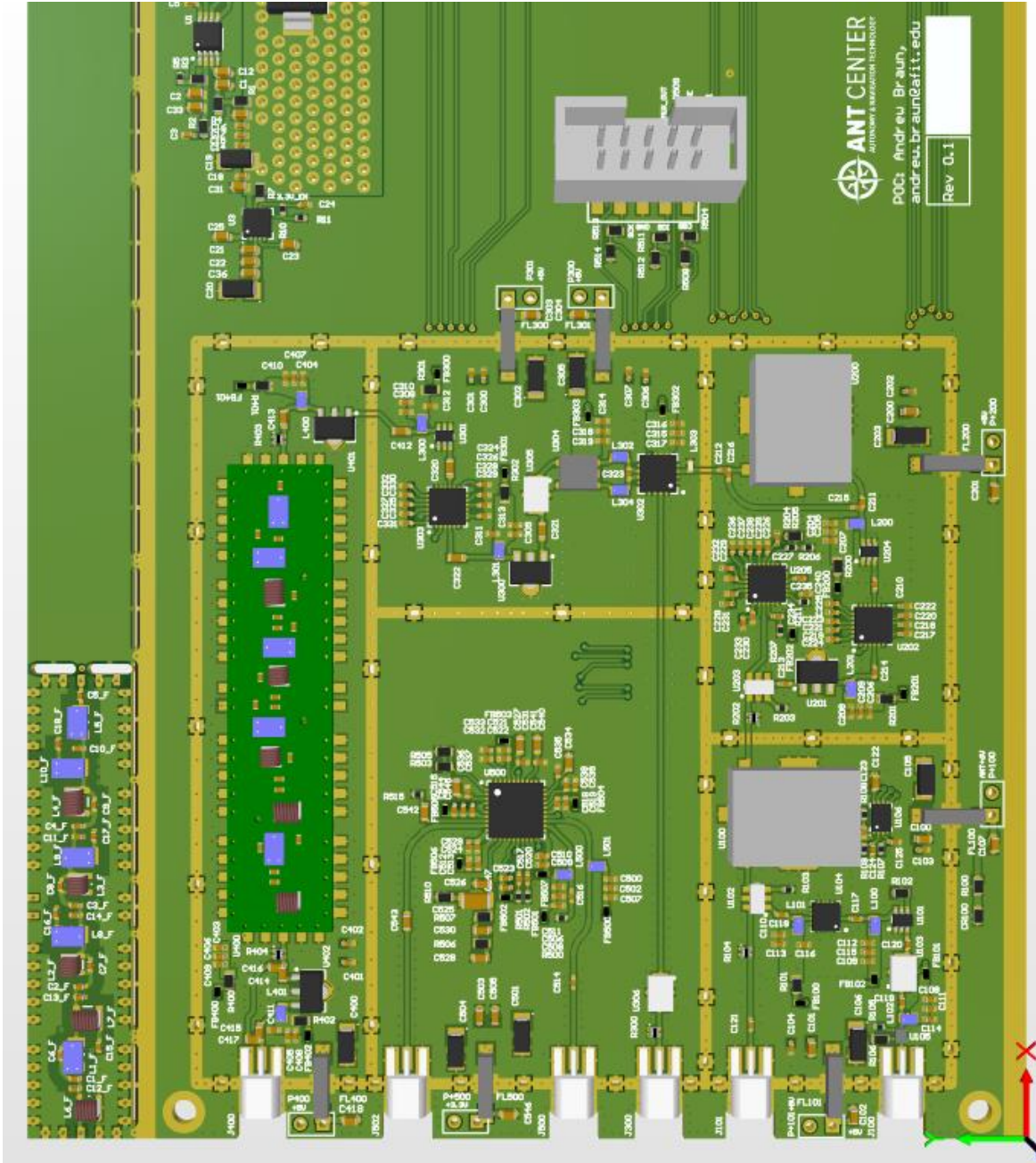
For this research, a satnav receiver front-end was modeled, designed, assembled, and tested over the span of 6 months. The front-end's group delay variations over the passband are lower than those of other receiver front-ends that have been previously implemented [47]. The phase noise and spurs from the FSPLL have been minimized through the design process. Digital gain control capabilities are included to keep the receiver operating in its linear region in high-interference environments.

Appendices

Appendix A: PCB Stack Up

Layer Stack Legend						
Material	Layer	Thickness	Dielectric Material	Type	Gerber	
	Top Paste			Paste Mask	GTP	
	Top Overlay			Legend	GTO	
	Surface Material	Top Solder	0.01mm	Solder Resist	Solder Mask	GTS
	Copper	Top Layer	0.04mm		Signal	GTL
	Core		0.20mm	RO4003C	Dielectric	
	Copper	Signal Layer 1	0.04mm		Signal	G1
	Prepreg		1.02mm	PrePreg	Dielectric	
	Copper	Signal Layer 2	0.04mm		Signal	G2
	Core		0.20mm	FR4	Dielectric	
	Copper	Bottom Layer	0.04mm		Signal	GBL
	Surface Material	Bottom Solder	0.01mm	Solder Resist	Solder Mask	GBS
	Bottom Overlay			Legend	GBO	
	Bottom Paste			Paste Mask	GBP	
Total thickness: 1.59mm						

Appendix B: 3D Render



Bibliography

- [1] S. Gunawardena, J. Raquet, and F. Van Graas, “A satellite with personality: Chip transition-edge based signal tracking for ultra-precise GNSS monitoring applications,” *GPS World*, vol. 26, no. 8, pp. 38–43, 2015.
- [2] S. Thombre, N. N. Tchamov, S. Lohan, M. Valkama, and J. Nurmi, “Effects of radio front-end PLL phase noise on GNSS baseband correlation,” *Navig. J. Inst. Navig.*, vol. 61, no. 1, pp. 13–21, 2014.
- [3] S. Gunawardena and F. Van Graas, “GPS-SPS Inter-PRN Pseudorange Biases compared for Transversal SAW and LC Filters using Live Sky Data and ChipShape Software Receiver Processing,” in *Proceedings of the 2015 International Technical Meeting*, 2015, pp. 393–403.
- [4] J. M. Guerrero and S. Gunawardena, “Characterization of Timing and Pseudorange Biases Due to GNSS Front-End Filters by Type, Temperature, and Doppler Frequency,” in *Proceedings of the 2017 International Technical Meeting of The Institute of Navigation*, 2018, pp. 418–444.
- [5] J. W. Betz, *Engineering Satellite-Based Navigation and Timing: Global Navigation Satellite Systems, Signals, and Receivers*. Piscataway, NJ: IEEE Press, 2016.
- [6] T. J. Roupael, *Wireless Receiver Architectures and Design: Antennas, RF, Synthesizers, Mixed Signal, and Digital Signal Processing*. Waltham: Elsevier, 2014.
- [7] M. L. Psiaki and D. M. Akos, “A Comparison of ‘ Direct RF Sampling ’ and ‘ Down-Convert & Sampling ’ GNSS Receiver Architectures,” *16th Int. Satell. Div. Inst. Navig. Tech. Meet.*, pp. 1941–1952, 2003.

- [8] R. G. Brown and P. Y. C. Hwang, *Introduction to Random Signals and Applied Kalman Filtering*. Wiley, 1992.
- [9] J. Ó. Winkel, “Modeling and Simulating GNSS Signal Structures and Receivers,” *Signals*, pp. 1–247, 2000.
- [10] W. Yu, G. Lachapelle, and S. Skone, “PLL Performance for Signals in the Presence of Thermal Noise, Phase Noise, and Ionospheric Scintillation,” in *Proceedings of the 19th International Technical Meeting of the Satellite Division of The Institute of Navigation (ION GNSS 2006)*, 2006, no. September, pp. 1341–1357.
- [11] W. J. Riley, *Handbook of Frequency Stability Analysis*, vol. 31, no. 1. NIST, 1994.
- [12] D. Banerjee, *PLL Performance, Simulation, and Design, Fifth Edition*. 2017.
- [13] A. Demir, “Phase noise and timing jitter in oscillators with colored-noise sources,” *IEEE Trans. Circuits Syst. I Fundam. Theory Appl.*, vol. 49, no. 12, pp. 1782–1791, 2002.
- [14] P. Mathecken, T. Riihonen, N. N. Tchamov, S. Werner, M. Valkama, and R. Wichman, “Characterization of OFDM radio link under PLL-based oscillator phase noise and multipath fading channel,” *IEEE Trans. Commun.*, vol. 60, no. 6, pp. 1479–1485, 2012.
- [15] “Texas Instruments LMX2582 Wideband PLLatinum RF Synthesizer With Integrated VCO,” 2017. [Online]. Available: <http://www.ti.com/lit/ds/symlink/lmx2582.pdf>. [Accessed: 07-Nov-2018].
- [16] S. Gunawardena and F. Van Graas, “Analysis of GPS-SPS Inter-PRN Pseudorange Biases due to Receiver Front-End Components,” in *Proc. Of the 27th International Technical Meeting of ION GNSS-2014*, 2014.

- [17] E. D. Kaplan and C. J. Hegarty, *Understanding GPS/GNSS Principals and Applications, Third Edition*. Boston: Artech House, 2017.
- [18] M. Irsigler and B. Eissfeller, “PLL Tracking Performance in the Presence of Oscillator Phase Noise,” *GPS Solut.*, vol. 5, no. 4, pp. 45–57, 2002.
- [19] J. J. Spilker, *Digital Communications by Satellite*. Englewood Cliffs, NJ: Prentice Hall, 1977.
- [20] P. Enge and P. Misra, *Global Positioning System: Signals, Measurements, and Performance - Revised Second Edition (2011)*, no. 2. 2011.
- [21] J. J. Spilker, P. Axelrad, B. W. Parkinson, and P. Enge, “‘GPS Receivers’, Global Positioning System: Theory and Applications, Volume I,” *Progress in Astronautics and Aeronautics*, 1996, pp. 329–407.
- [22] “AD9681.” [Online]. Available: <https://www.analog.com/media/en/technical-documentation/data-sheets/ad9681.pdf>. [Accessed: 02-Feb-2019].
- [23] “Modelithics.” [Online]. Available: <https://www.modelithics.com/>. [Accessed: 02-Feb-2019].
- [24] “Genesys Vendor Parts Synthesis.” [Online]. Available: <https://www.keysight.com/main/editorial.jspx?cc=US&lc=eng&ckey=2965156&nid=-34275.0.00&id=2965156&cmpid=zzfindeesof-genesys-vps>. [Accessed: 02-Feb-2019].
- [25] “Wenzel BTULN 501-27503-35.” [Online]. Available: <http://www.wenzel.com/model/btuln/>. [Accessed: 07-Nov-2018].
- [26] C. W. Sayre, *Complete Wireless Design, Second Edition*. McGraw-Hill, 2008.
- [27] “HMC542BLP4E.” [Online]. Available:

- <https://www.analog.com/media/en/technical-documentation/data-sheets/hmc542b.pdf>. [Accessed: 02-Feb-2019].
- [28] “HMC1020LP4E.” [Online]. Available:
<https://www.analog.com/media/en/technical-documentation/data-sheets/hmc1020.pdf>. [Accessed: 02-Feb-2019].
- [29] “MAAL-010704.” [Online]. Available: <https://www.macom.com/products/product-detail/MAAL-010704>. [Accessed: 14-Jan-2019].
- [30] “TQP3M9005.” [Online]. Available:
<https://www.qorvo.com/products/p/TQP3M9005>. [Accessed: 02-Feb-2019].
- [31] “SnP (Touchstone) File Format.” [Online]. Available:
http://na.support.keysight.com/plts/help/WebHelp/FilePrint/SnP_File_Format.htm.
[Accessed: 02-Feb-2019].
- [32] “RO4003C Laminates.” [Online]. Available:
<http://www.rogerscorp.com/acs/products/54/ro4003c-laminates.aspx>. [Accessed: 15-Jan-2019].
- [33] “Advanced Circuits.” [Online]. Available: <https://www.4pcb.com/>. [Accessed: 15-Jan-2019].
- [34] “Planar 304/1 3.2 GHz Analyzer.” [Online]. Available:
<https://coppermountaintech.com/vna/planar-304-1-vector-network-analyzer/>.
[Accessed: 15-Jan-2019].
- [35] “BK Precision Model 9130,” 2016. [Online]. Available:
<http://www.bkprecision.com/products/discontinued/9130-triple-output-programmable-dc-power-supply.html>. [Accessed: 07-Nov-2018].

- [36] “Analog Devices Microwave Wideband Synthesizer with Integrated VCO ADF4355-2,” 2016. [Online]. Available: <https://www.analog.com/media/en/technical-documentation/data-sheets/ADF4355-2.pdf>. [Accessed: 07-Nov-2018].
- [37] “Maxim Integrated 23.5MHz to 6000MHz Fractional/ Integer-N Synthesizer/VCO MAX2871,” 2017. [Online]. Available: <https://datasheets.maximintegrated.com/en/ds/MAX2871.pdf>. [Accessed: 07-Nov-2018].
- [38] “Analog Devices HMC830LP6GE Fractional-N PLL with Integrated VCO 25 - 3000 MHz v03.0512.” [Online]. Available: <https://www.analog.com/media/en/technical-documentation/data-sheets/hmc830.pdf>. [Accessed: 07-Nov-2018].
- [39] “Keysight PXA N9030B Spectrum Analyzer.” [Online]. Available: <https://www.keysight.com/en/pdx-2642777-pn-N9030B/pxa-signal-analyzer-multi-touch-3-hz-to-50-ghz?cc=US&lc=eng>. [Accessed: 07-Nov-2018].
- [40] “ADP3339.” [Online]. Available: <https://www.analog.com/media/en/technical-documentation/data-sheets/adp3339.pdf>. [Accessed: 02-Feb-2019].
- [41] “ADM7150.” [Online]. Available: <https://www.analog.com/media/en/technical-documentation/data-sheets/adm7150.pdf>. [Accessed: 02-Feb-2019].
- [42] “WavePro 7 Zi-A Series.” [Online]. Available: http://cdn.teledynelecroy.com/files/pdf/wavepro_7_zi-a_datasheet.pdf. [Accessed: 02-Feb-2019].
- [43] “EVAL-AD9681.” [Online]. Available: <https://www.analog.com/en/design->

center/evaluation-hardware-and-software/evaluation-boards-kits/eval-ad9681.html#eb-overview. [Accessed: 15-Jan-2019].

- [44] “Visual Analog™.” [Online]. Available: <https://www.analog.com/en/design-center/interactive-design-tools/visualanalog.html>. [Accessed: 15-Jan-2019].
- [45] “N5182B MXG X-Series RF Vector Signal Generator, 9 kHz to 6 GHz.” [Online]. Available: <https://www.keysight.com/en/pdx-x201912-pn-N5182B/mxg-x-series-rf-vector-signal-generator-9-khz-to-6-ghz?cc=US&lc=eng>. [Accessed: 15-Jan-2019].
- [46] “R&S®SMBV100A Vector Signal Generator.” [Online]. Available: https://www.rohde-schwarz.com/us/product/smbv100a-productstartpage_63493-10220.html. [Accessed: 15-Jan-2019].
- [47] S. Gunawardena, Z. Zhu, and F. Van Graas, “Triple Frequency RF Front-End for GNSS Instrumentation Receiver Applications,” in *Proceedings of the 21st International Technical Meeting of the Satellite Division of The Institute of Navigation (ION GNSS 2008)*, 2008, pp. 2984–2999.
- [48] “Polarx5.” [Online]. Available: <https://www.septentrio.com/products/gnss-receivers/reference-receivers/polarx-5>. [Accessed: 16-Jan-2019].

REPORT DOCUMENTATION PAGE

*Form Approved
OMB No. 0704-0188*

The public reporting burden for this collection of information is estimated to average 1 hour per response, including the time for reviewing instructions, searching existing data sources, gathering and maintaining the data needed, and completing and reviewing the collection of information. Send comments regarding this burden estimate or any other aspect of this collection of information, including suggestions for reducing the burden, to Department of Defense, Washington Headquarters Services, Directorate for Information Operations and Reports (0704-0188), 1215 Jefferson Davis Highway, Suite 1204, Arlington, VA 22202-4302. Respondents should be aware that notwithstanding any other provision of law, no person shall be subject to any penalty for failing to comply with a collection of information if it does not display a currently valid OMB control number.

PLEASE DO NOT RETURN YOUR FORM TO THE ABOVE ADDRESS.

1. REPORT DATE (<i>DD-MM-YYYY</i>)	2. REPORT TYPE	3. DATES COVERED (<i>From - To</i>)
---	-----------------------	--

4. TITLE AND SUBTITLE	5a. CONTRACT NUMBER
	5b. GRANT NUMBER
	5c. PROGRAM ELEMENT NUMBER

6. AUTHOR(S)	5d. PROJECT NUMBER
	5e. TASK NUMBER
	5f. WORK UNIT NUMBER

7. PERFORMING ORGANIZATION NAME(S) AND ADDRESS(ES)	8. PERFORMING ORGANIZATION REPORT NUMBER
---	---

9. SPONSORING/MONITORING AGENCY NAME(S) AND ADDRESS(ES)	10. SPONSOR/MONITOR'S ACRONYM(S)
	11. SPONSOR/MONITOR'S REPORT NUMBER(S)

12. DISTRIBUTION/AVAILABILITY STATEMENT
--

13. SUPPLEMENTARY NOTES

14. ABSTRACT

15. SUBJECT TERMS

16. SECURITY CLASSIFICATION OF:			17. LIMITATION OF ABSTRACT	18. NUMBER OF PAGES	19a. NAME OF RESPONSIBLE PERSON
a. REPORT	b. ABSTRACT	c. THIS PAGE			19b. TELEPHONE NUMBER (<i>Include area code</i>)